

# **Tuning laminar structures of graphene oxide-based membranes for water treatment**

By

**Yibin Wei**

Department of Environmental Sciences

**Supervisor:**

Prof. Damian Gore



**MACQUARIE**  
University  
SYDNEY • AUSTRALIA

FACULTY OF SCIENCE AND ENGINEERING

This thesis is presented for the degree of Doctor of Philosophy

March 2019



# Statement of Originality

I certify that the work in this thesis entitled “Tuning laminar structure of graphene oxide-based membranes for water treatment” has not previously been submitted for a degree nor has it been submitted as part of requirements for a degree to any other university or institution other than Macquarie University.

I also certify that the thesis is an original piece of research and it was authored by myself. Any help and assistance that I have received in the course of my research work and in the preparation of the thesis itself has, where appropriate, been acknowledged.

In addition, I certify that all information sources and literature used in the course of this research is also indicated where appropriate in this record of my thesis.

---

Yibin Wei

15 March 2019

© Yibin Wei, 2019.

# Table of Contents

<b>Statement of Originality .....</b>	<b>i</b>
<b>Table of Contents .....</b>	<b>ii</b>
<b>Abstract.....</b>	<b>iv</b>
<b>Acknowledgement.....</b>	<b>vi</b>
<b>List of Publications .....</b>	<b>ix</b>
<b>List of Acronyms.....</b>	<b>x</b>
<b>Chapter 1: Introduction .....</b>	<b>1</b>
1.1 Membrane Separation Technology .....	1
1.2 Water-treatment Membrane Materials .....	4
1.3 Graphene-based Membranes .....	6
1.3.1 Graphene-based Nanomaterials .....	6
1.3.2 Graphene Oxide Membranes.....	7
1.4 My Journey and Thesis Outline .....	10
1.4.1 The Journey with Membranes .....	10
1.4.2 Thesis Outline .....	13
1.5 References .....	16
<b>Chapter 2 A Literature Review: Specially Wettable Membranes for Oil-Water Separation.....</b>	<b>22</b>
2.1 Overview .....	22
2.2 Motivations and contributions .....	23
2.3 Story behind the article .....	24
2.4 The article- .....	25
<b>Chapter 3 Self-Cleaning Graphitic Carbon Nitride Nanotube Intercalated Reduced Graphene Oxide Membrane for Water Purification.....</b>	<b>52</b>
3.1 Overview .....	52
3.2 Motivations and contributions .....	53



3.3 Story behind the article .....	54
3.4 The article- .....	56
<b>Chapter 4 Precise Tuning Chemistry and Tailoring Defects of Graphene Oxide Films by Low Energy Ion Beam Irradiation.....</b>	<b>72</b>
4.1 Overview .....	72
4.2 Motivations and contributions .....	73
4.3 Story behind the article .....	74
4.4 The article- .....	76
<b>Chapter 5 Ion Beam Engineered Graphene Oxide Membranes for Mono-/Di-valent Metal Ion Separation .....</b>	<b>109</b>
5.1 Overview .....	109
5.2 Motivations and contributions .....	110
5.3 Story behind the article .....	110
5.4 The article- .....	113
<b>Chapter 6 Discussion and Summary .....</b>	<b>148</b>
6.1 Discussion .....	148
6.2 Summary .....	153
6.3 References .....	155

# Abstract

Membrane separation technologies are gaining attention for sustainable water supply since they are energy efficient, environmentally benign and economical. However, development of state-of-the-art membrane materials with well-defined nanostructures and excellent selectivity, high permeate flux and antifouling properties, remains challenging. Due to their excellent physical and chemical properties, two-dimensional (2D) graphene oxide (GO) is promising for use as building blocks for membrane construction. This thesis describes innovative research which constructs and tunes laminar structures of GO-based membranes for water treatment.

In this thesis, membrane separation technologies and membrane materials were introduced. Bioinspired conception for fabrication of polymeric, ceramic, metallic and nanomaterial-based free-standing membranes was then reviewed. GO could be combined with traditional membrane materials, forming composite membranes for enhanced separation performance. GO nanosheets (NS) could also be assembled into laminar structures solely for molecular and ion sieving. Laminar structures are attractive for designing GO-based membranes with desirable properties, which was a focus of this thesis.

Precisely tuning the crumpled laminar structure of GO-based membranes is crucial. I attempted to reduce GO and intercalate nano-fillers into the laminar structure. I developed a novel 1D graphitic carbon nitride nanotube (*g*-C<sub>3</sub>N<sub>4</sub> NT) intercalated reduced GO (rGO) nanofiltration (NF) membrane with enhanced photo-induced self-cleaning performance. The *g*-C<sub>3</sub>N<sub>4</sub> NT photocatalyst enlarged the rGO interlayer spacing for improved water permeability and endowed the composite membrane with visible-light photocatalytic activity for efficient removal of organic dyes from water. My *g*-C<sub>3</sub>N<sub>4</sub> NT/rGO membrane exhibits superior water permeability (4.87 L·m<sup>-2</sup>·h<sup>-1</sup>·bar<sup>-1</sup>) and synergetic Rhodamine B (RhB) removal rate (> 98%) for long-term operation. The RhB removal mechanism on the as-prepared composite membranes under integrated photocatalytic filtration was also established.

Apart from reducing GO and increasing laminar interlayer space to optimize the laminar structure of GO, I explored the potential for preparation of “nanoporous GO membranes” by *in-situ* ion beam modification. Ultra-thin (150-200 nm) GO films were modified by low energy carbon ion beams with ion fluences of  $1 \times 10^{15}$  ions·cm<sup>-2</sup> -  $1 \times 10^{17}$  ions·cm<sup>-2</sup>. Low

energy carbon ion beam irradiation can simultaneously reduce and drill nanoscale pores on GO surfaces in a controllable manner, which could be used for engineering GO-based separation membranes.

Ion beam modification was then used to prepare real GO ion-sieving membranes. The thickness of the GO layer and the ion fluence applied control the ion beam irradiated GO structure and the consequent mono-/di-valent metal ion separation performance. All ion beam irradiated GO membranes exhibited enhanced  $K^+$  selectivity compared with the ion separation performance of the corresponding GO membranes without ion beam treatment. Pure GO membrane with 0.5 mg GO loading amount exhibited a  $K^+$  ion permeation rate up to  $1.4 \times 10^{-3} \text{ mol} \cdot \text{m}^{-2} \cdot \text{h}^{-1}$  and an infinite separation factor to di-valent ions, after ion beam irradiation with fluence of  $1 \times 10^{16} \text{ ions} \cdot \text{cm}^{-2}$ . Ion beam modification was also successfully applied to EDA-modified GO membranes for enhanced selectivity, demonstrating the potential for applicability to other chemically modified GO membranes. This work is a step towards the development of high-performance GO-based membranes for use in water desalination, gas separation and biomedical applications.

**Key words:** graphene oxide; membranes; water treatment; nanofiltration; ion sieving

# Acknowledgement

The successful completion of this thesis was made possible through the invaluable help from dozens of people who have helped, instructed and encouraged me immensely.

First and foremost, I would like to express my sincere gratitude to my principal supervisor, Prof. Damian Gore, for his unconditional support, instructive advice and helpful suggestions during my time at Macquarie University. I appreciate all his contributions of time, patience and general supervision to make my PhD experience here productive and fruitful. Actually, this PhD is tough since I am the first PhD working on membrane research at Macquarie University. Without his protection and support, I might have quit this PhD. Very often I have moments that my heart is warmed and greatly touched by him. I recorded some of his replies to me from our email communications.

Moment 1: When I asked him if I could collaborate with other researchers, he replied that “it is your PhD. I am an advisor, and I want you to be the master of your own destiny. You’re the boss! Please collaborate with whomever you like without feeling the need to ask me. Only ask me if you ~want~ my opinion.”

Moment 2: He encouraged me to be the corresponding author for my work. When I asked him how to deal with the corresponding authorships, he replied that “All of my ~100 papers have one communicating author. It has never been a problem. But do what you want... it’s your paper, and you are a graduate, and a researcher. You have earned that respect, and right to make that decision.”

Moment 3: He is a strict supervisor. After finishing my 2017 departmental HDR presentation, he wrote to me immediately. “Filtration is mis-spelled in a number of places, and that is unacceptable. The table alignment and the captions you mention below are not fixed. I don’t want reasons, I want them fixed. Other changes were good yes, but you want these things perfect. They have to be for examination.” However, he is also a patient and nice supervisor. When I told him that I felt nervous when giving a presentation and using the laser, he kindly replied me that “Sometimes, I grip the laser with two hands to make it steady. Going over time is practice. You have to practice, again and again... only then do you get it right. Slow down, deliver less, tell the story better. It’s experience – and giving seminars like this gives you experience.”

There are too many cases that I could not mention them all. Overall, he is a respectable researcher and a nice advisor that I have been given unique opportunities to fully achieve the research project of my interest. and my experimental skills and scientific thinking were practiced in great extent. Besides, I am thankful for his support on my career plan. Once hearing that I secured a position after graduation, he was happy for me and encouraged me to submit my thesis earlier when I meet all the requirements of a PhD. Thank you, Damian!

Specially, I thank my previous collaborative supervisor and future team leader at Nanjing Tech University, China, Prof. Hong Qi. You hosted me as an independent researcher in your group before starting this PhD, supported me for some research facilities and research grants throughout this PhD, and are offering me a competitive position after this PhD. As my first University, Nanjing Tech is not only a research institute or a platform for me, but also my forever home. Thank you for taking me home and it is my honour to join your team for doing excellent research together.

Besides my advisor and mentor, my appreciation likewise extends to the rest of my collaborators: Dr Zeljko Pastuovic, Dr Timothy Murphy, Dr Yijiao Jiang and Dr Shen Chao, for their insightful comments and significant contributions to my research projects. I thank Yijiao for giving me access to her fully equipped laboratory for achieving my material research and the collaborative efforts for my first research work. Also, I thank Zeljko for the collaborative project using the ion beam for graphene oxide membrane modification, which is the big one for this thesis.

I would also like to thank my colleagues at Macquarie University, Dr Qingyao He, Dr Xin Cheng, Dr Xiaoyang Liu, Dr Long Ji, Xiong Cheng, Lian Jiang, Dr Sicong Tian, Dr Shilun Feng, Shengshen Gu, Jing He, Yan Wang, Xin Xu, Dr. Ping Tang, Sheran Li, Haftom Weldekidan, Asuramuni Chathurika Sewwandi Perera, Eva Gyamfi, Armin Kavehei, Huan Xiao, Jiayi Ai, Danfeng Wang, Dr Libing Fu, Zizhen Ming, Yameng Zhang and Muye Li for their support and encouragement in the last two years. You have been a source of friendship and fun. In addition, I thank all my friends in Sydney whose names should not be mentioned, for without you, my overseas study could not be enjoyable.

Financial support from Australian Government for my International Research Training Program (iRTP) scholarship and Macquarie University High Degree Research (HDR) funding should be acknowledged for my PhD candidature. National Collaborative Research

Infrastructure Strategy (NCRIS) funding provided by the Australian Government is acknowledged as well for the collaborative project with Australian Nuclear Science and Technology Organization (ANSTO).

Last but not least, I would like to express my utmost gratitude to my family members. I have been extremely fortunate in my life to have them who have given me their unflagging love and unconditional support during the past 28 years. I could not ask for more from my parents as they have both been great parents who raised me with love and financially supported me in all my pursuits.

# List of Publications

This thesis is an amalgamation of four articles (one Review Article and three Full-length Research Articles) consisting of four Chapters (Chapter 2-5), of which I was the lead author. The authorship of each article is strictly determined according to the Macquarie University Code for the Responsible Conduct of Research with the agreement of all co-authors. The Code on authorship refers to the Vancouver Protocol, and the detailed author academic contributions of each co-author are declared in the beginning of the corresponding Chapters.

**Chapter 2:** Y. Wei, H. Qi, X. Gong and S. Zhao. Specially wettable membranes for oil-water separation. *Advanced Materials Interfaces*, (2018) **5**, 1800576.

**Chapter 3:** Y. Wei, Y. Zhu and Y. Jiang. Self-cleaning graphitic carbon nitride nanotube intercalated reduced graphene oxide membrane for water purification. *Chemical Engineering Journal*. (2019) **356**: 915-925.

**Chapter 4:** Y. Wei, Z. Pastuovic, T. Murphy and D. B. Gore. Precise tuning chemistry and tailoring defects of graphene oxide films by low energy ion beam irradiation. *Submitted for publication*.

**Chapter 5:** Y. Wei, Z. Pastuovic, C. Shen and D. B. Gore. Ion beam engineered graphene oxide membranes for mono-/dia-valent metal ions separation. *Submitted for publication*.

# List of Acronyms

o/w	oil-in-water
w/o	water-in-oil
MF	microfiltration
UF	ultrafiltration
NF	nanofiltration
RO	reverse osmosis
FO	forward osmosis
MD	membrane distillation
CA	contact angle; cellulose acetate
WCA	water contact angle
OCA	oil contact angle
SL	solid–liquid
SV	solid–vapour
LV	liquid–vapour
LTA	local texture angle
HL	hydrophilic
HB	hydrophobic
OL	oleophilic
OB	oleophobic



SHB-SOL	superhydrophobic–superoleophilic
SHL-UWSOB	superhydrophilic–underwater superoleophobic
SHL-SOL	superhydrophilic-superoleophilic
SHB-SOB	superhydrophobic-superoleophobic
SSM	stainless-steel mesh
PAM	polyacrylamide
PDDA	poly (diallyldimethylammonium chloride)
PFO	perfluorooctanoate
POSS	polyhedral oligomeric silsesquioxane
x-PEGDA	cross-linked polyethylene glycol diacrylate
PTFE	poly-tetrafluoroethylene
PVDF	poly (vinylidene fluoride)
NWF	non-woven fabric
ALD	atomic-layer-deposition
PVDF-HFP	poly (vinylidene fluoride-co-hexafluoropropylene)
PEO	poly (ethylene oxide)
SDS	sodium dodecyl sulfate
MDEA	methyl diethanolamine
EG	ethylene glycol
PFDAE	1H,1H,2H,2H-perfluorodecyl acrylate
ODP	octadecyl phosphonic acid

P2VP-b-PDMS	poly (2-vinylpyridine)-b-polydimethylsiloxane
PNIPAAm	poly (N-isopropylacrylamide)
LCST	lower critical solution temperature
ATRP	atom transfer radical polymerization
PMMA	poly (methyl methacrylate)
TEOOS	triethoxy (octyl) silane
PEGMA	poly (ethylene glycol) methyl ether methacrylate
MMA	methyl methacrylate
SiNWA	silicon nanowire array
LbL	layer-by-layer
CNT	carbon nanotube
SWCNT	single walled-CNT
MWCNT	multiple walled-CNT
CVD	chemical vapor deposition
PSf	polysulfone
PES	polyethersulfone
PLA	polylactide
P34HB	poly (3-hydroxybutyrate-co-4-hydroxybutyrate)
PEG	poly (ethylene glycol)
TEOS	tetraethoxysilane
PU	polyurethane

SNF	silica nanofibrous
NP	nanoparticle
GO	graphene oxide
PGS	palygorskite
rGO	reduced graphene oxide
<i>g</i> -C <sub>3</sub> N <sub>4</sub>	graphitic carbon nitride
NS	nanosheet
NT	nanotube
1D	one dimension (al)
2D	two dimension (al)
3D	three dimension (al)
RhB	Rhodamine B
APT	attapulgit
MOF	metal organic framework
HNT	halloysite nanotube
TMPyP	tetrakis (1-methyl-4-pyridinio) porphyrin
PDA	polydopamine
MB	methylene blue
Tris	tris(hydroxymethyl) aminomethane
FE-SEM	field emission-scanning electron microscopy
HRTEM	high-resolution transmission electron microscopy

EDS	Electron dispersive spectrometry
SAED	selected area electron diffraction
AFM	atomic force microscopy
ATR-FTIR	attenuated total reflection-Fourier transform infrared
XRD	X-ray diffractometry
XPS	X-ray photoelectron spectrometer
UV–vis	ultraviolet–visible
PL	photoluminescence
Ra	arithmetical roughness
RMS	root mean squared roughness
CN	Cellulose nitrate
DI	deionized
ANSTO	Australian Nuclear Science and Technology Organization
KCl	potassium chloride
NaCl	sodium chloride
CaCl <sub>2</sub>	calcium chloride
MgCl <sub>2</sub>	magnesium chloride
EDA	ethylenediamine

**In order of precedence**

# Chapter 1: Introduction

## 1.1 Membrane Separation Technology

A membrane can be defined as a “thin barrier or film that exhibits permselectivity” when subjected to a driving force [1, 2]. Fig. 1.1 illustrates a typical model showing membrane process, whereby the membrane is mounted in a vessel forming two compartments. The membrane could selectively allow one of the constituents in the upper compartment to pass through, while blocking other constituents.

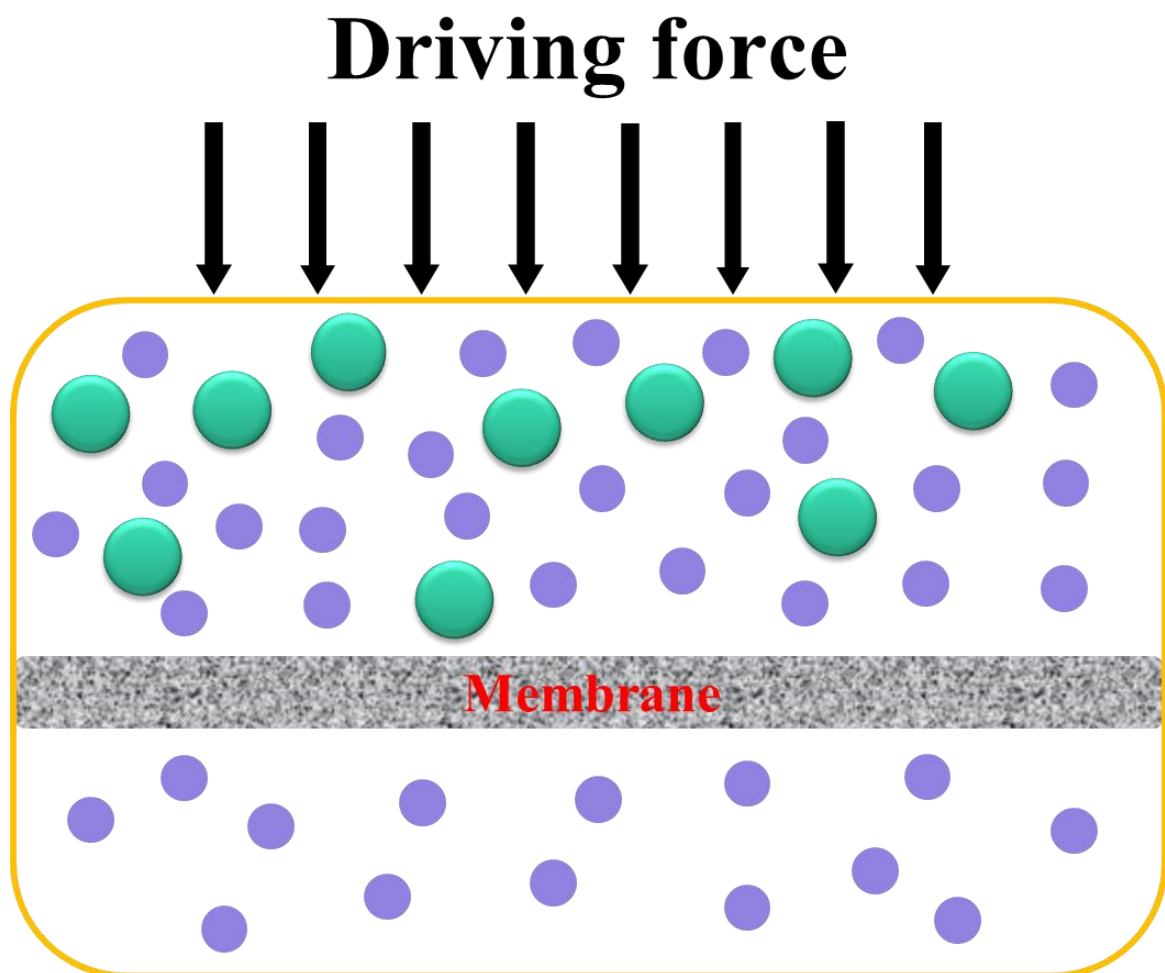


Figure 1.1. Schematic illustration of membrane separation process.

The feeding phases for membrane vessels are diverse; membranes could be used for gas-gas, gas-liquid, liquid-liquid, gas-solid and liquid-solid separation (e.g. liquids, gases, ions, molecules, and particles).

For membrane operation, a driving force is applied to the feeding fluid, forcing it to cross through the membrane. Pressure, concentration, temperature and electric potential gradient are commonly used driving forces in membrane operation [3-5]. With the development of smart membrane materials, diverse stimuli might be utilized as driving forces in the near future since many stimuli-responsive substances have been found and used to modify membrane materials [6].

Membrane materials are generally classified according to their nature (i.e. natural or synthetic membranes), structure and material type [7]. Common structures of synthetic membranes are presented in Fig. 1.2 Various types of membrane materials for water treatment will be discussed in next section in detail.

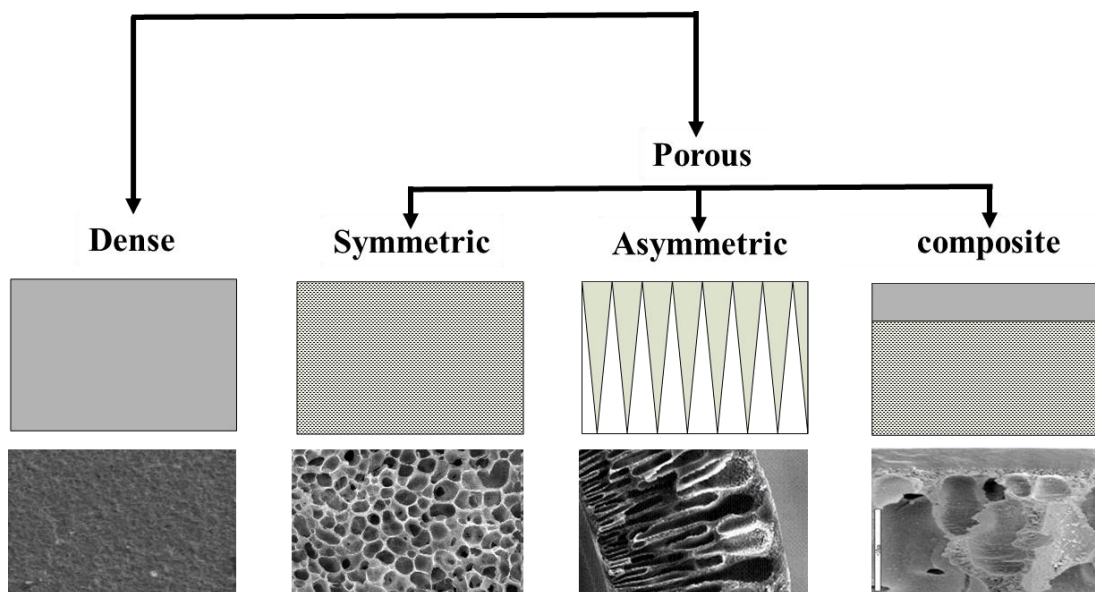


Figure 1.2. Common forms of synthetic membranes and corresponding scanning electron microscopy (SEM) images. (The SEM images are obtained from public lecture notes kindly shared by Prof. Enrico Drioli, Research Institute on Membrane Technology, ITM-CNR, Italy.)

Membrane separation technology involves many processes, which have recently become an accepted unit operation for a variety of industrial applications, providing technical solutions to the most urgent concerns of today (Fig. 1.3).

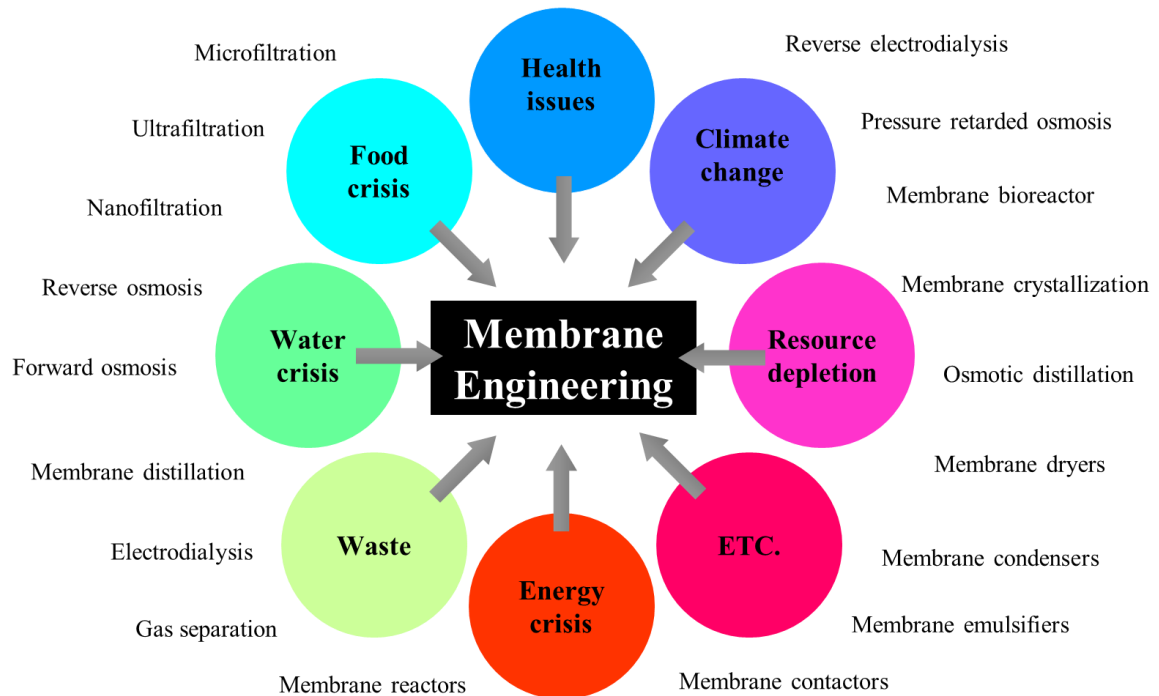


Figure 1.3. Membrane processes and membrane engineering solutions to challenges that human beings are facing today.

These membrane processes are generally classified by the driving force applied, feeding phases, and pore size of membrane materials used [8]. Among them, pressure-driven membrane processes including microfiltration (MF), ultrafiltration (UF), nanofiltration (NF), and reverse osmosis (RO) are predominant in water treatment industries [9-12]. Other membrane processes including but not limited to thermal-driven membrane distillation (MD) and osmotically driven forward osmosis have also been attempted for water treatment, especially desalination. However, the cost of thermal-driven membrane process is still not economical and the development of desired membrane materials for osmotically driven membrane processes is still challenging [13].

Currently, different textbooks or researchers define pressure-driven membranes differently because of the ongoing emergence of high performance membranes. Fig. 1.4 summarizes

commonly accepted definitions of pressure-driven membrane processes and the materials, which are mainly based on membrane pore size [14].

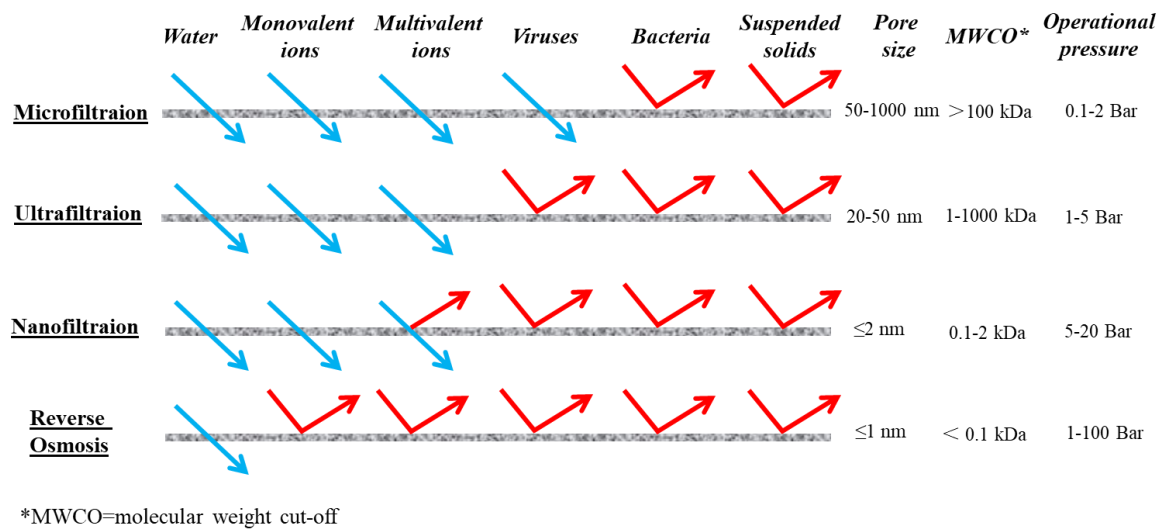


Figure 1.4. Characteristics of pressure-driven membrane processes

Additional desired characteristics are expected to be improved, which leaves room for membrane material scientists to challenge their knowledge and develop state-of-the-art membrane materials.

## 1.2 Water-treatment Membrane Materials

As discussed above, it is inappropriate to simply classify synthetic water treatment membranes according to their pore sizes. It is more reasonable to classify synthetic membranes on the basis of membrane material types: polymer-, ceramics-, metal-, and nanomaterial-based.

Owing to the remarkable advantages of low cost, prominent flexibility, excellent processability and ease of operation, polymeric membranes made of polysulfone (PSf), polyethersulfone (PES), polyvinylidene fluoride (PVDF), polytetrafluoroethylene (PTFE), etc., have been widely used in water treatment [15-19]. These membranes, however, may suffer from accumulation, adhesion, spreading, coalescence and migration of foulants as well as inevitable clogging during wastewater treatment, which results in flux decline and rejection deterioration [20].



In the family of membranes, porous ceramic membranes are important because of their high chemical, thermal and mechanical stability, which makes them suitable for use in harsh conditions such as corrosive and high temperature environments [21].



Figure 1.5. (a) Tubular ceramic membrane products with different shapes and channels and (b) oily waste water before and after treatment by ceramic membranes. (The photos were kindly provided by Prof. Hong Qi, Nanjing Hongyi Ceramic Membranes Co. Ltd., China, with all copyright reserved)

Ceramic membranes are made from alumina, titania, zirconia or silica oxides, silicon carbide, etc. [22]. Typical ceramic membranes are made in layers with different porous structure: a support (also known as the substrate) layer and a thin separation (also known as the top) layer. Sometimes an intermediate layer might also exist in a ceramic membrane. Ceramic supports usually consist of the above-mentioned metal oxide or inorganic powders, to which binders and plasticizers may be added. The resulting mixture is then pressed, extruded or slip cast prior to sintering. To obtain a ceramic membrane, the ceramic support surface has to be smoothed first. Then the flat ceramic support is usually coated with a casting material and then dried. Following coating and drying, a separation layer made of ceramic microcrystals is obtained by further calcination. This complicated manufacture process leads to relatively high cost of production and this consequently limits wide application of ceramic membranes in water treatment. As there is a growing tendency to apply ceramic membranes for industrial wastewater treatment, ceramic membranes with low production costs will be more attractive.

Dense metallic membranes (e.g. Palladium membrane) have for some time been considered for the separation of hot gases [23] while porous metallic membranes (e.g., stainless steel

mesh membranes, copper mesh membranes, or silver membranes) with pore diameters ranging from micro- to nanometer size have also been widely used for water treatment [24-26]. Gas separation membranes are out of scope of this thesis and the emerging mesh membranes are introduced in detail in Chapter 2.

With tremendous interest in nanotechnology, various types of metallic and several carbonaceous nanomaterials have drawn significant attention in recent years for water purification [27, 28]. In the field of water-treatment membranes, nanomaterials have been used not only to modify membrane surfaces but also to construct nanomaterial-based free-standing thin membranes. An ideal membrane is expected to have an active separation layer, which should be as thin as possible for pursuing low transport resistance and high flux. Therefore, taking advantage of their high surface area and special surface properties, 1D or 2D nanomaterials have made impressive progress in fabricating ultrathin filtration membranes with innovative structures which could exhibit low weight, high permeability and high rejection rate compared with traditional membrane materials.

## **1.3 Graphene-based Membranes**

### **1.3.1 Graphene-based Nanomaterials**

Since Geim and Novoselov received the Nobel Prize in Physics 2010 for their pivotal research on graphene [29, 30], graphene-based materials have attracted a growing interest in various environmental applications, such as metal ion removal [31], gaseous contaminants adsorption [32], desalination [33] and water treatment [34]. Graphene is composed of a single layer of carbon atoms arranged in a  $sp^2$ -bonded aromatic structure (Fig. 6) [35]. It possesses unique properties that make it attractive for environmental applications [36]. These properties mainly include special electronic mobility, excellent mechanical strength and high specific surface area. Although graphene is only one atom in thickness, it is the reported strongest material, with a Young's modulus of  $E = 1.0$  TPa and intrinsic strength of 130 GPa. Graphene also has the highest specific surface area, making it an ideal candidate for adsorption and surface reactions.

There are three types of graphene-based nanomaterials including graphene, graphene oxide (GO) and reduced GO (rGO). The general preparation route of graphene, GO and rGO from graphite is demonstrated in Fig. 6. Graphene can be produced by mechanical exfoliation from graphite, chemical vapour deposition (CVD) approach or by thermal decomposition of

SiC [32]. Graphene oxide (GO) is the oxidized derivative of graphene, which could be effectively produced through a solution-based approach by direct oxidation and exfoliation from graphite. GO could be regarded as a graphene scaffold with different oxygen-containing functional groups including epoxy, carboxyl, hydroxyl, and carbonyl [37]. The oxidation of GO provides abundant reaction sites for chemical modification. GO is the most popular graphene-based nanomaterial due to its low production cost. Moreover, GO could be easily reduced into rGO by chemical reduction, thermal reduction, or ultraviolet light irradiation-based reduction [38].

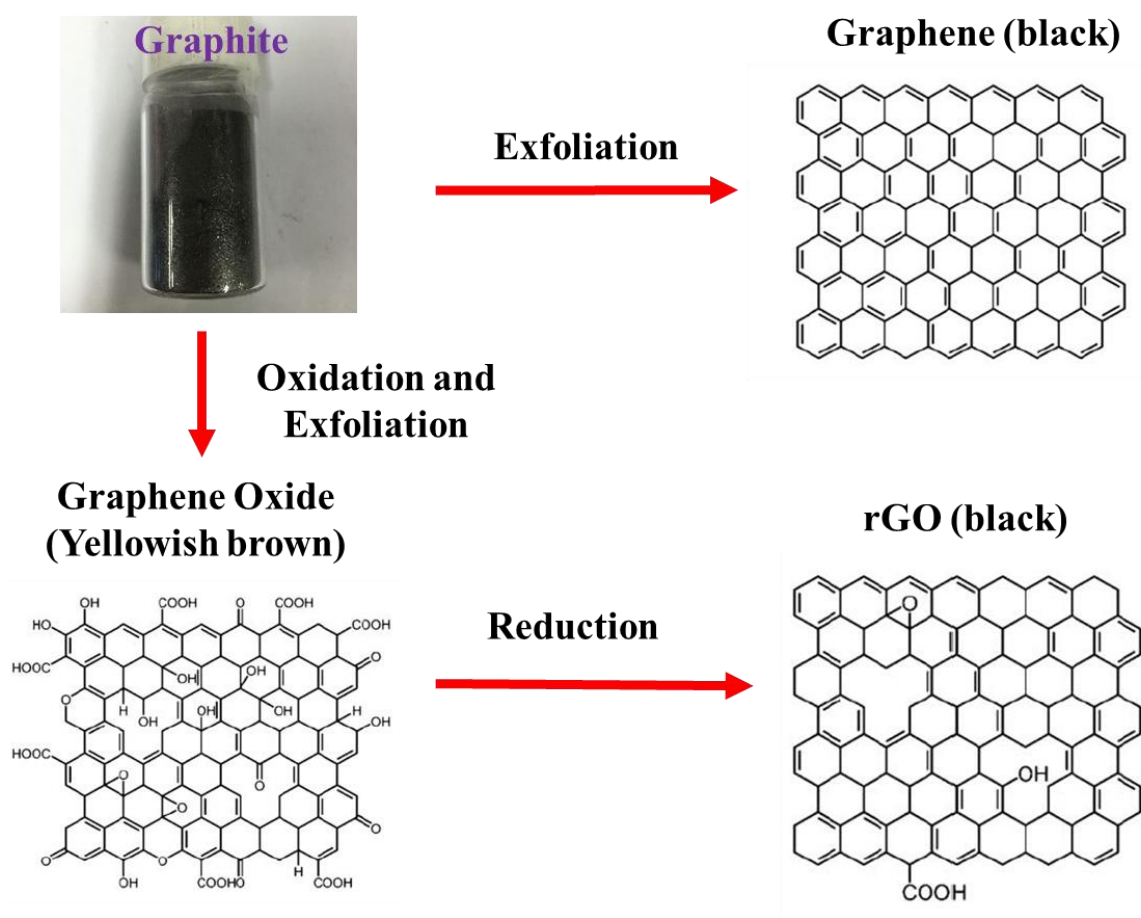


Figure 1.6. Schematic diagram for preparation of graphene, GO and rGO from graphite.

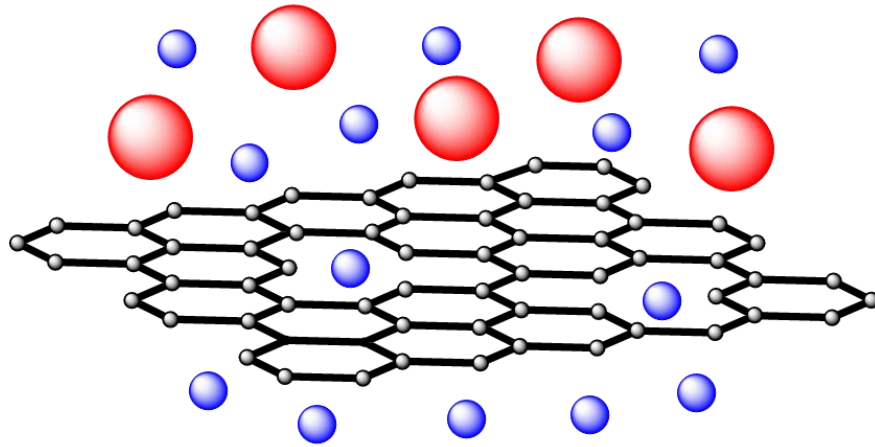
### 1.3.2 Graphene Oxide Membranes

In addition to direct doping graphene-based nanomaterials into a polymer matrix forming graphene-based composite membranes, there are two types of graphene-based membranes, including nanoporous graphene membranes and stacked GO membranes (Fig. 1.7) [39]. As

introduced above, production of graphene requires complicated procedures and high cost. Although many theoretical studies [40, 41] have predicted the extraordinary molecular separation performance of porous graphene and several experimental attempts [42, 43] drilling holes in graphene surface have confirmed the potential of porous graphene in selective passage of salt ions and gas molecules, facile and economical preparation of large-scale porous graphene membranes are still challenging.

Due to the low production cost of GO, there are exponentially growing studies on GO-based membranes [44]. Stacked GO that forms a laminar structure is able to be applied as a separation layer, which could either be assembled onto a support as a composite membrane or be a free-standing membrane [45]. The GO selective laminar-structured layer can be constructed via direct physical confinement such as filtration, drop casting, spin-coating, spray-coating, or dip-coating on substrates [46]. These methods are based on self-assembly, capillary force, centrifugal shear force and compressive force [47]. Among them, vacuum filtration based on compressive force is the most commonly used approach because the process is simple and the thickness of membranes is controllable by adjusting the loading amount, which shows great potential for industrial scaling up from lab research.

## **(a) Nanoporous Graphene Membrane**



## **(b) Laminar GO-based Membrane**

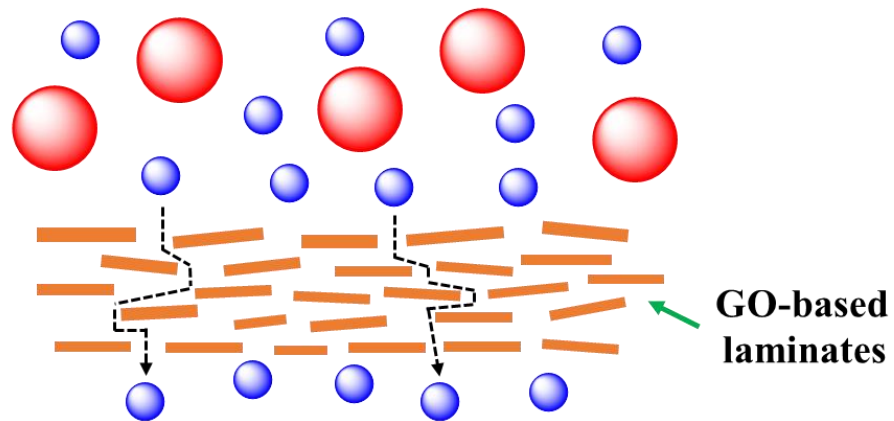


Figure 1.7. Schematic diagram of the two types of graphene-based membranes: (a) nanoporous graphene membranes consisting of a single layer of graphene with nanopores and (b) GO-based membranes with laminar structures.

In recent years, GO-based membranes with laminar structures have proved competitive for water treatment by various membrane operations. For example, Bhadra et al. [48] modified PTFE membrane surfaces with GO for desalination via direction contact membrane distillation (DCMD) and achieved a high water flux up to  $97 \text{ kg} \cdot \text{m}^{-2} \cdot \text{h}^{-1}$  at  $80^\circ \text{C}$ . The high performance of the GO membrane was attributed to selective sorption, the nanocapillary effect and reduced temperature polarization due to the presence of the polar functional groups of GO. GO has also been used to fabricate the selective layer of NF membranes for

heavy metal removal [31]. Huang et al. [49] developed a GO-based ceramic membrane for aqueous organic solution separation via pervaporation. Crumpled GO nanostructures can provide nanoscale channels for potentially fast water transport [50]. GO can also be incorporated with other materials such as TiO<sub>2</sub> [51], carbon nanotubes (CNT) [52] and hydrogels [53] via structure design or surface engineering to develop high performance membranes.

Despite great progress having been achieved, there remain many technical challenges to be overcome for fabricating reliable GO-based membranes in terms of stability, permeability and selectivity. GO-based membranes used for liquid separation generally need to be chemically modified due to their intrinsic water dispersion characteristic [54]. Cross-linking GO laminates and reducing GO are the simplest ways to enhance the water stability of GO-based membranes[55]. However, chemical modification often changes the GO laminar structure. The water transport channel of GO laminates are formed by face-to-face (van der Waals force) and edge-to-edge (electrostatic repulsive force) aligned GO and the reduction of GO can eliminate the oxygen-containing groups and narrow the water transport channels leading to a sharp decline in water permeability of the membrane [56]. To prepare robust and high performance GO-based membranes, most researchers apply the combined strategy of reduction of GO and intercalation with nano-spacers into the laminar structure [57].

## **1.4 My Journey and Thesis Outline**

### **1.4.1 The Journey with Membranes**

My passion for chemical-related engineering began as far back as high school, when my mother worked as an accountant for a coal washery, where the salary of engineers in her company is much higher than my mother's. Deeply influenced by this, I realized that chemical engineer working with energy resources is a high-paying job.

Before entering my first university, my chemistry grades were always ranked top in my class. Passing the rigid selection, the Chinese College Entrance Exam, I believed that engineering works are much more meaningful than pure chemistry, and the role of chemical engineers is to make chemical reactions scale up. Therefore, I chose chemical engineering as my subject for my first degree at Nanjing Technology University, China.

As a result of this sustained interest, I was quite studious towards becoming an excellent chemical engineer. After two years study in Nanjing Technology University, I was selected as an excellent undergraduate fully funded by the Chinese government to study in the University of Strathclyde (UK) for 1 year. Thanks to that study experience, I met an outstanding British Chinese scientist, Prof. Shanwen Tao who invented an interesting urine fuel cell device. He was happy to include me into his lab for a summer research project and that was the first time I came into contact with research. During nearly 4 months' lab work in his world class research centre, I was trained to carry out an independent research project fabricating electrolytes within a ceramic membrane, where I learned how to find answers that never appeared in the textbooks.

In February 2014, I went back to my home university to finish my graduate degree. I was designated to conduct research related to desulfurization of petrol using zeolite membranes. Benefitting from my previous research experience, my experiments went very well and the thesis was also evaluated as distinction by the academic panel at our school of Chemical Engineering.

Later on, even though I completed a fruitful M.Eng. degree in Gachon University, South Korea, for nanomaterials and biosensors research during 2014-2016, my strong will to pursue a Ph.D. education in the field of membrane research never stopped. Working in Macquarie University for a inorganic membrane material-based Ph.D. project was not an impulse decision, but a thorough consideration for my future development. For this MQ's Ph.D. project, I do not regret abandoning a Ph.D. scholarship offer for a polymer research project from University of New South Wales (UNSW, Australia).

In fact, my work in Macquarie University is about "Material-oriented Chemical Engineering for Environmental Applications" at the Department of Environmental Sciences. I am the first Ph.D. researcher at the university for membrane material research, therefore, I started with establishing experimental setups, where I met and overcame many problems during the process. Fortunately, my little toys, lab-scale filtration membrane performance evaluation setups, were designed, purchased and installed by myself after a half year. They could be used for gravity-driven, low or high pressure-driven dead-end and low pressure-driven cross-flow filtration processes (Fig. 1.8).



The research brings me a lot of fun. Fig. 1.8c shows the pink dye-containing water was put into the stirring cell as the feed and nearly clean water was collected in the permeate side driving by nitrogen gas. I was very excited at the moment that my first GO-based NF membrane was successfully prepared for dye-containing wastewater purification. The ground-breaking project “ion beam engineered GO membranes for water treatment” involved in the thesis attracted great interest by experts in the field of ion beam technologies, which cheers me up. Getting access to accelerators and collaborating with excellent scientists at the Australian Nuclear Science and Technology (ANSTO) also made this thesis happen.

#### **Gravity-driven filtration**



#### **Dead-end filtration**



#### **Cross-flow filtration**

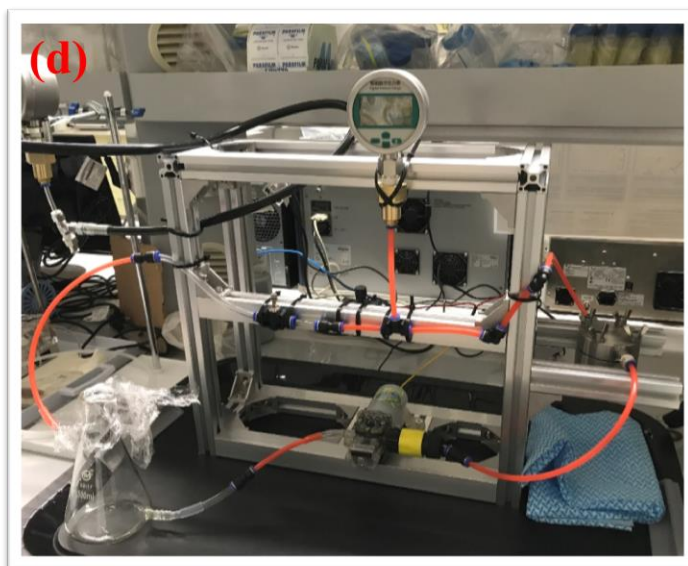


Figure 1.8. Digital photos of experimental setups. (Photos were taken by Yibin Wei.)



Making a membrane is like making a cake (Fig. 1.9). I got this idea when I started my first membrane research project. At that time, I saw researchers in white lab coats and safety glasses mix, heat, coat and calcine materials to form membranes. The process is very similar to a baker cooking a cake. In 2017, one of my co-authored papers was accepted for publication by Journal of Materials Chemistry A and the editor invited us to design a back cover to highlight the work. So, I designed this picture because I can find myself from it. Since my future career will continue to be with membranes, I will “bake” more high-performance membranes for solving practical and urgent energy and environmental issues. The future belongs to those who envision it, communicate it, and then make it happen. I am eager to be among them.



Figure 1.9. Schematic illustration of making a membrane in cartoon. (The artwork was designed by Dr. Huating Song, Yibin Wei and Prof. Hong Qi, with all copyright reserved.)

### 1.4.2 Thesis Outline

This thesis deals with the development of water-treatment membrane materials focusing on the cutting-edge theme of two dimensional (2D) GO-based membranes.

**Chapter 1** briefly introduces membrane separation technologies and membrane materials for water treatment. The background and a short review of the emerging graphene-based nanomaterials and graphene-based membranes are provided. Two types of transport channels in GO laminar membranes were proposed: (1) plane-to-plane interlayer galleries formed by face-to-face GO nanosheet interaction, and (2) in-plane structural defects and/or slit-like pores formed by edge-to-edge GO nanosheet interaction. The nanofiller intercalation is to expand GO plane-to-plane interlayer galleries, while the ion beam is to increase GO in-plane pores. By carefully regulating the interlayer spacing and creating in-plane pores, precise ion sieving can be achieved in GO laminar membranes.

**Chapter 2** is a comprehensive and up-to-date literature review conducted for all types of existing materials prepared under the concept of bioinspired special wettability. Although the focus is on oily wastewater treatment, a clear and intact membrane material research framework is established. With such deep understanding of membrane materials, especially GO-based membranes in mind, a series of GO-based membranes were prepared in the subsequent research.

As mentioned above, GO-based membranes show great potential to be the next generation of membrane materials for water treatment. Fabrication of high-performance GO-based membranes, in essence, is about efficient tuning of their laminar structures. Two strategies for tuning laminar structures of GO-based membranes were proposed. Fig 1.10a demonstrates the commonly adopted strategy that reduces GO laminates and intercalates nano-fillers into the laminar structure. Ion beam technology could reduce GO laminate *in-situ* and create subnanometer- and nanometer-sized pores on the reduced GO laminates simultaneously, which makes the laminar structure promising for salt ion separation (Fig. 1.10b). Due to the oxidation process, oxygen-containing functional groups on the GO surface create its intrinsic pores which could be reduced by ion beam or modified by chemical reagents to improve structural stability. In addition, nanopores on the rGO laminates could be precisely tailored by controlling the ion beam conditions. Therefore, tuning laminar structures of GO-based membranes by an ion beam offers new insights into designing high-performance water-treatment membrane materials.

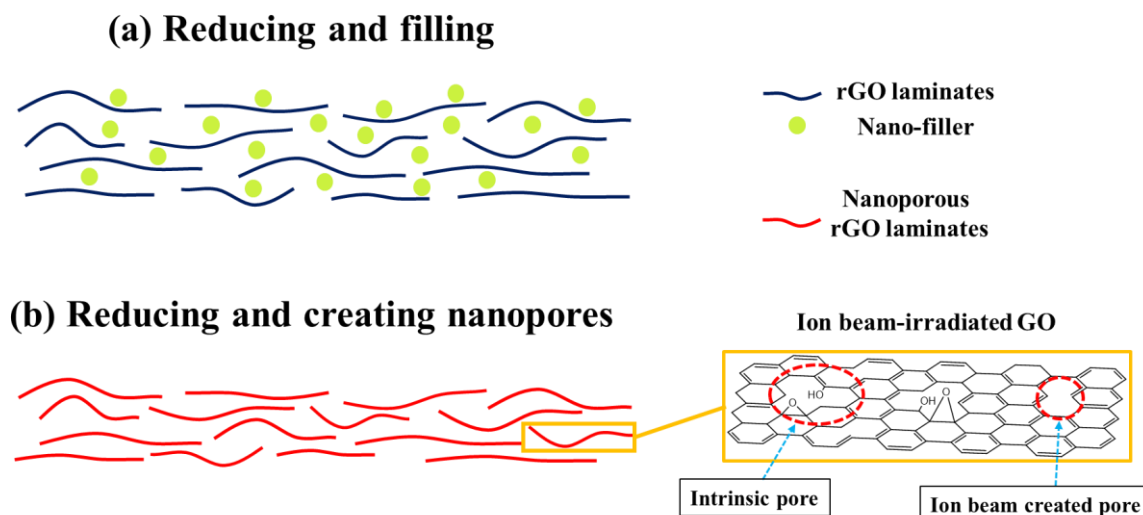


Figure 1.10. Schematic of two strategies for tuning laminar structure of GO-based membranes: (a) reducing and filling and (b) ion beam-induced reduction and pore engineering for GO laminates.

In **Chapter 3**, a photocatalytic self-cleaning rGO NF membrane for enhanced water treatment has been successfully prepared via the reducing and filling strategy. One dimensional (1D)  $g\text{-C}_3\text{N}_4$  NT and 2D  $g\text{-C}_3\text{N}_4$  NS were prepared as photocatalytic nano-fillers.  $g\text{-C}_3\text{N}_4$  NT/rGO and  $g\text{-C}_3\text{N}_4$  NS/rGO composites were then fabricated by intercalating  $g\text{-C}_3\text{N}_4$  NT and  $g\text{-C}_3\text{N}_4$  NS into a rGO laminar structure, respectively. The structure and corresponding properties of the prepared nanocomposites were well characterized by various methods. The influence of different dimensional intercalation on the rGO laminar structure and on the resultant membrane performance regarding water transport and Rhodamine B (RhB) removal were compared. Finally, the self-cleaning mechanism of the as-prepared composite membranes was described.

**Chapter 4** and **Chapter 5** focus on the novel strategy of fabricating porous GO membranes by ion beam-induced simultaneous *in-situ* reduction and defect engineering of GO. To the author's best knowledge, there are no GO-based separation membranes prepared by ion beam technology so far which brings the possibilities as well as difficulties to the research. In **Chapter 4**, ultra-thin GO films with thickness of 150-200 nm were prepared and then modified by a low energy carbon ion beam with ion fluences ranging from  $1 \times 10^{15}$  ions·cm<sup>-2</sup> to  $1 \times 10^{17}$  ions·cm<sup>-2</sup>. With the basic understanding of ion beam irradiated GO, in **Chapter 5**, I compared the effects of two key parameters - GO membrane thickness and ion fluence -

on GO membrane structure and consequent mono-/di-valent metal ion separation performance.

Finally, the discussion of my research and overall conclusions for this thesis including the outlook of GO-based membranes are presented in **Chapter 6**.

## 1.5 References

- [1] H.K. Lonsdale, Editorial, *J. Membr. Sci.* 34 (1987) 125-126.
- [2] H.K. Lonsdale, Editorial, *J. Membr. Sci.* 43 (1989) 1-3.
- [3] E. Drioli, L. Giorno, E. Fontananova, *Comprehensive Membrane Science and Engineering*, 2nd ed., Elsevier 2017.
- [4] H. Strathmann, *Introduction to Membrane Science and Technology* Wiley, 2011.
- [5] E. Drioli, L. Giorno, *Membrane Operations: Innovative Separations and Transformations*, Wiley, 2009.
- [6] Y. Wei, H. Qi, X. Gong, S. Zhao, Specially Wettable Membranes for Oil-Water Separation, *Adv. Mater. Interface.* 5 (2018), 1800576.
- [7] A. Lee, J.W. Elam, S.B. Darling, Membrane materials for water purification: design, development, and application, *Environ. Sci.: Water Res. Technol.* 2 (2016) 17-42.
- [8] R.W. Baker, *Membrane Technology and Applications*, 2nd Edition, Wiley, 2004.
- [9] L. Malaeb, G.M. Ayoub, Reverse osmosis technology for water treatment: State of the art review, *Desalination* 267 (2011) 1-8.
- [10] D.J. Miller, D.R. Dreyer, C.W. Bielawski, D.R. Paul, B.D. Freeman, Surface Modification of Water Purification Membranes, *Angew. Chem. Int. Ed.* 56 (2017) 4662-4711.
- [11] J. Yin, B.L. Deng, Polymer-matrix nanocomposite membranes for water treatment, *J. Membr. Sci.* 479 (2015) 256-275.

- [12] B. Van Der Bruggen, C. Vandecasteele, T. Van Gestel, W. Doyen, R. Leysen, A review of pressure-driven membrane processes in wastewater treatment and drinking water production, *Environ. Prog.* 22 (2003) 46-56.
- [13] M.M. Pendergast, E.M.V. Hoek, A review of water treatment membrane nanotechnologies, *Energ. Environ. Sci.* 4 (2011) 1946-1971.
- [14] A.G. Fane, R. Wang, M.X. Hu, Synthetic membranes for water purification: status and future, *Angew. Chem. Int. Ed.* 54 (2015) 3368-3386.
- [15] K. Venkatesh, G. Arthanareeswaran, A.C. Bose, PVDF mixed matrix nano-filtration membranes integrated with 1D-PANI/TiO<sub>2</sub>NFs for oil–water emulsion separation, *RSC Adv.* 6 (2016) 18899-18908.
- [16] R. Jamshidi Gohari, E. Halakoo, W.J. Lau, M.A. Kassim, T. Matsuura, A.F. Ismail, Novel polyethersulfone (PES)/hydrous manganese dioxide (HMO) mixed matrix membranes with improved anti-fouling properties for oily wastewater treatment process, *RSC Adv.* 4 (2014) 17587-17596.
- [17] R. Jamshidi Gohari, F. Korminouri, W.J. Lau, A.F. Ismail, T. Matsuura, M.N.K. Chowdhury, E. Halakoo, M.S. Jamshidi Gohari, A novel super-hydrophilic PSf/HAO nanocomposite ultrafiltration membrane for efficient separation of oil/water emulsion, *Sep. Purif. Technol.* 150 (2015) 13-20.
- [18] Y.-F. Zhao, L.-P. Zhu, Z. Yi, B.-K. Zhu, Y.-Y. Xu, Improving the hydrophilicity and fouling-resistance of polysulfone ultrafiltration membranes via surface zwitterionization mediated by polysulfone-based triblock copolymer additive, *J. Membr. Sci.* 440 (2013) 40-47.
- [19] B. Lee, Y. Baek, M. Lee, D.H. Jeong, H.H. Lee, J. Yoon, Y.H. Kim, A carbon nanotube wall membrane for water treatment, *Nat. Commun.* 6 (2015) 7109.
- [20] R. Zhang, Y. Liu, M. He, Y. Su, X. Zhao, M. Elimelech, Z. Jiang, Antifouling membranes for sustainable water purification: strategies and mechanisms, *Chem. Soc. Rev.* 45 (2016) 5888-5924.

- [21] H. Guo, S. Zhao, X. Wu, H. Qi, Fabrication and characterization of TiO<sub>2</sub>/ZrO<sub>2</sub> ceramic membranes for nanofiltration, *Micropor. Mesopor. Mater.* 260 (2018) 125-131.
- [22] L. Zhu, M. Chen, Y. Dong, C.Y. Tang, A. Huang, L. Li, A low-cost mullite-titania composite ceramic hollow fiber microfiltration membrane for highly efficient separation of oil-in-water emulsion, *Water Res.* 90 (2016) 277-285.
- [23] S. Adhikari, S. Fernando, Hydrogen membrane separation techniques, *Ind. Eng. Chem. Res.* 45 (2006) 875-881.
- [24] Y. Cao, X. Zhang, L. Tao, K. Li, Z. Xue, L. Feng, Y. Wei, Mussel-inspired chemistry and Michael addition reaction for efficient oil/water separation, *ACS Appl. Mater. Interfaces.* 5 (2013) 4438-4442.
- [25] F. Zhang, W.B. Zhang, Z. Shi, D. Wang, J. Jin, L. Jiang, Nanowire-haired inorganic membranes with superhydrophilicity and underwater ultralow adhesive superoleophobicity for high-efficiency oil/water separation, *Adv. Mater.* 25 (2013) 4192-4198.
- [26] N. Liu, X. Lin, W. Zhang, Y. Cao, Y. Chen, L. Feng, Y. Wei, A pure inorganic ZnO-Co<sub>3</sub>O<sub>4</sub> overlapped membrane for efficient oil/water emulsions separation, *Sci. Rep.* 5 (2015) 9688.
- [27] K.C. Kemp, H. Seema, M. Saleh, N.H. Le, K. Mahesh, V. Chandra, K.S. Kim, Environmental applications using graphene composites: water remediation and gas adsorption, *Nanoscale.* 5 (2013) 3149-3171.
- [28] S.C. Smith, D.F. Rodrigues, Carbon-based nanomaterials for removal of chemical and biological contaminants from water: A review of mechanisms and applications, *Carbon.* 91 (2015) 122-143.
- [29] A.K. Geim, K.S. Novoselov, The rise of graphene, *Nat. Mater.* 6 (2007) 183-191.
- [30] A.K. Geim, Graphene: status and prospects, *Science.* 324 (2009) 1530-1534.
- [31] Y. Zhang, S. Zhang, T.S. Chung, Nanometric Graphene Oxide Framework Membranes with Enhanced Heavy Metal Removal via Nanofiltration, *Environ. Sci. Technol.* 49 (2015) 10235-10242.

- [32] F. Perreault, A. Fonseca de Faria, M. Elimelech, Environmental applications of graphene-based nanomaterials, *Chem. Soc. Rev.* 44 (2015) 5861-5896.
- [33] K.A. Mahmoud, B. Mansoor, A. Mansour, M. Khraisheh, Functional graphene nanosheets: The next generation membranes for water desalination, *Desalination*. 356 (2015) 208-225.
- [34] Y. Zhu, S. Murali, W. Cai, X. Li, J.W. Suk, J.R. Potts, R.S. Ruoff, Graphene and graphene oxide: synthesis, properties, and applications, *Adv. Mater.* 22 (2010) 3906-3924.
- [35] L. Huang, M. Zhang, C. Li, G. Shi, Graphene-Based Membranes for Molecular Separation, *J. Phys. Chem. Lett.* 6 (2015) 2806-2815.
- [36] C. Lee, X. Wei, J.W. Kysar, J. Hone, Measurement of the elastic properties and intrinsic strength of monolayer graphene, *Science*. 321 (2008) 385-388.
- [37] X. Huang, Z. Yin, S. Wu, X. Qi, Q. He, Q. Zhang, Q. Yan, F. Boey, H. Zhang, Graphene-based materials: synthesis, characterization, properties, and applications, *Small*. 7 (2011) 1876-1902.
- [38] O.C. Compton, S.T. Nguyen, Graphene oxide, highly reduced graphene oxide, and graphene: versatile building blocks for carbon-based materials, *Small*. 6 (2010) 711-723.
- [39] G. Liu, W. Jin, N. Xu, Graphene-based membranes, *Chem. Soc. Rev.* 44 (2015) 5016-5030.
- [40] J.S. Bunch, S.S. Verbridge, J.S. Alden, A.M. van der Zande, J.M. Parpia, H.G. Craighead, P.L. McEuen, Impermeable atomic membranes from graphene sheets, *Nano Lett.* 8 (2008) 2458-2462.
- [41] D. Cohen-Tanugi, L.C. Lin, J.C. Grossman, Multilayer Nanoporous Graphene Membranes for Water Desalination, *Nano Lett.* 16 (2016) 1027-1033.
- [42] S.C. O'Hern, M.S. Boutilier, J.C. Idrobo, Y. Song, J. Kong, T. Laoui, M. Atieh, R. Karnik, Selective ionic transport through tunable subnanometer pores in single-layer graphene membranes, *Nano Lett.* 14 (2014) 1234-1241.

- [43] S.P. Surwade, S.N. Smirnov, I.V. Vlassiounk, R.R. Unocic, G.M. Veith, S. Dai, S.M. Mahurin, Water desalination using nanoporous single-layer graphene, *Nat. Nanotechnol.* 10 (2015) 459-464.
- [44] I.V. Vlassiounk, Water treatment: A scalable graphene-based membrane, *Nat. Nanotechnol.* 12 (2017) 1022-1023.
- [45] Y. Zhang, T.-S. Chung, Graphene oxide membranes for nanofiltration, *Curr. Opin. Chem. Eng.* 16 (2017) 9-15.
- [46] G. Liu, W. Jin, N. Xu, Two-Dimensional-Material Membranes: A New Family of High-Performance Separation Membranes, *Angew. Chem. Int. Ed.* 55 (2016) 13384-13397.
- [47] J. Shen, G. Liu, K. Huang, Z. Chu, W. Jin, N. Xu, Subnanometer Two-Dimensional Graphene Oxide Channels for Ultrafast Gas Sieving, *ACS Nano.* 10 (2016) 3398-3409.
- [48] M. Bhadra, S. Roy, S. Mitra, Desalination across a graphene oxide membrane via direct contact membrane distillation, *Desalination* 378 (2016) 37-43.
- [49] K. Huang, G. Liu, Y. Lou, Z. Dong, J. Shen, W. Jin, A graphene oxide membrane with highly selective molecular separation of aqueous organic solution, *Angew. Chem. Int. Ed.* 53 (2014) 6929-6932.
- [50] Y. Jiang, W.N. Wang, D. Liu, Y. Nie, W. Li, J. Wu, F. Zhang, P. Biswas, J.D. Fortner, Engineered crumpled graphene oxide nanocomposite membrane assemblies for advanced water treatment processes, *Environ. Sci. Technol.* 49 (2015) 6846-6854.
- [51] Y. Gao, M. Hu, B.X. Mi, Membrane surface modification with TiO<sub>2</sub>-graphene oxide for enhanced photocatalytic performance, *J. Membr. Sci.* 455 (2014) 349-356.
- [52] Y. Han, Y. Jiang, C. Gao, High-flux graphene oxide nanofiltration membrane intercalated by carbon nanotubes, *ACS Appl. Mater. Interfaces* 7 (2015) 8147-8155.
- [53] L. Huang, C. Li, W. Yuan, G. Shi, Strong composite films with layered structures prepared by casting silk fibroin-graphene oxide hydrogels, *Nanoscale.* 5 (2013) 3780-3786.



- [54] Y. Wei, Y. Zhu, Y. Jiang, Photocatalytic self-cleaning carbon nitride nanotube intercalated reduced graphene oxide membranes for enhanced water purification, *Chem. Eng. J.* 356 (2019) 915-925.
- [55] N. Meng, W. Zhao, E. Shamsaei, G. Wang, X. Zeng, X. Lin, T. Xu, H. Wang, X. Zhang, A low-pressure GO nanofiltration membrane crosslinked via ethylenediamine, *J. Membr. Sci.* 548 (2018) 363-371.
- [56] K. Guan, D. Zhao, M. Zhang, J. Shen, G. Zhou, G. Liu, W. Jin, 3D nanoporous crystals enabled 2D channels in graphene membrane with enhanced water purification performance, *J. Membr. Sci.* 542 (2017) 41-51.
- [57] H.M. Hegab, L. Zou, Graphene oxide-assisted membranes: Fabrication and potential applications in desalination and water purification, *J. Membr. Sci.* 484 (2015) 95-106.

# Chapter 2 A Literature Review: Specially Wettable Membranes for Oil-Water Separation

This chapter consists of:

- Overview
- Motivations and contributions
- Story behind the article
- The article-

## Abstract

### 1. Introduction

### 2. Wetting Phenomenon

#### 2.1. Contact Angles

#### 2.2. Wetting States in Oil–Water Separation

#### 2.3. Wetting with Membranes

### 3. Special Wettability on Membrane Surfaces

#### 3.1. Superhydrophobic–Superoleophilic Membranes

#### 3.2. Superhydrophilic–Underwater Superoleophobic Membranes

#### 3.3. Superhydrophilic–Superoleophobic (In-Air) Membranes

#### 3.4. Superamphiphilic (In-Air) Membranes

#### 3.5. Superomniphobic Membranes

#### 3.6. Smart Wettability in Membranes

#### 3.7. Janus Membranes

### 4. Membranes for Oil–Water Separation

#### 4.1. Metal-Based Membranes

#### 4.2. Polymer-Based Membranes

#### 4.3. Ceramic-Based Membranes

#### 4.4. Nanomaterial-Based Free-Standing Membranes

### 5. Conclusions and Outlook

### References

## 2.1 Overview

The Review Article forming this chapter has been published in the journal *Advanced Materials Interfaces*. Oil-water separation has attracted attention because of the ever-increasing amounts of oily water produced from industrial processes and other daily human activities. Cost-effective separation of oil-water mixtures is urgently needed for water,

energy and environmental security. Membrane separation technology has been successfully used in water industries for a few decades, demonstrating its significant technical and economical merits. However, it is inevitable that traditional membrane materials suffer from severe fouling, which counteracts the superiority of applying membranes in oil-water separation applications. Thanks to the emerging bioinspired interface research, special wettability not only endows membrane surfaces with outstanding antifouling properties, but also breaks through the long-standing trade-off effect between membrane permeability and selectivity. In addition to fundamentals such as the difficulty in separating oil-water mixtures and wetting phenomena on membrane surfaces, special wettability in membrane surfaces and its applications in oil-water separation are comprehensively summarized. The work brings novel insights into membrane material science for improved oily water treatment and may appeal to many research communities in areas such as water treatment, environmental remediation, material science and membranes.

## **2.2 Motivations and contributions**

Membranes have in recent decades gradually become the dominant separation technology in many industries. However, extensive research efforts are still needed, particularly from materials perspectives to improve the performance of existing membranes and to develop novel membranes for new applications. By learning from nature, bioinspired special wettability is an emerging research topic. The last few years have witnessed increasing applications of bioinspired interfacial materials in the separation field. Therefore, experts from the two research fields - specially wettable interfacial materials and conventional membrane materials - gathered together on 23-28 January 2018 in Melbourne, Australia for the 1st International Conference on Bioinspired Materials and Membranes (IBMM2018) to exchange innovative ideas and experiences for development of advanced materials and membranes for energy-efficient separation. It was timely to review, summarize and outlook this important, newly combined research direction.

The work was led by Yibin Wei. Two external experts, Prof. Hong Qi at Nanjing Tech University (China) and Prof. Xiao Gong at Wuhan University of Technology (China) were invited for collaborative efforts. Dr. Shuaifei Zhao at the Department of Environmental Sciences, Macquarie University participated in the work. Y. Wei proposed, planned and wrote the review article. S. Zhao helped revise the manuscript. H. Qi and X. Gong

contributed their knowledge in membrane materials and special wettability, respectively, providing useful and constructive suggestions to the work.

## **2.3 Story behind the article**

Writing a quality review article is not an easy task. As a newcomer to the bioinspired material research field, I read hundreds of papers and eventually 250 references were cited in the review. All co-authors believed the article is of high quality when we completed it. After a peer-review process and minor revision, the article was published online on 27 September 2018 by *Advanced Materials Interfaces*.

**Pages 25-51 of this thesis have been removed as they contain published material under copyright. Removed contents published as:**

Wei, Y., Qi, H., Gong, X., Zhao, S., Adv. Mater. (2018) Specially wettable membranes for oil–water separation, *Advanced Materials Interfaces*, vol. 5, no. 23, 1800576. <https://doi.org/10.1002/admi.201800576>

# Chapter 3 Self-Cleaning Graphitic Carbon Nitride Nanotube Intercalated Reduced Graphene Oxide Membrane for Water Purification

This chapter consists of:

- Overview
- Motivations and contributions
- Story behind the article
- The article-

Abstract

1. Introduction

2. Materials and methods

2.1. Materials

2.2. Synthesis of  $g\text{-C}_3\text{N}_4$  NS and  $g\text{-C}_3\text{N}_4$  NT

2.3. Synthesis of  $g\text{-C}_3\text{N}_4/\text{rGO}$  composites

2.4. Assembly of  $g\text{-C}_3\text{N}_4/\text{rGO}$  composite membranes

2.5. Characterization

2.6. Membrane filtration test

2.7. Photocatalytic performance evaluation

3. Results and discussion

3.1. Characterization of  $g\text{-C}_3\text{N}_4/\text{rGO}$  composites

3.2. Characterization of  $g\text{-C}_3\text{N}_4/\text{rGO}$  composite membranes

3.3. Evaluation of  $g\text{-C}_3\text{N}_4/\text{rGO}$  composite membranes

3.4. Self-cleaning mechanism

4. Conclusions

Reference

Supplementary Information

## 3.1 Overview

The Research Article presented in this chapter has been published in the *Chemical Engineering Journal*. Membrane separation technology has been successfully used in water industries for several decades, demonstrating its significant technical and economical merits. However, it is inevitable that membranes suffer from fouling, which reduces the benefits of

using membranes. Crumpled laminar nanostructures with nanoscale water transport channels constructed by two-dimensional (2D) reduced graphene oxide nanosheets (rGO NS) have been considered a promising membrane separation layer for water purification. In this study, I first report a novel 1D graphitic carbon nitride nanotube ( $g\text{-C}_3\text{N}_4$  NT) intercalated rGO nanofiltration (NF) membrane with a visible light-induced self-cleaning property, which can be used for efficient removal of organic dyes in an integrated photocatalytic filtration process. A photo-induced self-cleaning mechanism is proposed to explain this behaviour. The article brings novel insights into designing and tuning laminar structures of photocatalytic graphene-based NF membranes for enhanced water purification.

### **3.2 Motivations and contributions**

Constructing NF membrane materials with photo-induced self-cleaning properties gives rise to an emerging organic contaminant polluted water purification technology. Recently, graphitic carbon nitride ( $g\text{-C}_3\text{N}_4$ ) has attracted tremendous interest as a metal-free and visible-light photocatalyst owing to its good light-harvesting capability, high chemical stability, simple preparation and low cost. I realized that the combination of  $g\text{-C}_3\text{N}_4$  and rGO would enhance visible light absorption, overcome grain boundary effects of  $g\text{-C}_3\text{N}_4$  and facilitate electron transfer and charge for enhanced photocatalytic performance. In addition, the intercalation of  $g\text{-C}_3\text{N}_4$  into the rGO laminar structure was also expected to improve water flux. Inspired by expectations, the photocatalytic-induced self-cleaning GO membrane was designed by incorporating  $g\text{-C}_3\text{N}_4$ .

The work was led by Yibin Wei. Dr Yuxiang Zhu and Dr Yijiao Jiang at the School of Engineering, Macquarie University (the former was the previous fellow Ph.D. student of the latter), were invited for collaborative efforts. Y. Wei had the idea to develop the  $g\text{-C}_3\text{N}_4$  intercalated rGO photocatalytic membranes for enhanced water purification performance and designed the experiments. X. Zhu contributed to the synthesis of pristine  $g\text{-C}_3\text{N}_4$  nanomaterials and the analysis of  $g\text{-C}_3\text{N}_4$  nanomaterials and  $g\text{-C}_3\text{N}_4$ /rGO composites in terms of their optical properties. Y. Wei performed all of the remaining experiments and drafted the article. Y. Jiang supervised the project and provided constructive suggestions on it throughout the project. In addition, Y. Jiang critically revised the article for both technical and English language polish. A special appreciation must go to Prof. Damian Gore, who helped revised the English of the article without requesting authorship or acknowledgement.

### 3.3 Story behind the article

Dr Yijiao Jiang leads a passionate and fruitful research group working on catalysis at the School of Engineering, Macquarie University. With the same research interest in solving environmental problems, our membrane research group has very good linkage with Yijiao's group. On hearing that Yuxiang was working on the cutting-edge  $g\text{-C}_3\text{N}_4$  photocatalysts, I got the idea to combine my GO membranes with their  $g\text{-C}_3\text{N}_4$  photocatalyst for a unique collaboration.

Then, I searched for the relevant articles in the literature to see if the idea was possible or done by other researchers. After a careful analysis of the relevant literature, I believed that idea could work. However, there are two papers published regarding  $g\text{-C}_3\text{N}_4$  NS modified GO membranes for MF applications. I realized that Yuxiang and I have more space to work together because Yuxiang was working on the 1D  $g\text{-C}_3\text{N}_4$  NT. The 1D  $g\text{-C}_3\text{N}_4$  NT showed better photocatalytic performance than that of the 2D  $g\text{-C}_3\text{N}_4$  NS. In addition, I believed that incorporation of the 1D nano-filler into the GO laminar structure could result in higher water permeability than that of the 2D nano-filler. Moreover, I aimed at developing a high-performance NF membrane.

Therefore, it was possible to fabricate a novel photocatalytic  $g\text{-C}_3\text{N}_4$  NT/GO membrane. Yijiao is a very nice and open collaborator who agreed with my idea and gave me full support. I learnt a lot of new knowledge and skills from Yuxiang and Yijiao through this work. This research was published by the *Chemical Engineering Journal*, and was available online on 15 September 2018.



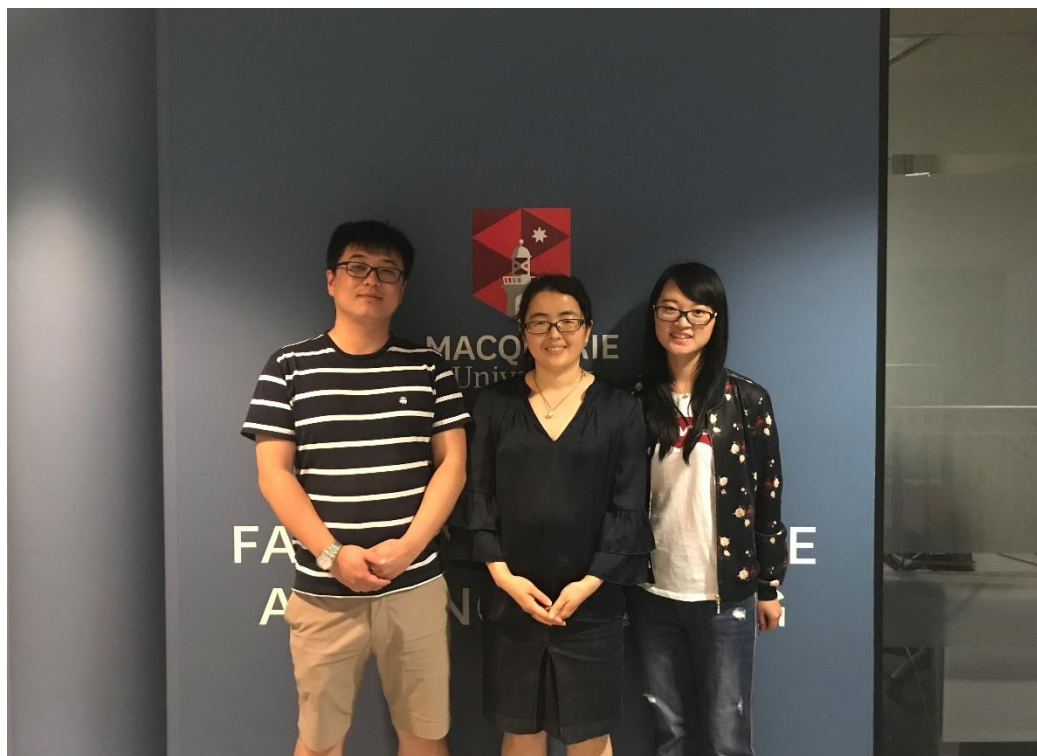


Figure 3.1. Photograph of co-authors of this article. (from left to right: Yibin, Yijiao and Yuxiang)

## 3.4 The article-

Chemical Engineering Journal 356 (2019) 915–925



Contents lists available at ScienceDirect

Chemical Engineering Journal

journal homepage: [www.elsevier.com/locate/cej](http://www.elsevier.com/locate/cej)



# Photocatalytic self-cleaning carbon nitride nanotube intercalated reduced graphene oxide membranes for enhanced water purification

Yibin Wei<sup>a,\*</sup>, Yuxiang Zhu<sup>b</sup>, Yijiao Jiang<sup>b,\*</sup>

<sup>a</sup> Department of Environmental Sciences, Macquarie University, Sydney, NSW 2109, Australia

<sup>b</sup> School of Engineering, Macquarie University, Sydney, NSW 2109, Australia

## HIGHLIGHTS

- Self-cleaning g-C<sub>3</sub>N<sub>4</sub>/rGO nanofiltration membranes were prepared.
- Organic dyes can be efficiently removed by an integrated process.
- 1D g-C<sub>3</sub>N<sub>4</sub> NT intercalated rGO membrane exhibits relatively competitive performance.
- Self-cleaning mechanism of the membranes is established.

## ARTICLE INFO

### Keywords:

Graphene oxide  
Carbon nitride nanotube  
Nanofiltration membrane  
Integrated photocatalytic filtration  
Water purification

## ABSTRACT

Crumpled laminar nanostructures with nanoscale water transport channels constructed by two-dimensional (2D) reduced graphene oxide nanosheets (rGO NS) have been considered as a promising membrane separation layer for water purification. However, efficient tuning of rGO laminar structures with enhanced membrane performance remains challenging. In this work, we report a novel 1D graphitic carbon nitride nanotube (g-C<sub>3</sub>N<sub>4</sub> NT) intercalated rGO nanofiltration (NF) membrane with enhanced photo-induced self-cleaning performance. The g-C<sub>3</sub>N<sub>4</sub> NT photocatalyst could not only enlarge the rGO interlayer spacing for improved water permeability, but also endow the composite membrane with visible-light photocatalytic activity for efficient removal of organic dyes from polluted water. Our g-C<sub>3</sub>N<sub>4</sub> NT/rGO membrane exhibits superior water permeability (4.87 L·m<sup>-2</sup>·h<sup>-1</sup>·bar<sup>-1</sup>) and synergetic Rhodamine B (RhB) removal rate (> 98%) for long-term operation, compared with pristine rGO membrane and 2D g-C<sub>3</sub>N<sub>4</sub> NS intercalated rGO membrane prepared by the same method. The RhB removal mechanism on the as-prepared composite membranes under integrated photocatalytic filtration process is presented. Our findings offer new insights into designing and tuning laminar structures of photocatalytic graphene-based NF membranes for enhanced water purification.

## 1. Introduction

Potable water production and wastewater reuse are essential for the sustainability of modern civilization [1]. Currently, mainstream water purification technologies remain high cost and energy intensive, thus efficient and cost-effective alternatives are required for society's ever-increasing water demand [2]. Membrane separation technologies are gaining attention for sustainable water supply since they are energy-efficient, environmentally benign and economical [3]. Nanofiltration (NF) is a pressure-driven membrane process exhibiting high retention rate for small molecules (with molecular weights ranging from 200 to 1000 Da) and relatively low energy consumption, resulting in increasing adoption for industrial wastewater purification [4–7].

However, development of state-of-the-art NF membranes with well-defined nanostructures and excellent selectivity, high permeate flux and antifouling properties, remains challenging. Two-dimensional (2D) graphene-based nanomaterials have drawn broad attention due to their excellent properties including distinct electron and thermal mobility, high mechanical strength, good capacity for microbial disinfection, ease of chemical or physical modification and high specific surface area [8–10]. Graphene and its most important derivative, graphene oxide (GO), exhibit similar properties, but GO holds many oxygen-containing functional groups distributed on the nanosheet (NS). To date, numerous GO-based membranes have been fabricated with laminar separation structures for gas separation, pervaporation, and pressure-driven filtration [11–14]. 2D GO NS has been regarded as a promising building

\* Corresponding authors.

E-mail addresses: [yibin.wei@hdr.mq.edu.au](mailto:yibin.wei@hdr.mq.edu.au) (Y. Wei), [yijiao.jiang@mq.edu.au](mailto:yijiao.jiang@mq.edu.au) (Y. Jiang).

<https://doi.org/10.1016/j.cej.2018.09.108>

Received 26 July 2018; Received in revised form 11 September 2018; Accepted 14 September 2018

Available online 15 September 2018

1385-8947/ © 2018 Elsevier B.V. All rights reserved.



block for the construction of new generation NF membranes with laminar nanostructures [6,15–17].

Although GO-based NF membranes have been successfully developed in recent years, there remains many technical challenges to be overcome for fabricating even high-performance membranes [18–21]. Pristine GO used for liquid separation generally needs to be chemically modified due to its intrinsic water dispersion characteristic [22]. Cross-linking GO laminates [23,24] and reduced GO (rGO) [25] are the simplest ways to enhance the water stability of GO-based membranes. However, chemical modification often changes the GO laminar structure. The water transport channel of GO laminates are formed by face-to-face (van der Waals' force) and edge-to-edge (electrostatic repulsive force) aligned GO NS and the reduction of GO can eliminate the oxygen-containing groups and narrow the water transport channels leading to a sharp decline in water permeability of the membrane [26]. To create water transport channel in GO-based laminar structure, Wang et al. used attapulgite (APT) nanorods as fillers for constructing NF membranes [27]. For the purpose of preparing robust and high performance NF membranes, most researchers applied both strategies, i.e. reduction of GO and intercalation with nano-spacers into the laminar structure. For examples, Zhang et al. intercalated metal organic framework (MOF), UiO-66-(COOH), into ultrathin rGO to prepare enhanced NF membranes for water purification [28]. Halloysite nanotubes (HNTs) and self-assembled 5, 10, 15, 20-tetrakis (1-methyl-4-pyridinio) porphyrin (TMPyP) molecules were attempted to be intercalated into rGO laminates for the purpose of tuning nanochannels [29,30]. Intercalating nano-spacers into rGO laminar structure has been proved to be an efficient strategy for enlarging water transport channels of rGO-based membranes, but very few intercalations can facilitate the rGO membrane with other desirable properties [31–35].

Recently, graphitic carbon nitride ( $g\text{-C}_3\text{N}_4$ ) has attracted tremendous interest as a metal-free and visible-light photocatalyst owing to its good light-harvesting capability, high chemical stability, simple preparation and low cost [36,37]. Unlike most metal-containing photocatalysts that need expensive metal precursors for synthesis,  $g\text{-C}_3\text{N}_4$  photocatalyst can be facilely prepared by thermally polycondensing cheap N-rich precursors, such as dicyanamide, cyanamide, melamine, and urea. The only disadvantage for  $g\text{-C}_3\text{N}_4$  is less visible light response and high electron-hole recombination [38]. Coincidentally,  $g\text{-C}_3\text{N}_4$  usually shows relatively low visible-light photocatalytic activity, but the introduction of rGO can efficiently promote an improvement [39]. Many studies have shown that graphene-based materials could conjugate well with nano-photocatalysts to enhance light absorption and charge separation of the heterostructure for improved photo-responsivity [40,41]. Graphene and  $g\text{-C}_3\text{N}_4$  possess similar carbon networks and  $sp^2$  conjugated  $\pi$  structures [42,43], which makes them the most compatible materials to form composites. The combination of  $g\text{-C}_3\text{N}_4$  and rGO would enhance visible light absorption, overcome grain boundary effects of  $g\text{-C}_3\text{N}_4$  and facilitate electron transfer and charge separation across the composite interface.

The concept of photocatalytic  $g\text{-C}_3\text{N}_4$ /rGO composite membranes was first proposed in 2014. Zhao et al. [44] attempted to intercalate 2D  $g\text{-C}_3\text{N}_4$  NS into the rGO laminar structure to enhance cellulose acetate microfiltration (MF) membranes. They found that the composite membrane showed enhanced efficiency for the removal of organic contaminants from surface water under visible-light irradiation. In 2017, Li et al. [45] developed a polydopamine (PDA) modified  $g\text{-C}_3\text{N}_4$  NS/rGO membrane which was used for efficiently separating oil-in-water emulsion and removing methylene blue (MB) dyes simultaneously when irradiated by visible light. To the best of our knowledge, these two studies are the only reports on photocatalytic  $g\text{-C}_3\text{N}_4$ /rGO composite membranes. They revealed that  $g\text{-C}_3\text{N}_4$ /rGO composite membranes have great potential in enhanced water purification, but there is still much scope for the improvement. For example, NF membranes can remove dye contaminants more efficiently, and intercalating different dimensions of  $g\text{-C}_3\text{N}_4$  photocatalyst can optimize the  $g\text{-C}_3\text{N}_4$ /

rGO composite structures and consequently improve membrane performance. Among various nanostructured  $g\text{-C}_3\text{N}_4$ , it was evident by one of our recent studies that 1D  $g\text{-C}_3\text{N}_4$  nanotube (NT) materials exhibited much better photocatalytic performance compared with its bulk and NS structures [46]. Many researchers believe that morphological control of  $g\text{-C}_3\text{N}_4$  is an effective method to tune the specific surface area, light-induced carrier migration distance and active centers for enhancing its photocatalytic performance [47]. Recent experimental and theoretical studies have also confirmed the superior photocatalytic activity of  $g\text{-C}_3\text{N}_4$  NT under visible light and a series of  $g\text{-C}_3\text{N}_4$  NT-based photocatalysts with enhanced hydrogen generation rate were reported [48–50].

In this work, 1D  $g\text{-C}_3\text{N}_4$  NT and 2D  $g\text{-C}_3\text{N}_4$  NS were prepared as photocatalytic nano-fillers.  $g\text{-C}_3\text{N}_4$  NT/rGO and  $g\text{-C}_3\text{N}_4$  NS/rGO composites were then fabricated by intercalating  $g\text{-C}_3\text{N}_4$  NT and  $g\text{-C}_3\text{N}_4$  NS into a rGO laminar structure, respectively. The structure and corresponding properties of the prepared nanocomposites were well understood by various characterization methods. The influence of different dimensional intercalation on the rGO laminar structure and on the resultant membrane performance regarding water transport and Rhodamine B (RhB) removal were compared. Finally, the self-cleaning mechanism of the as-prepared composite membranes was described.

## 2. Materials and methods

### 2.1. Materials

Graphene oxide (GO) water dispersion (4 mg/mL) was purchased from Graphenea Corporation. Melamine (99%), tris(hydroxymethyl) aminomethane (Tris, ACS reagent,  $\geq 99.8\%$ ), ethylenediamine ( $\geq 99.8\%$ ), hydrochloric acid (ACS reagent, 37%), anhydrous ethanol and dopamine hydrochloride ( $\geq 99\%$ ) were purchased from Sigma Aldrich. Rhodamine B (RhB) was obtained from Alfa Aesar. Commercial cellulose acetate (CA) membranes (diameter: 47 mm; pore size: 450 nm) were purchased from Sterlitech Corporation. All chemicals were used as received. Deionized (DI) water ( $18.2\text{ M}\Omega\text{-cm}^{-1}$  at  $25^\circ\text{C}$ ) used throughout this study was generated by a Milli-Q system.

### 2.2. Synthesis of $g\text{-C}_3\text{N}_4$ NS and $g\text{-C}_3\text{N}_4$ NT

5 g of melamine powder was calcined at  $550^\circ\text{C}$  for 2 h in static air to form bulk  $g\text{-C}_3\text{N}_4$ .  $g\text{-C}_3\text{N}_4$  nanosheets (NS) were then exfoliated from the bulk dissolved in ethanol by ultrasonic treatment for 1 h.  $g\text{-C}_3\text{N}_4$  nanotubes (NT) were synthesized by a modified water-induced morphological transformation process [46]. Briefly, the as-synthesized  $g\text{-C}_3\text{N}_4$  NS were then heated at  $350^\circ\text{C}$  for 10 min with a heating rate of  $10^\circ\text{C}/\text{min}$ . The hot powder was rapidly transferred into an ice-water bath.  $g\text{-C}_3\text{N}_4$  NT were finally obtained by filtration and drying at  $120^\circ\text{C}$  for 12 h under vacuum.

### 2.3. Synthesis of $g\text{-C}_3\text{N}_4$ /rGO composites

The details of synthesis and characterization of GO and rGO are present in the Supporting Information.  $g\text{-C}_3\text{N}_4$  NS/rGO and  $g\text{-C}_3\text{N}_4$  NT/rGO composites were synthesized through a facile physical adsorption process. 30 mg  $g\text{-C}_3\text{N}_4$  NS or  $g\text{-C}_3\text{N}_4$  NT were added into 1 mg/mL rGO solution (100 mL) under vigorous stirring for 24 h, respectively. After that, the mixtures were kept for 2 h and the well-dispersed  $g\text{-C}_3\text{N}_4$ /rGO composites were collected before use. The collected composites were dried under vacuum at  $60^\circ\text{C}$  for 12 h.

### 2.4. Assembly of $g\text{-C}_3\text{N}_4$ /rGO composite membranes

Disc-type CA membranes were used as substrates. Prior to membrane assembly process, the substrate was pre-treated with polydopamine (PDA) to enhance the adhesive force between the substrate

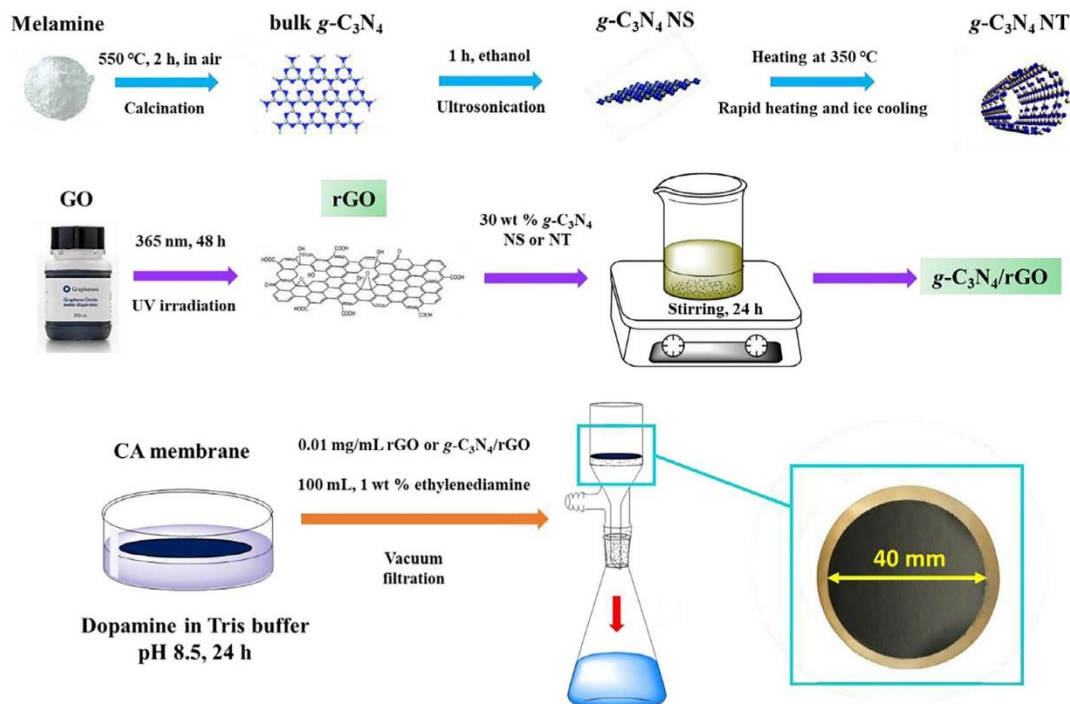


Fig. 1. Schematic illustration for the preparation process of composite materials and membranes.

and the rGO separation layer. Inspired by marine mussels, dopamine could self-polymerize and stick on all kinds of surfaces as a versatile molecular linker [51,52]. 0.16 g of dopamine hydrochloride was dissolved into 80 mL 0.01 M Tris buffer (pH 8.5) to obtain the coating solution. CA substrate was then immersed in the solution at room temperature for 24 h. Dopamine underwent self-polymerization and formed an adhesive polydopamine layer on the substrate during this time. The CA substrate was subsequently rinsed with plenty of DI water to remove unreacted PDA [53]. 0.01 mg/mL rGO,  $g\text{-C}_3\text{N}_4$  NS/rGO and  $g\text{-C}_3\text{N}_4$  NT/rGO water dispersions with 1 wt% ethylenediamine were used as membrane casting solutions. Ethylenediamine was used as cross-linker to enhance the stability of the rGO laminar structure. By using a vacuum-assisted filtration method, 100 mL of those as-prepared membrane casting materials were filtrated through the CA membranes at room temperature. All of the above-mentioned preparation procedure is summarized and presented in Fig. 1.

## 2.5. Characterization

A Phenom XL scanning electron microscope with electron dispersive spectrometry (SEM-EDS) was used to image surface and cross-section morphologies of the as-prepared membranes with filament conditions of mapping mode. High-resolution transmission electron microscopy (HRTEM, JEM-2100F, JEOL) with selected area electron diffraction (SAED) analysis was used to study the morphologies of the synthesized composites. Membrane surface roughness was measured using atomic force microscopy (AFM, NanoScope, Veeco Metrology) with the scan size of  $10 \times 10 \mu\text{m}$ . Fourier transform infrared (FTIR) spectra of membrane casting materials and membrane surfaces were measured by Thermo Nicolet 6700 (Thermo Fisher Scientific). Crystalline structure was analyzed by X-ray diffractometry (XRD, Aeris, PANalytical) using Cu K $\alpha$  radiation at 40 kV and 15 mA. Raman spectra were recorded on

LabRAM (HORIBA) using 785 nm wavelength incident laser light with 3 s exposure time, 10 s acquisition time and 10 accumulations. An X-ray photoelectron spectrometer (XPS) (Thermo Fisher, ESCALAB 250XI) was used for quantitative elemental analysis. The X-ray source is monochromated Al K $\alpha$  ( $h\nu = 1486.68 \text{ eV}$ ) operated at 150 W. Pass energy of 100 eV was applied to wide scans and 20 eV was used for high resolution scans. The scan number is 20 times and the spot size is  $500 \mu\text{m}$ . The binding energies were calibrated with reference to C1s at 284.8 eV for adventitious hydrocarbon contamination. The wettability of the membranes was analyzed by static water contact angle (WCA) measurements using the sessile drop method on a contact angle goniometer (DSA30, KRÜSS) equipped with a video camera recording system. The ultraviolet–visible (UV–vis) diffuse reflectance spectra were recorded on a Varian Cary 500 Scan UV–vis spectrophotometer. Photoluminescence (PL) measurements were carried out on a Fluorolog-Tau3 fluorescence spectrophotometer with an excitation wavelength of 330 nm at room temperature.

## 2.6. Membrane filtration test

The water permeability of the prepared membranes was determined by a dead-end filtration configuration. A 50 mL Amicon stirring cell was purchased from Millipore and nitrogen gas was used as the driving force. The effective area of the membrane surface is  $11.3 \text{ cm}^2$ . All experiments were conducted under steady state at  $25^\circ\text{C}$  with a constant transmembrane pressure of 4.5 bar. The permeate was continuously collected and monitored by a digital balance. The water permeability is calculated according to the Eq. (1):

$$J = \frac{V}{A \times p \times t} \quad (1)$$

where  $J$  is the water permeability ( $\text{L} \cdot \text{m}^{-2} \cdot \text{h}^{-1} \cdot \text{bar}^{-1}$ ),  $V$  is the collected



permeate volume (L),  $A$  is the membrane effective area ( $\text{m}^2$ ),  $p$  is the transmembrane pressure (bar), and  $t$  is the permeation time (h).

RhB, a dye with a molecular weight of 479 Da, was chosen as a representative organic contaminant. The concentration of RhB solution in the feed and the permeate side was analyzed by ultraviolet–visible (UV–Vis) spectroscopy (Hach DR4000) at wavelength of 554 nm. The RhB removal rate is calculated using the Eq. (2):

$$R = \left(1 - \frac{C_p}{C_f}\right) \times 100\% \quad (2)$$

where  $C_p$  and  $C_f$  are the concentrations of the permeate and feed solutions, respectively. 10 mg/L RhB aqueous solution was used as the feed.

### 2.7. Photocatalytic performance evaluation

The method for photocatalytic performance evaluation is similar to the above-mentioned single filtration test but under light irradiation simultaneously. The visible-light illumination was obtained by removing the UV part of the spectrum from a 300 W Xenon arc lamp using a 420 nm cut-off filter. Filtration and photocatalytic degradation occurred simultaneously during the dynamic process. For comparison, the photocatalytic performance of the  $g\text{-C}_3\text{N}_4/\text{rGO}$  composites in the degradation of RhB was also studied. 40 mg of the catalysts were suspended in 40 mL RhB (5 mg/L) solution in a 100 mL quartz tube. Prior to light irradiation, the suspension was stirred for 30 min in dark to achieve adsorption equilibrium. Then the solution was irradiated from the top through a quartz window while stirring, and an external cooling jacket was employed to absorb heat. The concentration of RhB was monitored at intervals of 30 min by UV–Vis spectroscopy.

## 3. Results and discussion

### 3.1. Characterization of $g\text{-C}_3\text{N}_4/\text{rGO}$ composites

HRTEM images of the as-prepared  $g\text{-C}_3\text{N}_4/\text{rGO}$  and  $g\text{-C}_3\text{N}_4/\text{NT}/\text{rGO}$  composites show that both  $g\text{-C}_3\text{N}_4$  NS and NT are well dispersed onto the rGO NS (Fig. 2). The diameter of the  $g\text{-C}_3\text{N}_4$  NT in Fig. 2d is

around 250 nm. The morphology of the synthesized  $g\text{-C}_3\text{N}_4$  NS and  $g\text{-C}_3\text{N}_4$  NT with higher resolution can be found in Fig. S2. The lattice fringes with an inter planar distance of 0.32 nm corresponding to the (0 0 2) plane of  $g\text{-C}_3\text{N}_4$  were found. The selected area electron diffraction (SAED patterns of  $g\text{-C}_3\text{N}_4$  NS and  $g\text{-C}_3\text{N}_4$  NT revealed that bright continuous concentric rings were attributed to diffraction from the 100 and 002 planes of  $g\text{-C}_3\text{N}_4$  [54]. The similar SAED patterns of  $g\text{-C}_3\text{N}_4/\text{rGO}$  composites demonstrate a homogeneous distribution of  $g\text{-C}_3\text{N}_4$  structures on the rGO sheets (Fig. 2c and f) [39].

Crystal structures of the as-prepared samples were examined using XRD and the interlayer spacing was analyzed by Bragg's Law [55]. The XRD patterns of the  $g\text{-C}_3\text{N}_4$  NS and  $g\text{-C}_3\text{N}_4$  NT powders are similar (Fig. S3). The peak at  $13.0^\circ$  represents the (1 0 0) plane, the packing of tri-s-triazine segments of  $g\text{-C}_3\text{N}_4$  [56]. The strong characteristic (0 0 2) peak at  $27.4^\circ$  corresponds to the interlayer-stacking of the conjugated aromatic system with a stacking distance of 0.32 nm. The characteristic peak of pure GO appears in  $10.5^\circ$ . In Fig. 3a, the XRD pattern of rGO shows a weak characteristic peak at around  $21.2^\circ$  indicating the interlayer space of the as-prepared rGO is 0.42 nm. We find that both  $g\text{-C}_3\text{N}_4$  NS/rGO and  $g\text{-C}_3\text{N}_4$  NT/rGO composites possess weak characteristic peaks at  $15.8^\circ$  and  $27.5^\circ$  which is attributed to the slight shift of the (1 0 0) and (0 0 2) planes. In addition,  $g\text{-C}_3\text{N}_4$  NS/rGO and  $g\text{-C}_3\text{N}_4$  NT/rGO show strong characteristic peaks at  $2\theta = 11.6^\circ$  ( $d$  spacing = 0.76 nm) and  $10.0^\circ$  ( $d$  spacing = 0.85 nm), respectively. The enlarged interlayer distance may be attributed to the intercalation of  $g\text{-C}_3\text{N}_4$  nanomaterials and a similar result was also found by other group [43,45].

Raman spectra are widely used to understand the quality of graphene-based materials [57]. The pristine rGO and the two  $g\text{-C}_3\text{N}_4/\text{rGO}$  composites all exhibit two intense bands at  $1340$  and  $1590\text{ cm}^{-1}$  (Fig. 3b), which are assigned to the D- and G-bands, respectively. The intensity ratio of D- and G-band ( $I_D/I_G$ ) can be used for qualitative analysis of the graphene-based material structure, especially the defect density and size [58]. The method is established on the model that a defect on graphene surface causes a circular structural disorder area (region S), which is surrounded by so-called activated region (region A). The gap between the two regions contribute strongly to the D band, whereas the rest area on graphene outside region S contribute to the G band. Structural disorder region S contribute weakly to the D band

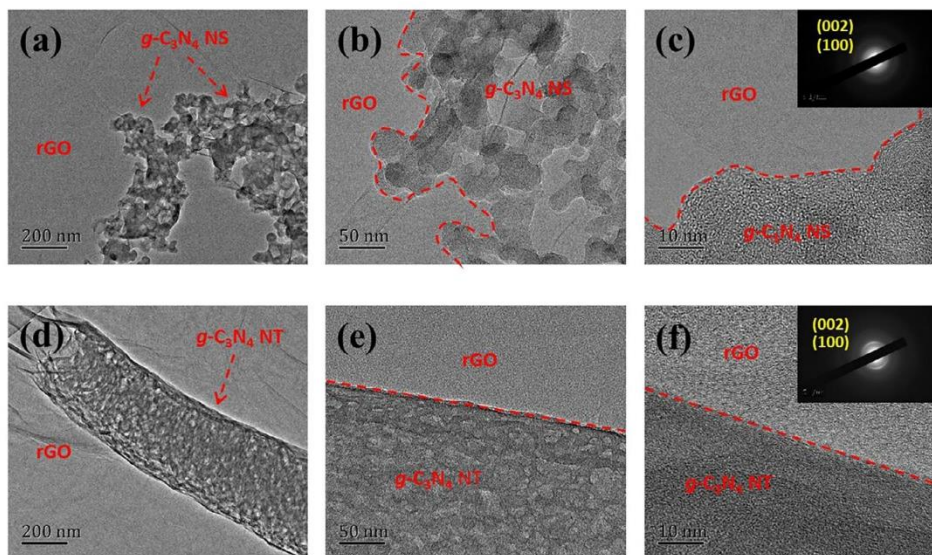


Fig. 2. HRTEM images of  $g\text{-C}_3\text{N}_4$  NS/rGO composite (a)–(c), and  $g\text{-C}_3\text{N}_4$  NT/rGO composite (d)–(e). The insets of Fig. 1c and f are the corresponding SAED patterns.



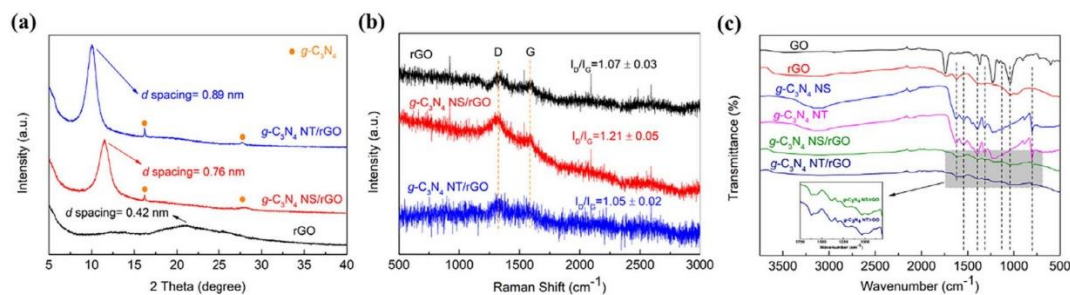


Fig. 3. (a) XRD patterns, (b) Raman spectra and (c) FTIR spectra of the rGO,  $g\text{-C}_3\text{N}_4$  NS,  $g\text{-C}_3\text{N}_4$  NT,  $g\text{-C}_3\text{N}_4$  NS/rGO, and  $g\text{-C}_3\text{N}_4$  NT/rGO composites.

owing to breakdown of the lattice structure itself. We found that the  $I_D/I_G$  of  $g\text{-C}_3\text{N}_4$  NT/rGO of  $1.05 \pm 0.02$  is close to the value of pristine rGO ( $1.07 \pm 0.03$ ), whereas for  $g\text{-C}_3\text{N}_4$  NS/rGO it is  $1.21 \pm 0.05$ . This may indicate that intercalating 2D  $g\text{-C}_3\text{N}_4$  NS into rGO NS leads to significant structural disorder on the rGO surface, because some of  $g\text{-C}_3\text{N}_4$  NS induced defects may overlap and improve the possibility of defect density.

FTIR experiments were conducted to verify changes in chemical state of the as-prepared samples (Fig. 3c). Peaks of GO at  $1037\text{ cm}^{-1}$ ,  $1223\text{ cm}^{-1}$ ,  $1619\text{ cm}^{-1}$ ,  $1738\text{ cm}^{-1}$  and  $1630\text{ cm}^{-1}$  correspond to C–O, C–OH, C=C, C–O, and O–H bonds, respectively [59]. In the FTIR spectra for rGO, the peaks representing the above-mentioned oxygen-containing functional groups were weak and some of them were even absent, indicating that GO was successfully reduced into rGO by ultraviolet irradiation. The spectra of  $g\text{-C}_3\text{N}_4$  NS and  $g\text{-C}_3\text{N}_4$  NT are identical and the peaks occurring in the  $1600\text{--}1200\text{ cm}^{-1}$  region are ascribed to the stretching modes of C–N heterocycles [44]. The characteristic stretching of triazine units centered at  $810\text{ cm}^{-1}$  is observed. The spectra of the two  $g\text{-C}_3\text{N}_4$ /rGO composites display all characteristic peaks in  $g\text{-C}_3\text{N}_4$  and rGO.

To further understand the chemical composition of the  $g\text{-C}_3\text{N}_4$  NS/rGO and  $g\text{-C}_3\text{N}_4$  NT/rGO composites, XPS analysis was conducted. The rGO does not contain nitrogen element (Table S1), therefore the new peak of N1s emerged in the XPS spectra of  $g\text{-C}_3\text{N}_4$ /rGO composites suggests the incorporation of  $g\text{-C}_3\text{N}_4$  into the framework of  $g\text{-C}_3\text{N}_4$ /rGO composites. Fig. 4a shows the wide scan XPS spectra of the two  $g\text{-C}_3\text{N}_4$ /rGO composites. Fig. 4b–f are the C1s, O1s and N1s XPS core-level spectra of  $g\text{-C}_3\text{N}_4$  NS/rGO and  $g\text{-C}_3\text{N}_4$  NT/rGO. In Fig. 4b and c, the C1s spectrum of the two  $g\text{-C}_3\text{N}_4$ /rGO composites exhibit three peaks at about 284.6, 286.7, and 288.4 eV, which are attributed to C–C, C–O and C=O/C–N=C, respectively [45]. Fig. 4d depicts the O1s spectrum of the two  $g\text{-C}_3\text{N}_4$ /rGO composites and the broad peak observed at 532.5 eV corresponds to the surface oxygen complexes in the carbon phase. The N1s XPS spectrum of the two  $g\text{-C}_3\text{N}_4$ /rGO composites could be deconvoluted into three peaks at 398.8, 399.5 and 401.3 eV, demonstrating three main types of N bonding in the samples (Fig. 4e–f). The peaks centered at 398.8 eV and 399.5 eV are attributed to the  $\text{sp}^2$ -bonded aromatic N in triazine rings and bridged N–(C)<sub>3</sub>, respectively. The peak at 401.3 eV corresponds to the  $\text{–NH}_2$  or  $\text{=NH}$  groups. Positive charge localization in C–N heterocycles were found at  $\sim 404.9\text{ eV}$  [39]. All peaks of the XPS spectrum of  $g\text{-C}_3\text{N}_4$  NS/rGO occur at similar positions as for  $g\text{-C}_3\text{N}_4$  NT/rGO, but the proportions of each species are different. Elemental analysis of the two  $g\text{-C}_3\text{N}_4$ /rGO composites is in Table S1. Compared with the C and O atomic ratios of rGO (77.16% and 22.84%, respectively), it is also found that carbon content in the two composites is a little higher while oxygen content in the two composites is lower, with the values of 17.96% for  $g\text{-C}_3\text{N}_4$  NS/rGO and 18.35% for  $g\text{-C}_3\text{N}_4$  NS/rGO. The N atomic ratios are calculated to be around 3.21% and 1.84% for  $g\text{-C}_3\text{N}_4$  NS/rGO and  $g\text{-C}_3\text{N}_4$  NT/rGO, respectively. This indicates that  $g\text{-C}_3\text{N}_4$  NS is easier to adsorb onto rGO than  $g\text{-C}_3\text{N}_4$  NT.

### 3.2. Characterization of $g\text{-C}_3\text{N}_4$ /rGO composite membranes

The surface and cross-sectional morphologies of rGO and the composite membranes were observed using SEM. Fig. 5a shows the pristine rGO membrane surface layer-by-layer assembled by rGO monolayer and a fluctuant surface with silk veil waves is observed. As seen from the cross-sectional images, the rGO skin layer shows a crumpled laminar nanostructure with thickness of  $\sim 700\text{ nm}$ . The laminar structure is mostly attributed to the oxygenated groups and interlayer spacing and the nanosheet folding effect during the deposition [60]. To further investigate the elemental distribution of the membrane surface, elemental mapping was undertaken. A uniform distribution of carbon and oxygen element was found on the membrane surface of the rGO membrane (Fig. 5a). Fig. 5b and c show the morphologies of the two  $g\text{-C}_3\text{N}_4$ /rGO composite membranes and their surface elemental mapping results, respectively. It is found that intercalating 1D  $g\text{-C}_3\text{N}_4$  NT or 2D  $g\text{-C}_3\text{N}_4$  NS into rGO significantly altered the surface and cross-section structure. More apparent large wrinkles were observed on the two types of composite membrane surfaces and the thickness of the two  $g\text{-C}_3\text{N}_4$ /rGO composite layers increased compared with that of pristine rGO layer. Besides carbon and oxygen, nitrogen from the  $g\text{-C}_3\text{N}_4$  NS or  $g\text{-C}_3\text{N}_4$  NT is detected on the surface of the two  $g\text{-C}_3\text{N}_4$ /rGO membranes, which confirms that the  $g\text{-C}_3\text{N}_4$  NS and NT were successfully incorporated onto the rGO NS.

To investigate the surface roughness of rGO and the two types of composite membranes, the three membrane surfaces were characterized by AFM. Three-dimensional AFM images and roughness parameters of these membranes (Fig. 6) show a sand dune-like surface structures with high roughness degree. Clear valleys and gullies were observed on the three surfaces. It was found that the two types of  $g\text{-C}_3\text{N}_4$ /rGO composite membranes showing higher arithmetical roughness ( $R_a$ ) and root mean squared roughness (RMS) values than that of pristine rGO membrane. This indicates that much larger wrinkles were formed in the composite membranes, which is consistent with the above-mentioned SEM images. We speculate that more wrinkles were generated in the rGO crumpled laminar nanostructure by intercalating 1D or 2D nanoscale  $g\text{-C}_3\text{N}_4$  into the scaffold. The  $g\text{-C}_3\text{N}_4$  NS/rGO membrane has the roughest surface among the three, which may be attributed to locally anisotropic stacking aggregation of  $g\text{-C}_3\text{N}_4$  NS, corroborating the Raman results.

The chemical state of rGO and the composite membranes were confirmed by FTIR. The two types of composite membranes show identical FTIR spectrum with the same representative peaks contributed by rGO and  $g\text{-C}_3\text{N}_4$  (Fig. 7). The new peak at approximately  $625\text{ cm}^{-1}$  is attributed to C–C stretching vibration from additional ethylenediamine, which has been proved to be an effective cross-linker to bond rGO NS. A nucleophilic reaction can take place between the amines of ethylenediamine and the epoxide rings of  $\text{rGO}^{14}$ .

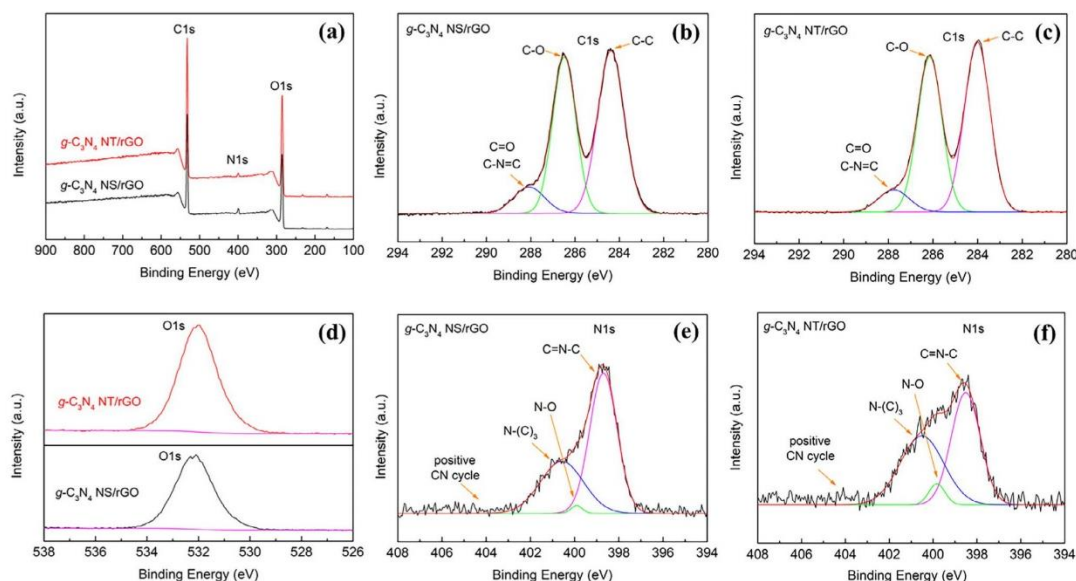


Fig. 4. XPS of the  $g\text{-C}_3\text{N}_4/\text{GO}$  composites: (a) wide-scan; (b) and (c) C1s core-level; (d) O1s core-level; (e) and (f) N1s core-level.

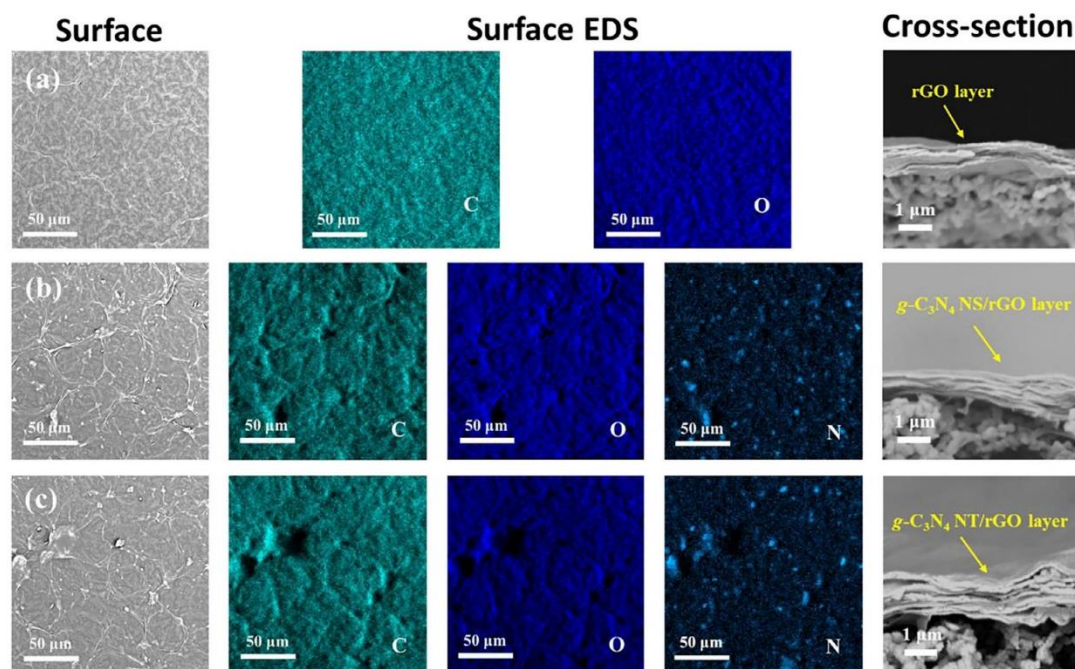


Fig. 5. SEM images and the corresponding EDS images of (a) rGO membrane, (b)  $g\text{-C}_3\text{N}_4\text{ NS/rGO}$  composite membrane and (c)  $g\text{-C}_3\text{N}_4\text{ NT/rGO}$  composite membrane. Inserts: cross-sectional SEM images of the three membranes.

### 3.3. Evaluation of $g\text{-C}_3\text{N}_4/\text{rGO}$ composite membranes

The wettability of rGO and the surfaces of the composite membranes was characterized by water contact angle measurement. As shown in Fig. 8a, the pure water contact angle (WCA) of the as-prepared pristine rGO membrane is  $73.7 \pm 1.2^\circ$ . The WCA of the  $g\text{-C}_3\text{N}_4\text{ NS/rGO}$  and  $g\text{-C}_3\text{N}_4\text{ NT/rGO}$  membrane surfaces are  $73.3 \pm 0.8^\circ$  and  $74.3 \pm 1.0^\circ$ , respectively.

It seems that integrating small amounts of  $g\text{-C}_3\text{N}_4$  into rGO did not induce any significant effect on the wettability of the rGO surface. To reveal the role of 1D  $g\text{-C}_3\text{N}_4\text{ NT}$  and 2D  $g\text{-C}_3\text{N}_4\text{ NS}$  on the rGO laminar structure for water transport, the pure water permeability of the three membranes was evaluated in a dead-end membrane



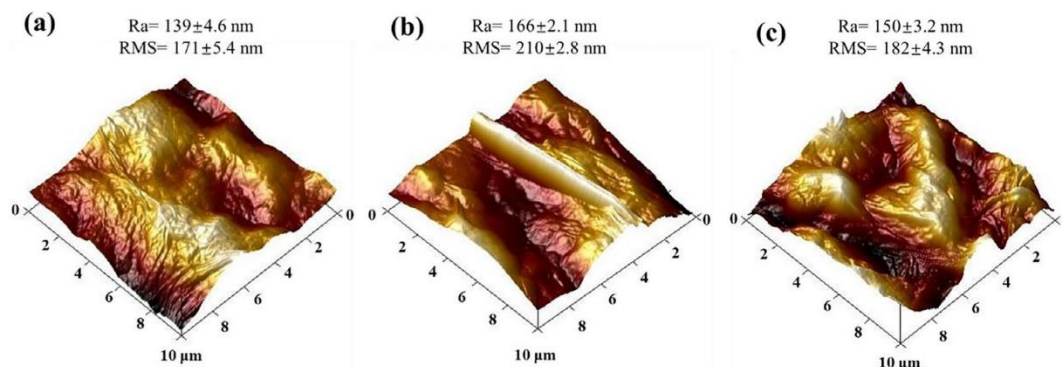


Fig. 6. AFM images of (a) rGO membrane, (b)  $g\text{-C}_3\text{N}_4$  NS/rGO composite membrane and (c)  $g\text{-C}_3\text{N}_4$  NT/rGO composite membrane with calculated roughness values.

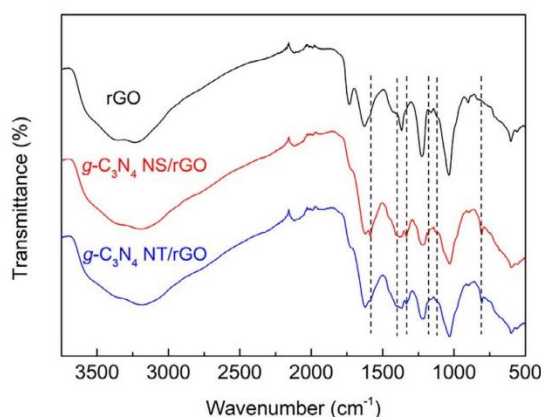


Fig. 7. FTIR spectra of the rGO and  $g\text{-C}_3\text{N}_4$ /rGO composite membranes.

configuration. Although the three membranes are similar in wettability, their pure water permeability increases with incorporation of  $g\text{-C}_3\text{N}_4$  NS and  $g\text{-C}_3\text{N}_4$  NT. The pure water permeability of the rGO membrane is  $2.31 \text{ L m}^{-2} \text{ h}^{-1} \text{ bar}^{-1}$ , and that of the  $g\text{-C}_3\text{N}_4$  NS/rGO membrane is up to  $3.53 \text{ L m}^{-2} \text{ h}^{-1} \text{ bar}^{-1}$ . Notably, the pure water permeability of  $g\text{-C}_3\text{N}_4$  NT/rGO ( $4.87 \text{ L m}^{-2} \text{ h}^{-1} \text{ bar}^{-1}$ ) is twice as high as that of pristine rGO membrane (Fig. 8a). Generally, high hydrophilicity of membrane

surfaces leads to high water permeability. Therefore, the enhanced water permeability of the two types of  $g\text{-C}_3\text{N}_4$ /rGO composite membranes might be attributed to the newly constructed composite laminar structures.

Since the amount of rGO building blocks and the amount of  $g\text{-C}_3\text{N}_4$  NS or  $g\text{-C}_3\text{N}_4$  NT deposited on the rGO were kept identical in this study, we found that the rGO laminar structure intercalated by low content of 1D  $g\text{-C}_3\text{N}_4$  NT shows better water transport performance in comparison with the pure rGO and  $g\text{-C}_3\text{N}_4$  NS/rGO. This might be explained by two reasons. Firstly, 1D intercalation is more beneficial than 2D intercalation for the rGO laminar structure in water transport. The 1D  $g\text{-C}_3\text{N}_4$  NT with larger size in diameter can readily enlarge the local interlayer spacing of rGO laminates providing fast water channels inside its laminar structure. Secondly, although more 2D  $g\text{-C}_3\text{N}_4$  NS were intercalated into the laminar structure and more sites with enlarged interlayer spacing were created, the stacking aggregation of  $g\text{-C}_3\text{N}_4$  NS with anisotropic wrinkles increased the resistance to water flow.

To evaluate the separation performance of the as-prepared membranes, filtration tests were conducted in both dark and light conditions (Fig. 8b). RhB dye was used as a model pollutant owing to its relatively small molecular weight and electroneutral property to exclude electrostatic effect and stability during integrated filtration and photodegradation under visible light irradiation. Without light irradiation, we found that the water permeability of the rGO and the composite membranes remained similar as the test results for pure water, but the membranes with 1D and 2D  $g\text{-C}_3\text{N}_4$  intercalation led to a continuous drop in RhB removal rate. In the dark filtration tests, rGO membranes

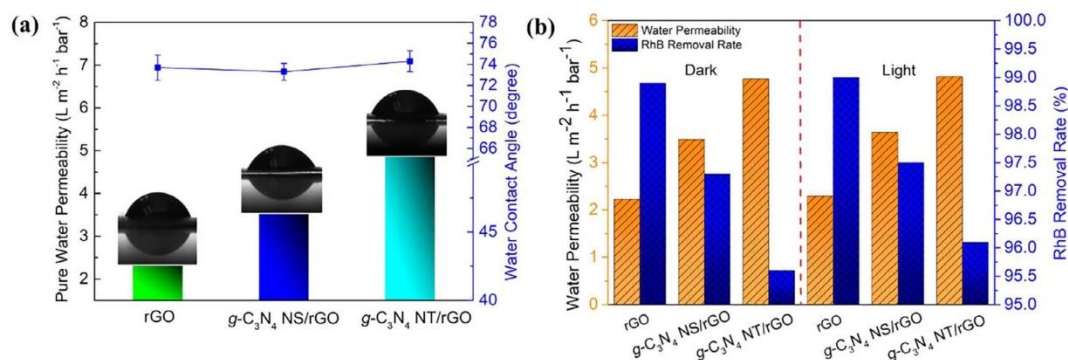


Fig. 8. (a) Pure water permeability and water contact angles of the as-prepared rGO and  $g\text{-C}_3\text{N}_4$ /rGO composite membranes; (b) RhB removal rates of the as-prepared rGO and  $g\text{-C}_3\text{N}_4$ /rGO composite membranes under dark and light conditions.



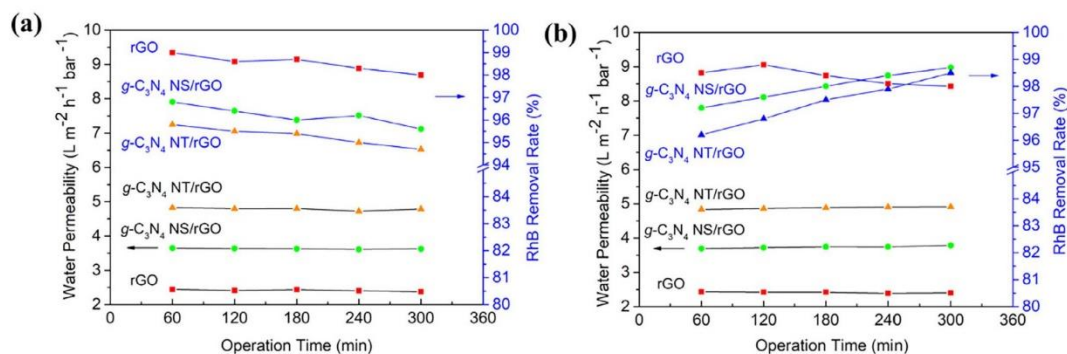


Fig. 9. RhB removal rates for the as-prepared rGO and  $g\text{-C}_3\text{N}_4/\text{rGO}$  composite membranes without (a) and with (b) visible-light irradiation for 5 h.

show a water permeability of  $2.26 \text{ L}\cdot\text{m}^{-2}\cdot\text{h}^{-1}\cdot\text{bar}^{-1}$  and RhB removal rate of 98.9%. Under the same conditions, the water permeability of  $g\text{-C}_3\text{N}_4 \text{ NS/rGO}$  and  $g\text{-C}_3\text{N}_4 \text{ NT/rGO}$  membranes are 3.49 and  $4.77 \text{ L}\cdot\text{m}^{-2}\cdot\text{h}^{-1}\cdot\text{bar}^{-1}$ , respectively. Their RhB removal rates are 97.3% and 95.6%, respectively. However, upon visible-light irradiation, the prepared rGO,  $g\text{-C}_3\text{N}_4 \text{ NS/rGO}$  and  $g\text{-C}_3\text{N}_4 \text{ NT/rGO}$  membranes showed slight increases in water permeability, i.e. 2.29, 3.64 and  $4.81 \text{ L}\cdot\text{m}^{-2}\cdot\text{h}^{-1}\cdot\text{bar}^{-1}$ , respectively. RhB removal rates also slightly increased (rGO membrane of 99.0%,  $g\text{-C}_3\text{N}_4 \text{ NS/rGO}$  membrane of 97.5% and  $g\text{-C}_3\text{N}_4 \text{ NT/rGO}$  membrane of 96.1%).

We hypothesized that the introduction of  $g\text{-C}_3\text{N}_4$  photocatalysts could improve the water permeability and removal rate for organic pollutants. To validate whether or not photodegradation occurs during the filtration process, a long-term operation performance of the membranes was undertaken for 5 h. Fig. 9a depicts the separation performance of the three prepared membranes in RhB filtration without and with visible-light irradiation. We found that the water permeability of the rGO membrane remained stable with negligible fluctuations during the operating period regardless of dark or light conditions. However, the water permeability of the two types of  $g\text{-C}_3\text{N}_4/\text{rGO}$  composite membranes exhibited a slight increase with the running time. The long-term operation stability of the three membranes might be attributed to the introduction of cross-linker when the membranes were assembled.

RhB removal rates over the three membranes without visible-light irradiation exhibited a downward tendency with the time (Fig. 9a), whereas RhB removal rates of  $g\text{-C}_3\text{N}_4 \text{ NS/rGO}$  membrane and  $g\text{-C}_3\text{N}_4 \text{ NT/rGO}$  membrane under light irradiation improved from 97.2% to 98.7% and 96.2% to 98.5%, respectively (Fig. 9b). The unique separation performance of  $g\text{-C}_3\text{N}_4/\text{rGO}$  composite membranes may be caused by the intercalation of  $g\text{-C}_3\text{N}_4$  nanomaterials into rGO laminates, and the composite membranes could simultaneously photodegrade RhB during the filtration process. We deduce that RhB removal is mainly based on molecular sieving within the rGO-dominated laminar structure. Notably, the content of  $g\text{-C}_3\text{N}_4 \text{ NT}$  in the  $g\text{-C}_3\text{N}_4 \text{ NT/rGO}$  membrane is lower than that of  $g\text{-C}_3\text{N}_4 \text{ NS}$  in the  $g\text{-C}_3\text{N}_4 \text{ NT/rGO}$  membrane, but the RhB removal rate of  $g\text{-C}_3\text{N}_4 \text{ NT/rGO}$  membrane was improved more significantly than that of  $g\text{-C}_3\text{N}_4 \text{ NS/rGO}$  membrane. This result indicates that the as-prepared  $g\text{-C}_3\text{N}_4 \text{ NT}$  showed better photocatalytic activity compared with that of the  $g\text{-C}_3\text{N}_4 \text{ NS}$  photocatalyst.

Table 1 compares dye-containing wastewater treatment performance of our composite membranes with that of other recently reported NF membranes. When APT nanorods were intercalated into GO laminates via grafting modification, the water permeability of APT/GO membrane sharply increases to about  $10 \text{ L}\cdot\text{m}^{-2}\cdot\text{h}^{-1}\cdot\text{bar}^{-1}$  with preserving high rejection to dyes [27]. Similarly, Chen et al. [35] successfully developed a series of polyamide (PA)/GO NF membranes and then they investigated the effect of intercalating different nanomaterials into GO laminar structures on the separation performance of the

Table 1

Comparison of the as-prepared membranes in this work with other reported membranes in terms of organic dyes removal rates.

Membrane	WP ( $\text{LMH}\cdot\text{bar}^{-1}$ )	Dye	Removal (%)	Refs.
APT/GO	~9.9	RhB	80	[27]
PA 6/GO (120)	7.62	MO	99.47	[35]
PA 6/GO (120)/TiO <sub>2</sub>	13.77	MO	99.36	[35]
PA 6/GO (120)/SiO <sub>2</sub>	11.39	MO	99.62	[35]
PA 6/GO (120)/Si <sub>3</sub> N <sub>4</sub>	14.82	MO	99.28	[35]
CNT/rGO	13	MO	98.2	[61]
PDA/rGO/HNT	9.95	MB	99.7	[29]
UiO-66/rGO	14.4	RhB	98.2	[22]
$\alpha\text{-Fe}_2\text{O}_3/\text{rGO}/\text{PAN}$	N/A	RhB	69.2	[63]
$\beta\text{-FeOOH}/\text{PDA}/\text{PEI}$	~9.97	RhB	77.3	[62]
rGO	2.26	RhB	98.9	This work
$g\text{-C}_3\text{N}_4 \text{ NS/rGO}$ (light)	3.49	RhB	98.7	This work
$g\text{-C}_3\text{N}_4 \text{ NT/rGO}$ (light)	4.77	RhB	98.5	This work

Abbreviations: WP, water permeability; LHM =  $\text{L}\cdot\text{m}^{-2}\cdot\text{h}^{-1}\cdot\text{bar}^{-1}$ ; MO, methyl orange; MB, methylene blue; APT, attapulgite; PA, polyamide.

membranes. They also found the intercalation can improve the water permeabilities ( $11.39\text{--}14.82 \text{ L}\cdot\text{m}^{-2}\cdot\text{h}^{-1}\cdot\text{bar}^{-1}$ ) of their membranes while maintaining high dyes removal efficiencies (above 99%). In addition, 1D carbon or hallysite NTs and 3D UiO-66 were used to improve rGO NF membranes and these membranes also exhibited excellent performance in purifying dye-containing wastewater [22,29,61]. Although it has been demonstrated that intercalating different dimensional nano-spacers into GO-based laminar structures is an efficient strategy to tuning the separation performance of the resultant rGO membranes, the long-term operation stability and antifouling property of those membranes could not be ignored.

Constructing NF membrane materials with photo-induced self-cleaning property gives a rise to an emerging organic contaminant-polluted water purification technology. In 2017, Lv et al. [62] prepared a  $\beta\text{-FeOOH}$  nanorods doped PDA/polyethyleneimine (PEI) photocatalytic NF membrane with high water permeability and enhanced RhB removal performance, but their RhB removal rate was still unsatisfied. Shortly thereafter, Pan's group also reported a  $\alpha\text{-Fe}_2\text{O}_3/\text{rGO}/\text{polyacrylonitrile}$  (PAN) nanofiber membrane for the treatment of dye polluting water [63]. Their photocatalytic experiments show that their membrane can effectively degrade a variety of organic dyes, among which the degradation rate of  $20 \text{ mg/mL}$  RhB is 69.2% within 2 h. However, they didn't report any membrane filtration results. Development of robust photocatalytic NF membranes with both high permeability and organic pollutants removal efficiency is still lack of exploration. Our  $g\text{-C}_3\text{N}_4/\text{rGO}$  composite NF membranes show relatively low water permeability yet high RhB removal rate and excellent long-term stability. Therefore, the performance of our  $g\text{-C}_3\text{N}_4/\text{rGO}$  composite

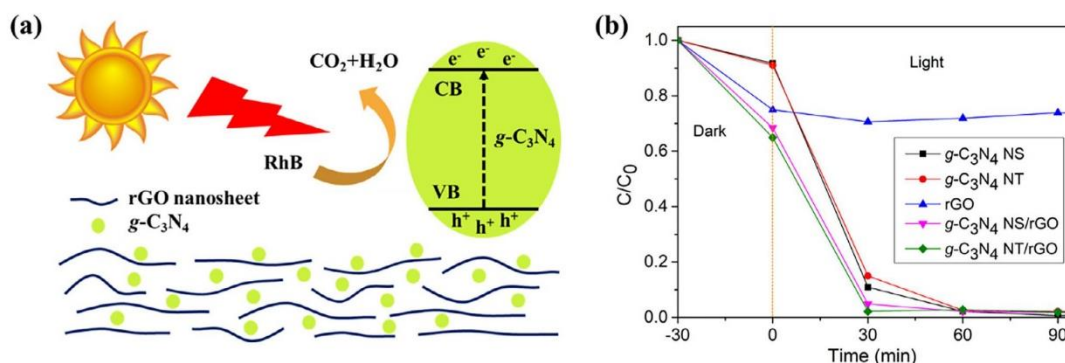
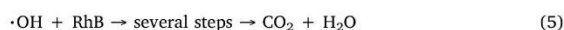
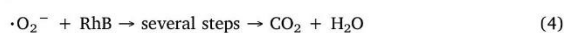


Fig. 10. (a) Schematic illustration of self-cleaning mechanism for the  $g\text{-C}_3\text{N}_4/\text{rGO}$  composite membranes and (b) photocatalytic activities of the  $g\text{-C}_3\text{N}_4$  and their composite photocatalysts.

NF membranes, especially the  $g\text{-C}_3\text{N}_4$  NT/rGO membrane, is relatively competitive when applied to purify dye-containing wastewater.

### 3.4. Self-cleaning mechanism

The possible self-cleaning mechanism is given in Fig. 10a. As reported previously, GO and GO-based membranes generally show high adsorption capacity [64]. We hypothesized that RhB dyes can be easily adsorbed onto the composite membranes and uniformly distributed on the surfaces of  $g\text{-C}_3\text{N}_4$  and rGO NS. The UV–Vis diffuse reflectance analysis determines that the band gaps of  $g\text{-C}_3\text{N}_4$  NS/rGO and  $g\text{-C}_3\text{N}_4$  NT/rGO are 2.41 eV and 1.98 eV, respectively (Fig. S4). The photocatalytic reaction schemes are given below:



Under visible-light irradiation,  $g\text{-C}_3\text{N}_4$  can generate  $\pi\text{-}\pi^*$  electronic transition and transfer the excited-state electrons from the valence band (VB) to the conduction band (CB) [42]. Then the electrons ( $e^-$ ) accumulate in the CB and holes ( $h^+$ ) are generated in the VB. The electrons and holes react with oxygen and water to produce superoxide radicals and hydroxyl radicals, respectively, which will oxidize the adsorbed RhB due to their high oxidative capacity [39].

It was reported that the photo-generated electrons can be easily migrated from  $g\text{-C}_3\text{N}_4$  to the rGO NS because of its remarkable electron conductivity and high electron storage capacity [65]. The photoluminescence (PL) analysis also confirmed that  $g\text{-C}_3\text{N}_4/\text{rGO}$  composites could inhibit the photogenerated carrier recombination leading to enhanced light utilization and photocatalytic efficiency. The  $g\text{-C}_3\text{N}_4$  NT/rGO shows the best photocatalytic performance among the nanocomposites (Fig. S5). Therefore, the superior self-cleaning property of  $g\text{-C}_3\text{N}_4/\text{rGO}$  composite membranes may be attributed to the enhanced dye adsorption capacity, promoted light harvesting ability and fast transfer of photo-generated electrons at the  $g\text{-C}_3\text{N}_4/\text{rGO}$  surface.

To further reveal the photo-induced self-cleaning properties of the as-prepared  $g\text{-C}_3\text{N}_4/\text{rGO}$  composite membranes, the RhB adsorption and photodegradation activities of rGO,  $g\text{-C}_3\text{N}_4$  and their composites were studied. After 30 min stirring without light irradiation, RhB can adsorb onto all the tested materials (Fig. 10b). Only about 8% of RhB dyes were adsorbed for the two types of  $g\text{-C}_3\text{N}_4$  photocatalysts, whereas

the  $g\text{-C}_3\text{N}_4/\text{rGO}$  composites showed largely improved adsorption capacity for RhB. Approximately 32% and 36% of RhB were adsorbed onto  $g\text{-C}_3\text{N}_4$  NS/rGO and  $g\text{-C}_3\text{N}_4$  NT/rGO, respectively. The rGO material can only adsorb around 25% of RhB and no photocatalytic performance was found. However, the two  $g\text{-C}_3\text{N}_4$  nanomaterials and the two  $g\text{-C}_3\text{N}_4/\text{rGO}$  composites exhibited excellent photocatalytic activities. RhB was completely photodegraded within 60 min, and the photodegradation efficiency of the composites is higher than that of the bare  $g\text{-C}_3\text{N}_4$  photocatalysts, which is consistent with the PL analysis. After dark adsorption and subsequent visible-light irradiation for 30 min, 97.8% of RhB was removed by the as-prepared  $g\text{-C}_3\text{N}_4$  NT/rGO and 95.1% for the  $g\text{-C}_3\text{N}_4$  NS/rGO. These results further confirm that adsorption and photodegradation leads to the self-cleaning properties of the as-prepared  $g\text{-C}_3\text{N}_4/\text{rGO}$  composite membranes. In addition, the better photocatalytic activity of  $g\text{-C}_3\text{N}_4$  NT/rGO explains the better performance of  $g\text{-C}_3\text{N}_4$  NT/rGO membranes in the integrated photocatalytic filtration process as discussed in Section 3.3.

## 4. Conclusions

In summary, photo-induced self-cleaning  $g\text{-C}_3\text{N}_4/\text{rGO}$  composite nanofiltration membranes were successfully fabricated by intercalating 1D  $g\text{-C}_3\text{N}_4$  NT or 2D  $g\text{-C}_3\text{N}_4$  NS photocatalysts into rGO laminates. The  $g\text{-C}_3\text{N}_4/\text{rGO}$  composite membrane modified by 1D  $g\text{-C}_3\text{N}_4$  NT was reported for the first time. Different dimensional intercalation of  $g\text{-C}_3\text{N}_4$  photocatalysts for rGO membranes was comparatively investigated for water transport and dye-contaminated water purification. We found that 1D intercalation exhibits more advantages over 2D intercalation for the nanocomposites. The rGO membrane with  $g\text{-C}_3\text{N}_4$  NT exhibited higher water permeability ( $4.87 \text{ L m}^{-2} \text{ h}^{-1} \text{ bar}^{-1}$ ) than that with  $g\text{-C}_3\text{N}_4$  NS ( $3.53 \text{ L m}^{-2} \text{ h}^{-1} \text{ bar}^{-1}$ ). The NF and photodegradation of dye contaminants can be achieved in one integrated process for both composite membranes. Upon visible-light irradiation, the RhB removal rates of both composite membranes are above 98% in long-term operation. The photo-induced self-cleaning mechanism for the  $g\text{-C}_3\text{N}_4/\text{rGO}$  composite membranes was established. This study demonstrates that the  $g\text{-C}_3\text{N}_4$  NT/rGO composite membrane is a promising candidate for water purification and intercalating 1D nanoscale photocatalysts into rGO membranes offers a new strategy for developing efficient photocatalytic membrane materials.

## Acknowledgements

Y. Wei thanks the Australian Government for his International Research Training Program (iRTP) scholarship. Financial support by the ARC Discovery Project (DP140102432), and China Scholarship Council



Scholarship for Y. Zhu is gratefully acknowledged. The use of the Microscopy Unit, Faculty of Science and Engineering at Macquarie University, Australia is acknowledged. We also thank Dr. Chao Shen from the Microscopy Unit, for technical assistance with microscopy. Anonymous reviewers are acknowledged for their suggestions and comments that helped us to improve the quality of this work.

### Conflict of interest

The authors declare that they have no conflict of interest.

### Appendix A. Supplementary data

Supplementary data to this article can be found online at <https://doi.org/10.1016/j.cej.2018.09.108>.

### References

- [1] A.G. Fane, R. Wang, M.X. Hu, Synthetic membranes for water purification: status and future, *Angew. Chem. Int. Ed.* 54 (2015) 3368–3386.
- [2] A. Lee, J.W. Elam, S.B. Darling, Membrane materials for water purification: design, development, and application, *Environ. Sci. Water Res. Technol.* 2 (2016) 17–42.
- [3] H.M. Hegab, L. Zou, Graphene oxide-assisted membranes: fabrication and potential applications in desalination and water purification, *J. Membr. Sci.* 484 (2015) 95–106.
- [4] H. Guo, S. Zhao, X. Wu, H. Qi, Fabrication and characterization of  $\text{TiO}_2/\text{ZrO}_2$  ceramic membranes for nanofiltration, *Microp. Mesop. Mater.* 260 (2018) 125–131.
- [5] Y. Du, Y. Lv, W.Z. Qiu, J. Wu, Z.K. Xu, Nanofiltration membranes with narrowed pore size distribution via pore wall modification, *Chem. Commun.* 52 (2016) 8589–8592.
- [6] Y. Zhang, T.-S. Chung, Graphene oxide membranes for nanofiltration, *Curr. Opin. Chem. Eng.* 16 (2017) 9–15.
- [7] J. Wang, Y. Wang, J. Zhu, Y. Zhang, J. Liu, B. Van der Bruggen, Construction of  $\text{TiO}_2$ @graphene oxide incorporated antifouling nanofiltration membrane with elevated filtration performance, *J. Membr. Sci.* 533 (2017) 279–288.
- [8] G. Liu, W. Jin, N. Xu, Graphene-based membranes, *Chem. Soc. Rev.* 44 (2015) 5016–5030.
- [9] K.C. Kemp, H. Seema, M. Saleh, N.H. Le, K. Mahesh, V. Chandra, K.S. Kim, Environmental applications using graphene composites: water remediation and gas adsorption, *Nanoscale* 5 (2013) 3149–3171.
- [10] F. Perreault, A. Fonseca de Faria, M. Elimelech, Environmental applications of graphene-based nanomaterials, *Chem. Soc. Rev.* 44 (2015) 5861–5896.
- [11] J. Shen, G. Liu, K. Huang, Z. Chu, W. Jin, N. Xu, Subnanometer two-dimensional graphene oxide channels for ultrafast gas sieving, *ACS Nano* 10 (2016) 3398–3409.
- [12] J.C. Zhu, X.X. Meng, J.P. Zhao, Y. Jin, N.T. Yang, S.G. Zhang, J. Sunarso, S.M. Liu, Facile hydrogen/nitrogen separation through graphene oxide membranes supported on YSZ ceramic hollow fibers, *J. Membr. Sci.* 535 (2017) 143–150.
- [13] Y. Lou, G. Liu, S. Liu, J. Shen, W. Jin, A facile way to prepare ceramic-supported graphene oxide composite membrane via silane-graft modification, *Appl. Surf. Sci.* 307 (2014) 631–637.
- [14] X.L. Xu, F.W. Lin, Y. Du, X. Zhang, J. Wu, Z.K. Xu, Graphene oxide nanofiltration membranes stabilized by cationic porphyrin for high salt rejection, *ACS Appl. Mater. Interface* 8 (2016) 12588–12593.
- [15] N. Meng, W. Zhao, E. Shamsaei, G. Wang, X. Zeng, X. Lin, T. Xu, H. Wang, X. Zhang, A low-pressure GO nanofiltration membrane crosslinked via ethylenediamine, *J. Membr. Sci.* 548 (2018) 363–371.
- [16] H. Shen, N. Wang, K. Ma, L. Wang, G. Chen, S. Ji, Tuning inter-layer spacing of graphene oxide laminates with solvent green to enhance its nanofiltration performance, *J. Membr. Sci.* 527 (2017) 43–50.
- [17] Y. Yuan, X. Gao, Y. Wei, X. Wang, J. Wang, Y. Zhang, C. Gao, Enhanced desalination performance of carboxyl functionalized graphene oxide nanofiltration membranes, *Desalination* 405 (2017) 29–39.
- [18] L. Chen, J.-H. Moon, X. Ma, L. Zhang, Q. Chen, L. Chen, R. Peng, P. Si, J. Feng, Y. Li, J. Lou, L. Ci, High performance graphene oxide nanofiltration membrane prepared by electrospraying for wastewater purification, *Carbon* 130 (2018) 487–494.
- [19] L. Chen, Y. Li, L. Chen, N. Li, C. Dong, Q. Chen, B. Liu, Q. Ai, P. Si, J. Feng, L. Zhang, J. Suhr, J. Lou, L. Ci, A large-area free-standing graphene oxide multilayer membrane with high stability for nanofiltration applications, *Chem. Eng. J.* 345 (2018) 536–544.
- [20] Y. Zhan, X. Wan, S. He, Q. Yang, Y. He, Design of durable and efficient poly(arylene ether nitrile)/bioinspired polydopamine coated graphene oxide nanofibrous composite membrane for anionic dyes separation, *Chem. Eng. J.* 333 (2018) 132–145.
- [21] D. Hua, T.-S. Chung, Polyelectrolyte functionalized lamellar graphene oxide membranes on polypropylene support for organic solvent nanofiltration, *Carbon* 122 (2017) 604–613.
- [22] K. Guan, D. Zhao, M. Zhang, J. Shen, G. Zhou, G. Liu, W. Jin, 3D nanoporous crystals enabled 2D channels in graphene membrane with enhanced water purification performance, *J. Membr. Sci.* 542 (2017) 41–51.
- [23] Z. Jia, Y. Wang, W. Shi, J. Wang, Diamines cross-linked graphene oxide free-standing membranes for ion dialysis separation, *J. Membr. Sci.* 520 (2016) 139–144.
- [24] P. Zhang, J.-L. Gong, G.-M. Zeng, C.-H. Deng, H.-C. Yang, H.-Y. Liu, S.-Y. Huan, Cross-linking to prepare composite graphene oxide-framework membranes with high-flux for dyes and heavy metal ions removal, *Chem. Eng. J.* 322 (2017) 657–666.
- [25] H. Liu, H. Wang, X. Zhang, Facile fabrication of freestanding ultrathin reduced graphene oxide membranes for water purification, *Adv. Mater.* 27 (2015) 249–254.
- [26] G. Liu, W. Jin, N. Xu, Two-dimensional-material membranes: a new family of high-performance separation membranes, *Angew. Chem. Int. Ed.* 55 (2016) 13384–13397.
- [27] C.-Y. Wang, W.-J. Zeng, T.-T. Jiang, X. Chen, X.-L. Zhang, Incorporating attapulgite nanorods into graphene oxide nanofiltration membranes for efficient dyes wastewater treatment, *Sep. Purif. Technol.* (2018).
- [28] P. Zhang, J.L. Gong, G.M. Zeng, B. Song, H.Y. Liu, S.Y. Huan, J. Li, Ultrathin reduced graphene oxide/MOF nanofiltration membrane with improved purification performance at low pressure, *Chemosphere* 204 (2018) 378–389.
- [29] Y. Liu, W. Tu, M. Chen, L. Ma, B. Yang, Q. Liang, Y. Chen, A mussel-induced method to fabricate reduced graphene oxide/halloysite nanotubes membranes for multi-functional applications in water purification and oil/water separation, *Chem. Eng. J.* 336 (2018) 263–277.
- [30] T. Gao, L. Huang, C. Li, G. Xu, G. Shi, Graphene membranes with tuneable nanochannels by intercalating self-assembled porphyrin molecules for organic solvent nanofiltration, *Carbon* 124 (2017) 263–270.
- [31] L.M. Pastrana-Martinez, S. Morales-Torres, J.L. Figueiredo, J.L. Faria, A.M. Silva, Graphene oxide based ultrafiltration membranes for photocatalytic degradation of organic pollutants in salty water, *Water Res.* 77 (2015) 179–190.
- [32] Y. Gao, M. Hu, B. Mi, Membrane surface modification with  $\text{TiO}_2$ -graphene oxide for enhanced photocatalytic performance, *J. Membr. Sci.* 455 (2014) 349–356.
- [33] G. Liu, K. Han, H. Ye, C. Zhu, Y. Gao, Y. Liu, Y. Zhou, Graphene oxide/triethanolamine modified titanate nanowires as photocatalytic membrane for water treatment, *Chem. Eng. J.* 320 (2017) 74–80.
- [34] G. Rao, Q. Zhang, H. Zhao, J. Chen, Y. Li, Novel titanium dioxide/iron (III) oxide/graphene oxide photocatalytic membrane for enhanced humic acid removal from water, *Chem. Eng. J.* 302 (2016) 633–640.
- [35] L. Chen, N. Li, Z. Wen, L. Zhang, Q. Chen, L. Chen, P. Si, J. Feng, Y. Li, J. Lou, L. Ci, Graphene oxide based membrane intercalated by nanoparticles for high performance nanofiltration application, *Chem. Eng. J.* 347 (2018) 12–18.
- [36] Q. Han, N. Chen, J. Zhang, L. Qu, Graphene/graphitic carbon nitride hybrids for catalysis, *Mater. Horiz.* 4 (2017) 832–850.
- [37] Y. Zhao, J. Zhang, L. Qu, Graphitic carbon nitride/graphene hybrids as new active materials for energy conversion and storage, *ChemNanoMat* 1 (2015) 298–318.
- [38] X. Dong, F. Cheng, Recent development in exfoliated two-dimensional  $\text{g-C}_3\text{N}_4$  nanosheets for photocatalytic applications, *J. Mater. Chem. A* 3 (2015) 23642–23652.
- [39] Y. Li, H. Zhang, P. Liu, D. Wang, Y. Li, H. Zhao, Cross-linked  $\text{g-C}_3\text{N}_4/\text{rGO}$  nanocomposites with tunable band structure and enhanced visible light photocatalytic activity, *Small* 9 (2013) 3336–3344.
- [40] Z. Huang, W. Han, H. Tang, L. Ren, D.S. Chander, X. Qi, H. Zhang, Photoelectrochemical-type sunlight photodetector based on  $\text{MoS}_2$ /graphene heterostructure, *2D Mater.* 2 (2015).
- [41] W. Han, C. Zang, Z. Huang, H. Zhang, L. Ren, X. Qi, J. Zhong, Enhanced photocatalytic activities of three-dimensional graphene-based aerogel embedding  $\text{TiO}_2$  nanoparticles and loading  $\text{MoS}_2$  nanosheets as co-catalyst, *Int. J. Hydrog. Energy* 39 (2014) 19502–19512.
- [42] L. Sun, T. Du, C. Hu, J. Chen, J. Lu, Z. Lu, H. Han, Antibacterial activity of graphene oxide/ $\text{g-C}_3\text{N}_4$  composite through photocatalytic disinfection under visible light, *ACS Sustainable Chem. Eng.* 5 (2017) 8693–8701.
- [43] Z. Tong, D. Yang, J. Shi, Y. Nan, Y. Sun, Z. Jiang, Three-dimensional porous aerogel constructed by  $\text{g-C}_3\text{N}_4$  and graphene oxide nanosheets with excellent visible-light photocatalytic performance, *ACS Appl. Mater. Interface* 7 (2015) 25693–25701.
- [44] H. Zhao, S. Chen, X. Quan, H. Yu, H. Zhao, Integration of microfiltration and visible-light-driven photocatalysis on  $\text{g-C}_3\text{N}_4$  nanosheet/reduced graphene oxide membrane for enhanced water treatment, *Appl. Catal. B-Environ.* 194 (2016) 134–140.
- [45] F. Li, Z. Yu, H. Shi, Q. Yang, Q. Chen, Y. Pan, G. Zeng, L. Yan, A Mussel-inspired method to fabricate reduced graphene oxide/ $\text{g-C}_3\text{N}_4$  composites membranes for catalytic decomposition and oil-in-water emulsion separation, *Chem. Eng. J.* 322 (2017) 33–45.
- [46] Y. Zhu, A. Marianov, H. Xu, C. Lang, Y. Jiang, Bimetallic Ag-Cu supported on graphitic carbon nitride nanotubes for improved visible-light photocatalytic hydrogen production, *ACS Appl. Mater. Interface* 10 (2018) 9468–9477.
- [47] L. Zhang, N. Ding, M. Hashimoto, K. Iwasaki, N. Chikamori, K. Nakata, Y. Xu, J. Shi, H. Wu, Y. Luo, D. Li, A. Fujishima, Q. Meng, Sodium-doped carbon nitride nanotubes for efficient visible light-driven hydrogen production, *Nano Res.* 11 (2018) 2295–2309.
- [48] Q. Gao, S. Hu, Y. Du, Z. Hu, The origin of the enhanced photocatalytic activity of carbon nitride nanotubes: a first-principles study, *J. Mater. Chem. A* 5 (2017) 4827–4834.
- [49] Y. Wang, X. Liu, J. Liu, B. Han, X. Hu, F. Yang, Z. Xu, Y. Li, S. Jia, Z. Li, Y. Zhao, Carbon quantum dot implanted graphitic carbon nitride nanotubes: excellent charge separation and enhanced photocatalytic hydrogen evolution, *Angew. Chem. Int. Ed.* 57 (2018) 5765–5771.
- [50] Z. Mo, H. Xu, Z. Chen, X. She, Y. Song, J. Wu, P. Yan, L. Xu, Y. Lei, S. Yuan, H. Li, Self-assembled synthesis of defect-engineered graphitic carbon nitride nanotubes for efficient conversion of solar energy, *Appl. Catal. B-Environ.* 225 (2018) 154–161.
- [51] H. Lee, S.M. Dellatore, W.M. Miller, P.B. Messersmith, Mussel-inspired surface chemistry for multifunctional coatings, *Science* 318 (2007) 426–430.

- [52] C. Wang, Z. Li, J. Chen, Y. Yin, H. Wu, Structurally stable graphene oxide-based nanofiltration membranes with bioadhesive polydopamine coating, *Appl. Surf. Sci.* 427 (2018) 1092–1098.
- [53] Q. Liu, N. Wang, J. Caro, A. Huang, Bio-inspired polydopamine: a versatile and powerful platform for covalent synthesis of molecular sieve membranes, *J. Am. Chem. Soc.* 135 (2013) 17679–17682.
- [54] S. Martha, A. Nashim, K.M. Parida, Facile synthesis of highly active g-C<sub>3</sub>N<sub>4</sub> for efficient hydrogen production under visible light, *J. Mater. Chem. A* 1 (2013) 7816–7824.
- [55] W.H. Bragg, W.L. Bragg, The reflexion of X-rays by crystals, *Proc. Royal Soc. A* 88 (1913) 428–438.
- [56] Z. Zeng, K. Li, L. Yan, Y. Dai, H. Guo, M. Huo, Y. Guo, Fabrication of carbon nitride nanotubes by a simple water-induced morphological transformation process and their efficient visible-light photocatalytic activity, *RSC Adv.* 4 (2014) 59513–59518.
- [57] S.P. Surwade, S.N. Smirnov, I.V. Vlassiuk, R.R. Unocic, G.M. Veith, S. Dai, S.M. Mahurin, Water desalination using nanoporous single-layer graphene, *Nat. Nanotechnol.* 10 (2015) 459–464.
- [58] M.M. Lucchese, F. Stavale, E.H.M. Ferreira, C. Vilani, M.V.O. Moutinho, R.B. Capaz, C.A. Achete, A. Jorio, Quantifying ion-induced defects and Raman relaxation length in graphene, *Carbon* 48 (2010) 1592–1597.
- [59] D.C. Marcano, D.V. Kosynkin, J.M. Berlin, A. Sinititskii, Z. Sun, A. Slesarev, L.B. Alemany, W. Lu, J.M. Tour, Improved synthesis of graphene oxide, *ACS Nano* 4 (2010) 4806–4814.
- [60] M. Hu, B. Mi, Enabling graphene oxide nanosheets as water separation membranes, *Environ. Sci. Technol.* 47 (2013) 3715–3723.
- [61] X. Chen, M. Qiu, H. Ding, K. Fu, Y. Fan, A reduced graphene oxide nanofiltration membrane intercalated by well-dispersed carbon nanotubes for drinking water purification, *Nanoscale* 8 (2016) 5696–5705.
- [62] Y. Lv, C. Zhang, A. He, S.-J. Yang, G.-P. Wu, S.B. Darling, Z.-K. Xu, Photocatalytic nanofiltration membranes with self-cleaning property for wastewater treatment, *Adv. Funct. Mater.* 27 (2017) 1700251.
- [63] K. Sun, L. Wang, C. Wu, J. Deng, K. Pan, Fabrication of  $\alpha$ -Fe<sub>2</sub>O<sub>3</sub>@rGO/PAN nanofiber composite membrane for photocatalytic degradation of organic dyes, *Adv. Mater. Interface.* 4 (2017) 1700845.
- [64] Y. Wei, C.-H. Jang, Liquid crystal as sensing platforms for determining the effect of graphene oxide-based materials on phospholipid membranes and monitoring anti-bacterial activity, *Sensor. Actuat. B-Chem.* 254 (2018) 72–80.
- [65] J. Tian, Q. Liu, A.M. Asiri, K.A. Alamry, X. Sun, Ultrathin graphitic C<sub>3</sub>N<sub>4</sub> nanosheets/graphene composites: efficient organic electrocatalyst for oxygen evolution reaction, *ChemSusChem* 7 (2014) 2125–2130.

## Supplementary Information

### Photocatalytic Self-Cleaning Carbon Nitride Nanotube Intercalated Reduced Graphene Oxide Membranes for Enhanced Water Purification

Yibin Wei<sup>a\*</sup>, Yuxiang Zhu<sup>b</sup>, Yijiao Jiang<sup>b,\*</sup>

a. Department of Environmental Sciences, Macquarie University, Sydney, NSW 2109, Australia

b. School of Engineering, Macquarie University, Sydney, NSW 2109, Australia

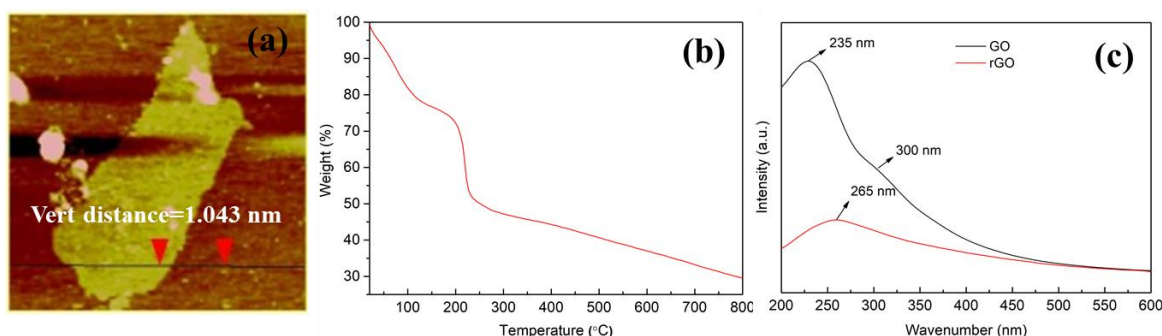
#### Corresponding authors:

*\*Tel:* +61-2-9850-8337; *E-mail:* [yibin.wei@hdr.mq.edu.au](mailto:yibin.wei@hdr.mq.edu.au) (Y. Wei); *E-mail:* [yijiao.jiang@mq.edu.au](mailto:yijiao.jiang@mq.edu.au) (Y. Jiang)

## 1. Synthesis and characterization of GO and rGO

Graphene oxide (GO) was prepared using a modified method according to the literature [1]. A mixture of  $\text{NaNO}_3$  (5 g) and graphite powder (10 g) was added to 230 mL of concentrated  $\text{H}_2\text{SO}_4$  and stirred for 3 h. Next, 30 g  $\text{KMnO}_4$  was slowly put into the suspension, and the solution temperature kept below 20 °C. Then, the suspension was carefully heated to 35 °C and stirred for 2 h. 460 mL of deionized water was then added, the mixture was heated to 98 °C and stirred for another 30 min. The reaction was completed by the addition of 1.4 L of deionized water, followed by the introduction of 30 wt%  $\text{H}_2\text{O}_2$  (25 mL) until the mixture became bright yellow. After washing with HCl and a large amount of water, the GO powder was obtained via vacuum freeze drying. The concentration of GO solution was determined through re-dispersion. Reduced GO (rGO) solution was obtained through a facile longwave ultraviolet light (365 nm) irradiation for 48 h.

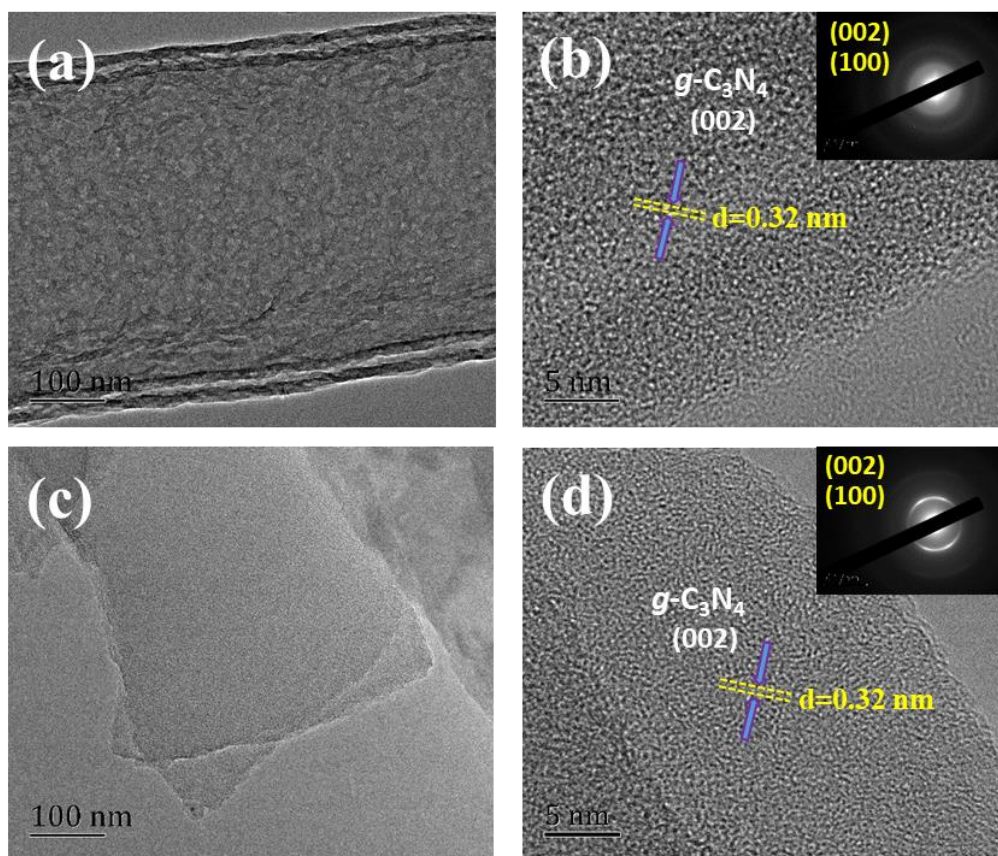
Morphology of the GO nanosheets was characterized by atomic force microscopy (AFM, NanoScope, Veeco Metrology). Samples were tested under ambient conditions using silicon tips with an average radius of ~10 nm and the  $2 \times 2 \mu\text{m}$  images were captured at a scan rate of 1.0 Hz with 256 sample points per line and the oscillation amplitude was 10 nm. The thermal properties of GO and as-prepared membranes were characterized by thermogravimetric analysis (TG analysis, NETZSCH STA 449F3) in the range of room temperature to 800 °C with the rate of  $10^\circ\text{C min}^{-1}$ .



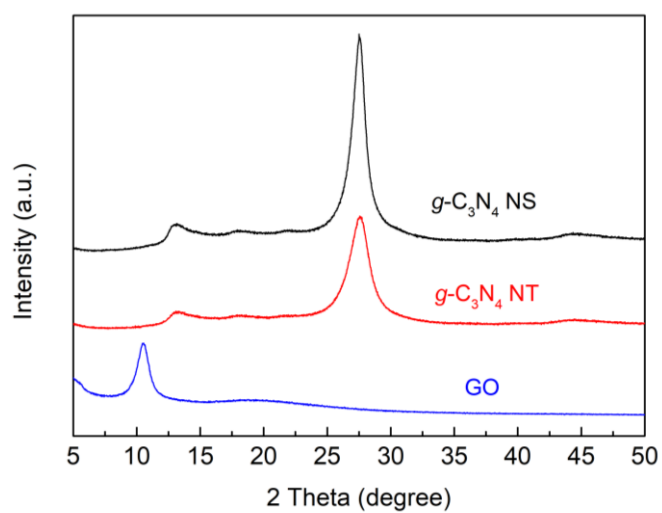
**Fig. S1.** (a) AFM; (b) TG analysis of GO; (c) UV-Vis spectra of GO and rGO

## 2. Characterization of *g*-C<sub>3</sub>N<sub>4</sub> NT and *g*-C<sub>3</sub>N<sub>4</sub> NS

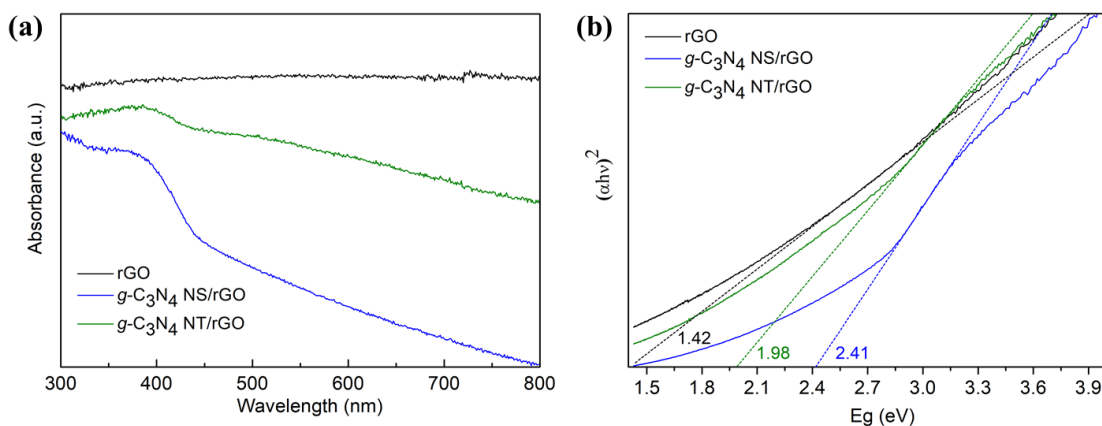




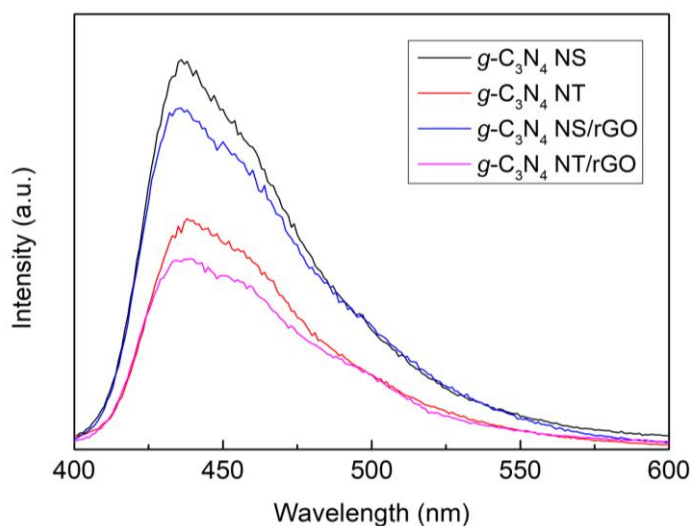
**Fig. S2.** HRTEM images of (a)-(b) g-C<sub>3</sub>N<sub>4</sub> NT and (c)-(d) g-C<sub>3</sub>N<sub>4</sub> NS. The insets in (b) and (d) are the accompanying SAED patterns.



**Fig. S3.** XRD patterns of the GO, g-C<sub>3</sub>N<sub>4</sub> NS and g-C<sub>3</sub>N<sub>4</sub> NT.



**Fig. S4.** UV-vis diffuse reflectance spectra of the rGO,  $g\text{-C}_3\text{N}_4$  NS/ rGO and  $g\text{-C}_3\text{N}_4$  NT /rGO composites.



**Fig. S5.** PL spectra of the rGO,  $g\text{-C}_3\text{N}_4$  NS,  $g\text{-C}_3\text{N}_4$  NT,  $g\text{-C}_3\text{N}_4$  NS/ rGO and  $g\text{-C}_3\text{N}_4$  NT /rGO composites.

According to our previous work [2], the band gaps of  $g\text{-C}_3\text{N}_4$  NS and  $g\text{-C}_3\text{N}_4$  NT were determined to be 2.77 eV and 2.75 eV, respectively. The UV-Vis diffuse reflectance spectra of rGO,  $g\text{-C}_3\text{N}_4$  NS/rGO and  $g\text{-C}_3\text{N}_4$  NT/rGO are shown in Fig. S4a and the band gaps of the materials were calculated by using the Kubelka-Munk transformation (Fig. S4b). The rGO exhibits strong light absorbance in UV and visible light region and the band gap of rGO was determined to be 1.42 eV. After intercalating with  $g\text{-C}_3\text{N}_4$  NT and  $g\text{-C}_3\text{N}_4$  NS, the band gaps of  $g\text{-C}_3\text{N}_4$  NS/rGO and  $g\text{-C}_3\text{N}_4$  NT/rGO decrease to approximately 2.41 eV and 1.98



eV, respectively. The results suggest that the as-prepared  $g\text{-C}_3\text{N}_4/\text{rGO}$  composites shows a combined behaviour in optical property. PL spectroscopy was used to investigate the carrier separation efficiency of the as-prepared photocatalysts. In general, a lower PL emission intensity corresponds to a lower carrier recombination rate, i.e. a longer lifetime of the electron-hole pairs [2]. In Fig. S5, the  $g\text{-C}_3\text{N}_4$  NS exhibit a strong emission band at around 450 nm, and the intensity is higher than that of  $g\text{-C}_3\text{N}_4$  NT, indicating the efficient transportation of the photo-excited carriers at  $\text{C}_3\text{N}_4$  NT surface. The PL intensities become lower after incorporation with rGO nanoparticles, which may be ascribed to the fact rGO acting as an electron collector leads to a decreased recombination of photo-generated electrons and holes in the composites. Additionally, it is apparent that the  $g\text{-C}_3\text{N}_4$  NT/rGO exhibits the lowest intensity of the PL signal, which demonstrates the prolonged lifetime of the carriers, thus enhancing the photocatalytic performance.

**Table S1.** XPS analysis of  $g\text{-C}_3\text{N}_4$  NS/rGO and  $g\text{-C}_3\text{N}_4$  NT/rGO

Name	rGO	$g\text{-C}_3\text{N}_4$ NS/rGO	$g\text{-C}_3\text{N}_4$ NT/rGO
	[Peak (BE)/Atomic (%)]	[Peak (BE)/Atomic (%)]	[Peak (BE)/Atomic (%)]
C1s	284.38-297.95/77.16	284.38-297.95/78.82	284.38-297.95/79.81
O1s	532.17-544.95/22.84	532.17-544.95/17.96	532.17-544.95/18.35
N1s	0	398.77-409.95/3.21	398.77-409.95/1.84

Abbreviation: BE, binding energy (eV)

### Supporting References

- [1] W.S. Hummers, R.E. Offeman, Preparation of graphitic oxide, J. Am. Chem. Soc. 80 (1958) 1339-1339.
- [2] Y. Zhu, A. Marianov, H. Xu, C. Lang, Y. Jiang, Bimetallic Ag-Cu supported on graphitic carbon nitride nanotubes for improved visible-light photocatalytic hydrogen production, ACS Appl. Mater. Interface 10 (2018) 9468-9477.

# Chapter 4 Precise Tuning Chemistry and Tailoring Defects of Graphene Oxide Films by Low Energy Ion Beam Irradiation

This chapter consists of:

- Overview
- Motivations and contributions
- Story behind the article
- The article-

Abstract

1. Introduction

2. Materials and methods

2.1. Materials

2.2. Ion beam irradiation

2.3. Characterization

2.4. Simulation

3. Results and discussion

3.1. Surface morphological analysis

3.2. Chemical state analysis

3.3. Defect analysis

3.4. SRIM simulations

4. Conclusions

Reference

## 4.1 Overview

The research article forming this chapter has been submitted for publication. Crumpled laminar nanostructures forming membrane separation layer constructed by two-dimensional (2D) graphene oxide (GO) has been considered promising for water treatment. However, precise tuning of the structure remains challenging to reach the state-of-the-art separation performance that is predicted by theoretical studies. Ion beam irradiation technology offers a wide choice of ion beams in terms of ion species and ion energies to achieve on-demand modification, which has been applied to 2D nanomaterials modification very recently (Note:

detailed research background will be discussed and referenced in the main article). Therefore, in this study, we first explore the possibility of in-situ modification of GO films to achieve a desired GO-based nanostructure using an ion beam. I found that the low energy carbon ion beam irradiation could simultaneously reduce and drill nanoscale pores on ultra-thin GO films in a controllable manner. This work provides in-depth understanding of tuning chemistry and tailoring defects on GO-based laminar nanostructures by ion beam-induced surface engineering, opening new possibilities for fabricating nanoporous GO for a wide of potential applications such as water treatment and gas separation.

## **4.2 Motivations and contributions**

As mentioned above, efficient and precise tuning of the laminar structure of 2D nanomaterial-based membranes is the key to preparation of high-performance membranes with excellent permeability and selectivity. The Australian Nuclear Science and Technology Organization (ANSTO) could provide technology supporting a broad range of disciplines, emphasising nuclear technology. I expected that a beam of accelerated ions could be used for GO membrane irradiation in order to modify its structure by creation of point and extended defects. These defects should increase the porosity of the as-prepared membranes. Based on the wide choice of ions having different combinations of mass, energy, and charge state offered by the ANSTO accelerator, the pore creation efficiency can be tuned in a controllable manner. This proposed idea attracted the interest from Dr Zeljko Pastuovic at ANSTO as well. With the support from the National Collaborative Research Infrastructure Strategy (NCRIS) funding provided by the Australian Government (Project No.: ARP-11226), the ground-breaking work was conducted together with researchers from Macquarie University and ANSTO.

The work was led by Yibin Wei and Dr Zeljko Pastuovic. Dr Timothy Murphy, an expert in Raman analysis, at the Department of Earth and Planetary Sciences, Macquarie University, was invited to be included in this project contributing the defect analysis from Raman spectroscopy. Y. Wei had the idea of exploring the effect of ion beam on ultra-thin GO films. Y. Wei and Z. Pastuovic designed and conducted the experiments. Y. Wei drafted the article and all authors contributed to data analyse, discussions and manuscript preparation. D. B. Gore supervised the whole project, participated in some experiments and critically revised the manuscript.

### 4.3 Story behind the article

It is never easy to make a research paper. This research project is completely new and there were very few references. So, we met many problems and had to overcome them in this project. For choosing a suitable GO target, substrate-supported GO film and free-standing GO film were both tested. As shown in the below photograph, in our first ion beam irradiation experiment, the free-standing GO membrane with thickness about 100 nm was burned after ion beam irradiation. Moreover, the way of mounting GO samples on the stage was also not idea because the samples might be influenced by the heat generated by the ion beams.

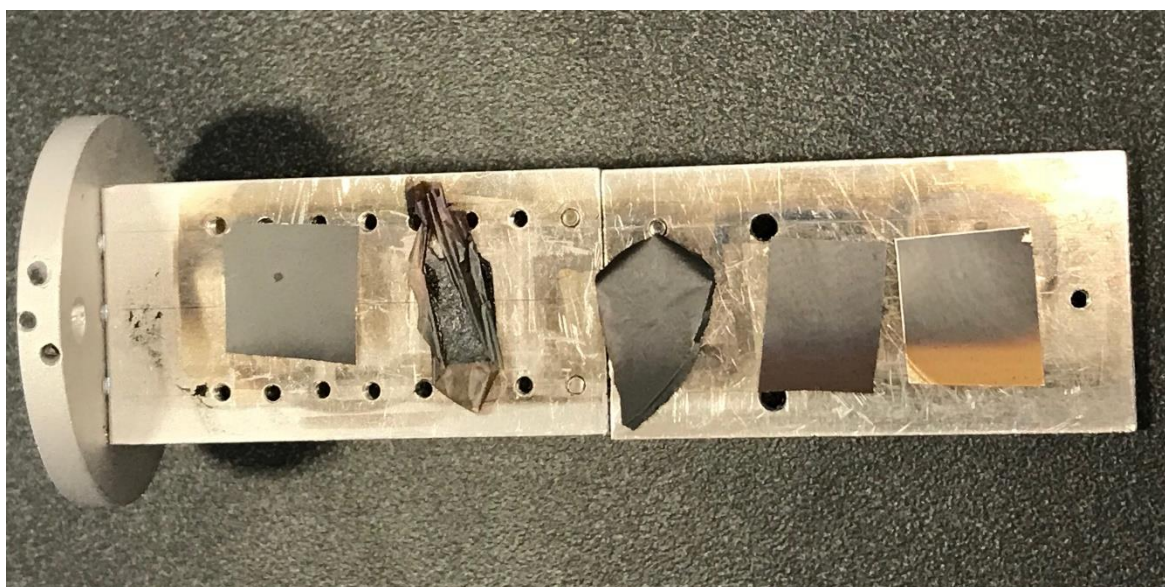


Figure 4.1. Photograph of the results obtained from our first ion beam irradiation experiment: GO membranes mounted on stage after ion beam irradiation.

Besides, it was also unknown how to select the ion type, ion energy and ion fluence. Zeljko is an experienced ion beam implanter expert, who suggested to use the easily available carbon ion with the ion influence between  $1 \times 10^{15}$  ions·cm<sup>-2</sup> to  $1 \times 10^{17}$  ions·cm<sup>-2</sup>. Fortunately, characterization which followed confirms that his intuition was correct. We found an interesting threshold ion fluence of  $1 \times 10^{16}$  ions·cm<sup>-2</sup> which has a significant influence on the chemistry and structure of the ion beam irradiated GO film.

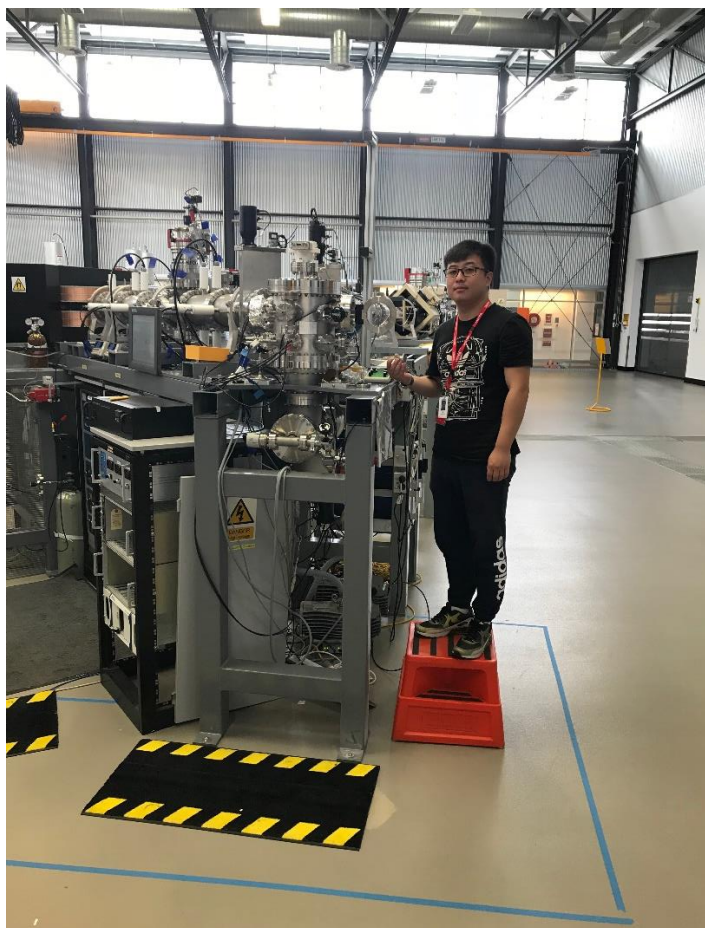


Figure 4.2. Photograph of Yibin and the low energy ion beam material modification unit in ANSTO (photo: Damian Gore).

#### **4.4 The article-**

### **Precise tuning chemistry and tailoring defects of graphene oxide films by low energy ion beam irradiation**

Yibin Wei <sup>a\*</sup>, Zeljko Pastuovic <sup>b</sup>, Timothy Murphy <sup>c</sup>, Damian B. Gore <sup>a</sup>

a. Department of Environmental Sciences, Macquarie University, Sydney, NSW 2109, Australia

b. Centre for Accelerator Science, Australian Nuclear Science and Technology Organization, Sydney, NSW 2234, Australia

c. Department of Earth and Planetary Sciences, Macquarie University, Sydney, NSW 2109, Australia

To whom all correspondence should be addressed.

*\*Tel: +61-2-9850-8337; E-mail: yibin.wei@hdr.mq.edu.au (Y. Wei)*

## **Abstract**

Precise tuning chemistry and tailoring nanopores of graphene oxide (GO) thin films are vital for their application in liquid and gas separation. In this work, ultra-thin GO films with thickness of about 150 nm were prepared and then modified by a low energy carbon ion beam with ion fluences ranging from  $1 \times 10^{15}$  ions·cm<sup>-2</sup> to  $1 \times 10^{17}$  ions·cm<sup>-2</sup>. An ion fluence of  $1 \times 10^{16}$  ions·cm<sup>-2</sup> is a threshold of surface geometry (i.e. the chemical state and the consequent morphology) for the GO film. Moreover, X-ray photoelectron spectroscopy (XPS) results reveal that oxygen loss in ion beam-induced reduction of GO films was mainly by the elimination of the unstable C=O species. Raman spectroscopy indicates a mass of defects with a mean defect distance of about 1.4 nm were generated in GO films by C<sup>+</sup> irradiation. According to SRIM simulation, an average of 208 carbon vacancies were created in GO film per impinging C<sup>+</sup>. These results suggest that low energy carbon ion beam irradiation is promising for simultaneously reducing and drilling nanoscale pores on GO surfaces in a controllable manner, which could be used for engineering GO-based separation membranes.

**Keywords:** Graphene oxide; ultrathin film; ion beam; defect; Raman; SRIM

## 1. Introduction

Graphene, consisting of a one-atom-thick planar sheet of  $sp^2$ -bonded carbon atoms, has attracted much scientific and industrial interest in the past decade owing to its unique thermal, electronic, and mechanical properties.<sup>1-6</sup> In addition to applications in the production of transistors,<sup>7</sup> supercapacitors<sup>8</sup> and sensors,<sup>9</sup> porous graphene has been considered a promising nanoscale building block for construction of liquid or gas separation membranes, because the robust one-atom-thick carbon layer may minimize transport resistance and maximize permeate flux in the separation process.<sup>10</sup> Although many theoretical studies<sup>11-14</sup> have predicted extraordinary molecular separation performance of porous graphene and a few experimental attempts<sup>15-16</sup> drilling holes in graphene surface have confirmed the potential of porous graphene in selective passage of salt ions and gas molecules, there still remain challenges in fabricating large-scale membranes with low cost for practical applications.

Graphene oxide (GO) is the oxidized derivative of graphene, which could be cost-effectively produced through a solution-based approach by direct oxidization and exfoliation from graphite.<sup>17</sup> GO could be regarded as a graphene scaffold with different oxygen-containing functional groups including epoxy, carboxyl, hydroxyl, and carbonyl. The oxidation of GO provides abundant reaction sites for chemical modification while resulting in considerable amounts of defects on the basal plane.<sup>18</sup> In recent years, there are an exponentially growing number of studies on GO-based membranes, because GO nanosheets could be assembled into laminar structures via simple vacuum filtration or coating methods providing fast and selective channels for small molecules transportation.<sup>19</sup> Most of these works focused on tuning GO-based laminar structures to obtain excellent structural stability and membrane separation performance (i.e. permeability and selectivity).<sup>20-23</sup> To optimize the laminar structure, the majority of reported strategies could be summarized as a two-step procedure;



reduction of GO and increasing the laminar interlayer space.<sup>24</sup> This is because chemical reduction can stabilize the GO laminar structure but lead to significant permeability decline, and the incorporation of nanoscale fillers could enlarge interlayer spacing introducing more channels, compensating for the lowered permeability.<sup>25</sup> However, it seems that these conventional chemical modification methods involve multiple steps that are not simple to be precisely controlled.

Physical processing techniques including plasma treatment,<sup>26</sup> laser treatment,<sup>27</sup> electron beam irradiation<sup>28</sup> and ion beam irradiation<sup>29</sup> have been successfully used to engineer graphene-based materials in the past few years. Among these techniques, ion beam irradiation offers a wide choice of ion species and energies to achieve customizable modification. Very recently, several experiments have demonstrated that two-dimensional (2D) graphene or GO could be efficiently modified by diverse ion beams<sup>30-37</sup> and the irradiation of 2D materials may trigger three main effects including structural modification, defect engineering, and doping effects.<sup>38</sup> For example, O'Hern et al.<sup>15</sup> introduced sub-nanometer defects onto single layer graphene by an ion beam in a controllable manner, which demonstrates great potential for the development of nanoporous separation membranes. However, Malinsky et al.<sup>39</sup> found that there were no compositional changes in bulk GO film with thickness  $\sim 50\ \mu\text{m}$  associated with ion beam irradiation. In addition, using 250 keV chlorine ions at fluence of  $5 \times 10^{13}\ \text{ions}\cdot\text{cm}^{-2}$ , Ammar et al.<sup>40</sup> believed that their ion beam could only penetrate through approximately 200 nm of a graphite surface due to dissipation of the irradiating ion energy. These results suggest ion beam could create sub-nanometer pores on graphene, but the penetration depth of ions was limited to a certain thickness.

Generally, ion beam irradiation induced surface engineering can introduce energetic ions which alter the surface chemistry as well as create additional defects or vacancies in the

target. Therefore, it is possible to fabricate nanoporous thin GO films for separation purposes, but the thickness of the GO layer and ion beam conditions need to be better constrained. To the best of our knowledge, there is still no report on ion beam irradiated thin GO film with thickness of a few hundreds of nanometers. In this work, we explore the potential for preparation of “nanoporous GO membranes” by *in-situ* ion beams for simultaneous tuning of chemistry and tailoring nanopores on a GO film. We first investigate the morphological, chemical and structural properties of ultrathin GO films (~150 nm) irradiated with low energy C<sup>+</sup> with different fluences. The defects created by ion beam irradiation were then investigated using Raman spectroscopy and theoretically simulated by SRIM. This work provides an in-depth understanding of tuning chemistry and tailoring defects on graphene oxide films by ion beam-induced surface engineering process, opening new possibilities for fabricating nanoporous GO for a wide range of potential applications such as water treatment and gas separation.

## **2. Materials and Methods**

### *2.1. Materials*

Graphene oxide (GO) water dispersion (4 mg·mL<sup>-1</sup>) was purchased from Graphenea Corporation. Ethylenediamine (≥ 99.8 %) was purchased from Sigma Aldrich. Commercial cellulose nitrate (CN) filters (diameter: 47 mm; pore size: 0.45 μm; thickness 0.5 mm; mass density: 1.6 g·cm<sup>-3</sup>) were obtained from Sartorius. All chemicals were used as received. Deionized (DI) water (18.2 MΩ·cm<sup>-1</sup> at 25 °C) used throughout this study was generated by a Milli-Q system.

### *2.2. Ion beam irradiation*

Disc-type CN filters were used as a support and GO water dispersion ( $0.0025 \text{ mg}\cdot\text{mL}^{-1}$ ) with was used as GO film casting solution. Ethylenediamine was used as cross-linker to enhance the stability of the GO stacking structure.<sup>41</sup> 200 mL GO water dispersion with 1 wt% ethylenediamine was vacuum filtrated through the CN filters at room temperature to form the GO films.

The low energy ion implanter at the Australian Nuclear Science and Technology Organization (ANSTO)<sup>42</sup> was used for 40 keV  $\text{C}^+$  ion beam irradiation of the as-prepared GO films. All irradiation was performed using a raster-scanning focused beam through a mask of  $20 \text{ mm} \times 20 \text{ mm}$ . The ion fluence delivered to the target was calculated using the total integrated ion beam current induced in the target. The ion beam current was varied in the  $1\text{-}5 \text{ }\mu\text{A}$  current range in order to achieve homogenous irradiation of the total scanned area of samples during irradiation periods of 1 to 60 min. The total accumulated ion doses delivered to samples were in the range of  $1 \times 10^{15} - 1 \times 10^{17} \text{ ions}\cdot\text{cm}^{-2}$ .

### *2.3. Characterization*

A field emission scanning electron microscope (FESEM, JSM-7100F, JEOL) was used to image surface and cross-section morphologies of the as-prepared GO films at an acceleration voltage of 15 kV. The three dimensional (3D) vision of the GO film surface and its roughness was established and analyzed by atomic force microscopy (AFM, Innova, Bruker). Samples were tested under ambient conditions in tapping mode and  $5 \times 5 \text{ }\mu\text{m}$  images were captured at a scan rate of  $10 \text{ }\mu\text{m}\cdot\text{s}^{-1}$  with 1024 sample points per line. The crystalline structure was analyzed by X-ray diffractometry (XRD, Aeris, PANalytical) using  $\text{Cu K}\alpha$  radiation at 40 kV and 15 mA. Attenuated total reflection Fourier transform infrared spectroscopy (ATR-FTIR, Nicolet 6700, Thermo Fisher) was used to study the chemical functional groups of the film samples. Raman spectra were recorded on LabRAM (HORIBA) with 512 nm

wavelength laser light at power of 50%. Raman mapping was performed at 2  $\mu\text{m}$  steps for an area 50  $\mu\text{m} \times 50 \mu\text{m}$  with an acquisition time of 2 s and duplicate measurement of each point, and the maps were processed in LabSpec 6. An X-ray photoelectron spectrometer (XPS, ESCALAB 250Xi, Thermo Fisher) equipped with a monochromated Al K $\alpha$  source (1486.68 eV) operating at 150 W was used for quantitative elemental analyse. A pass energy of 100 eV was applied to wide scans and 20 eV was used for high resolution scans. Scans were repeated 20 times and the spot size was 500  $\mu\text{m}$ . The binding energies were calibrated with reference to C1s at 284.8 eV for adventitious hydrocarbon contamination.

#### *2.4. Simulation*

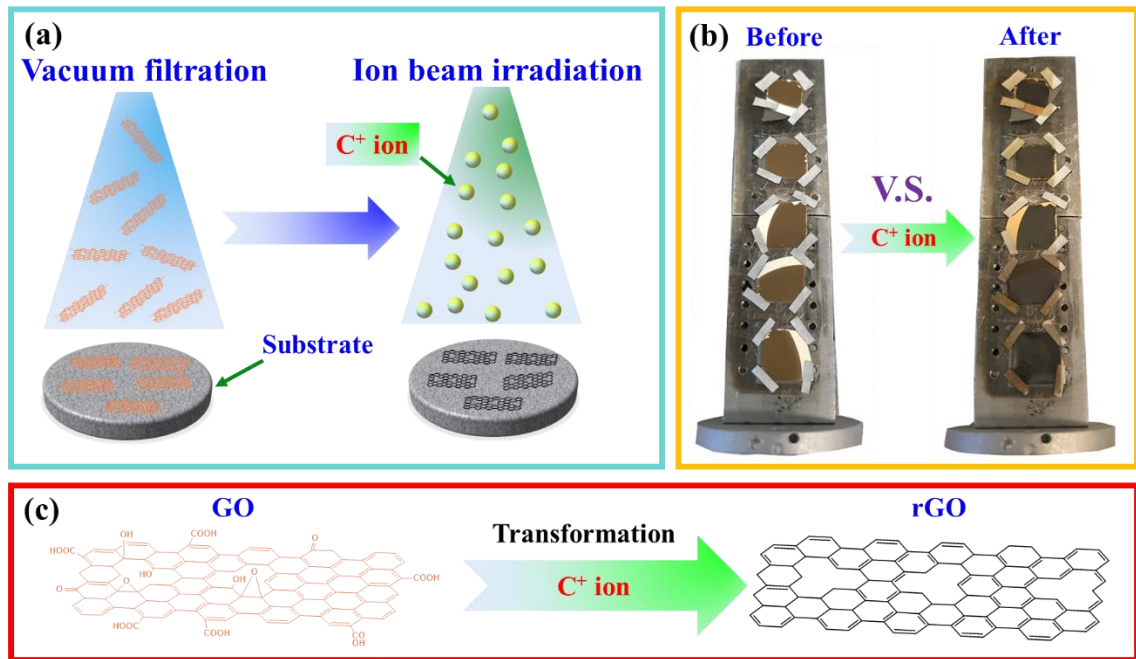
Irradiation of the GO film deposited on a thick filter is simulated using the SRIM code.<sup>43</sup> The mass density of GO film is approximated with the density of a graphite sheet (2.253 g·cm<sup>-3</sup>). The energy required for a displacement of a carbon atom from its site and creation of a carbon vacancy in graphene is ~24 eV.<sup>44</sup> The simulation was run for a total of 50000 carbon ion projectiles incident perpendicular to the sample surface.

### **3. Results and Discussion**

#### *3.1. Surface morphological analysis*

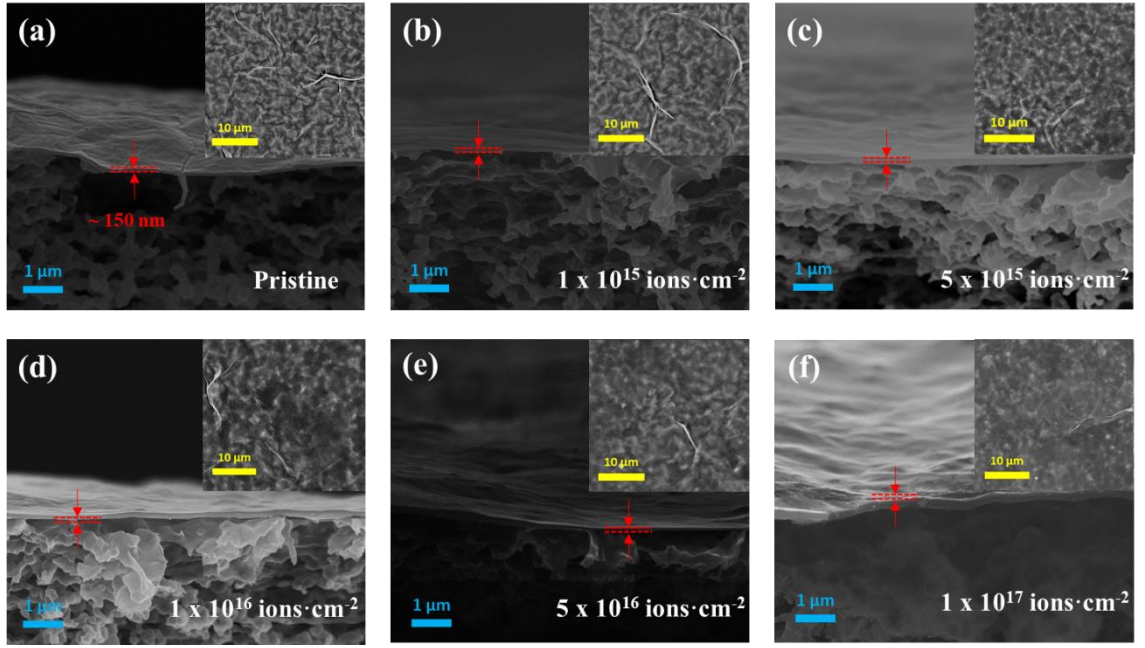
The preparation and ion beam irradiation process of the GO films is summarized and illustrated in Fig.1. GO films before ion beam irradiation exhibited a yellowish brown colour and those films became black after irradiation (Fig. 1b). This may indicate that the chemical state of GO films was modified by the C<sup>+</sup> ions. Fig. 2 shows the cross-sectional and surface morphologies of the pristine and the ion beam irradiated GO films analyzed by SEM. Taking the visual error from the cross-sectional images into consideration, the thickness of the as-prepared pristine GO film was estimated to be ~150 nm. Ion beam irradiated GO films show

the same thickness as the pristine GO film, indicating ion beam irradiation with these operating conditions did not change the ultrathin and layered GO structures. The pristine GO film did not show any visible surface morphological defects and a typical GO surface with wrinkled structure was observed. Surface morphologies of GO films irradiated with  $1 \times 10^{15}$  ions·cm<sup>-2</sup> and  $5 \times 10^{15}$  ions·cm<sup>-2</sup> were similar to that of the pristine GO film, whereas increasing numbers of “silk veil waves” on the GO film surfaces were removed after ion beam irradiation at ion fluences greater than  $1 \times 10^{16}$  ions·cm<sup>-2</sup>. Compared with the surface morphology of pristine GO film, the GO film irradiated at the highest ion fluence ( $1 \times 10^{17}$  ions·cm<sup>-2</sup>) in our study exhibited a nearly new appearance with very few wrinkles. Our findings are similar to those reported by Jayalakshmi et al.<sup>45</sup>, who believed many more oxygen-containing functional groups distributed at the edge and basal plane of GO layers could be removed by ion beam irradiation at higher ion fluence.

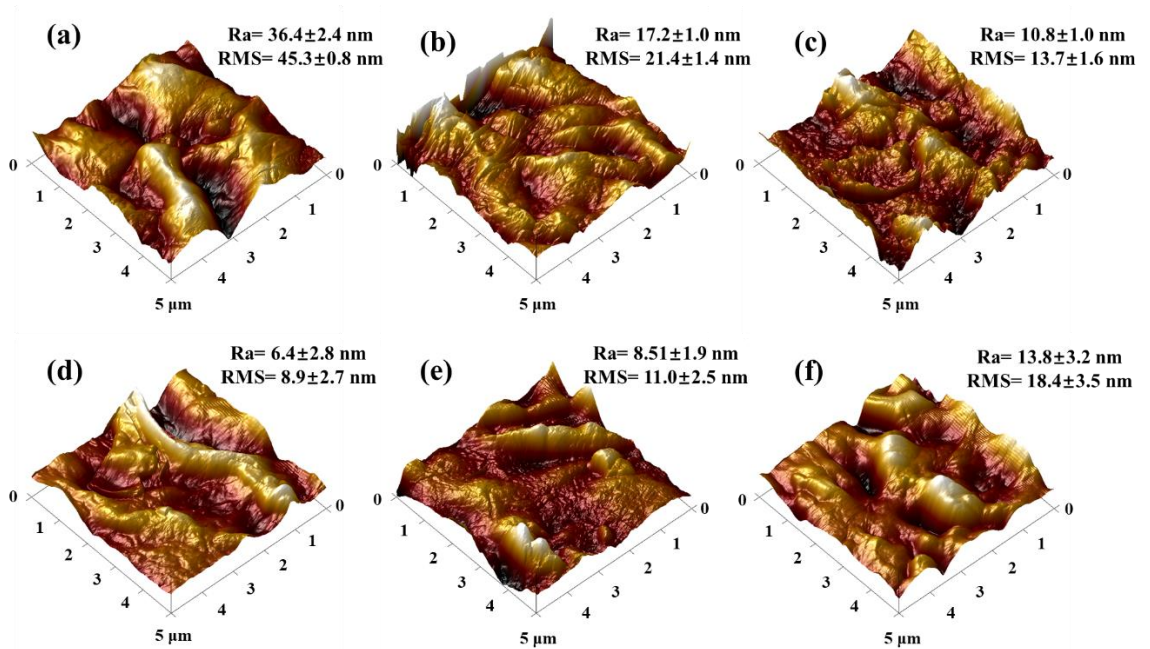


**Fig. 1.** (a) Schematic illustration for preparation and ion beam irradiation of GO films; (b) photographs of GO films mounted on the stage before and after irradiation; (c) illustration of the chemical and structural transformation of GO after irradiation.

To further characterize the surface morphologies of these GO films, AFM measurements were conducted. Sand dune-like surface structures with valleys and gullies were observed on pristine and ion beam-irradiated GO films (Fig. 3). The arithmetical roughness (Ra) and root mean squared roughness (RMS) of the pristine GO film were  $36.4 \pm 2.4$  nm and  $45.3 \pm 0.8$  nm, respectively (Fig. 3a). All ion beam irradiated GO films showed significant decreases in surface roughness (Fig. 3b-f), and the roughness of ion beam irradiated GO films was controlled by the ion fluence. It seems that  $1 \times 10^{16}$  ions·cm<sup>-2</sup> is the ion fluence threshold in terms of the surface roughness of these ion beam irradiated GO films (Fig. 3d), because the GO film irradiated at  $1 \times 10^{16}$  ions·cm<sup>-2</sup> has the lowest Ra and RMS values ( $6.4 \pm 2.8$  nm and  $8. \pm 2.7$  nm, respectively). We speculate that more surface irregularities were eliminated by ion beams with fluence below the threshold, while the GO surface morphologies were reshaped by ion beams with larger ion fluences. The AFM analysis is consistent with the above-mentioned SEM results.



**Fig. 2.** Cross-sectional SEM images of (a) pristine GO film and GO films irradiated by 40 keV  $C^+$  at fluences of: (b)  $1 \times 10^{15} \text{ ions}\cdot\text{cm}^{-2}$ , (c)  $5 \times 10^{15} \text{ ions}\cdot\text{cm}^{-2}$ , (d)  $1 \times 10^{16} \text{ ions}\cdot\text{cm}^{-2}$ , (e)  $5 \times 10^{16} \text{ ions}\cdot\text{cm}^{-2}$  and (f)  $1 \times 10^{17} \text{ ions}\cdot\text{cm}^{-2}$ . Inserts: SEM images of the surface morphologies of these films.

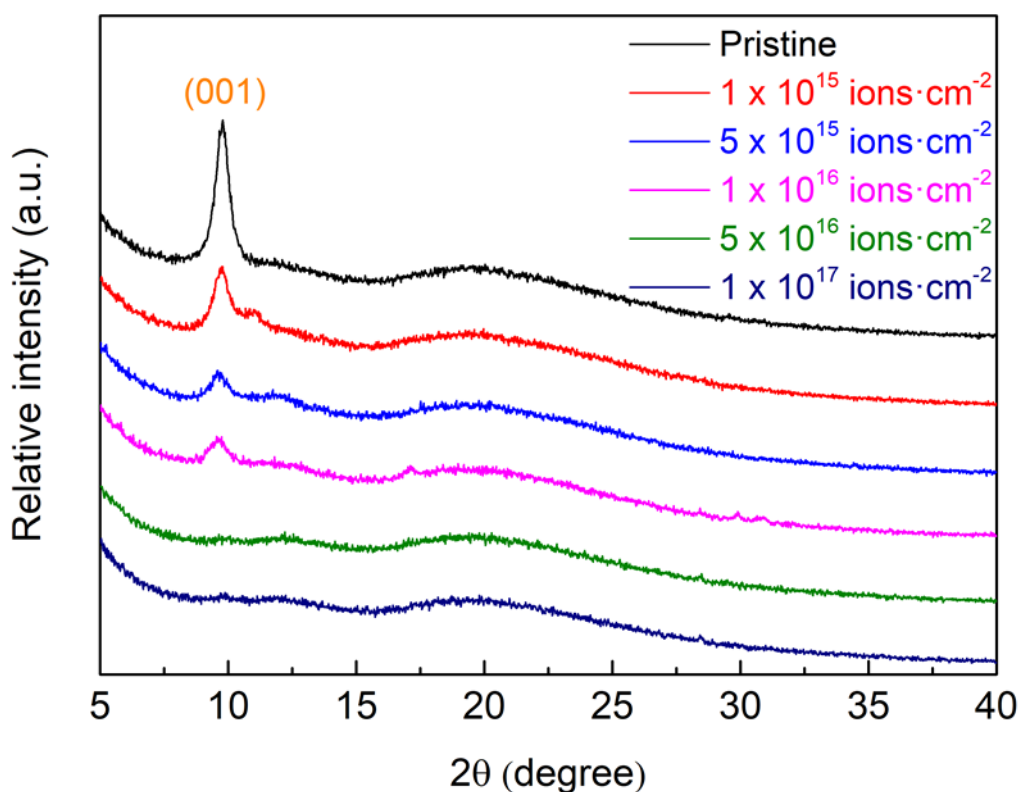


**Fig. 3.** AFM images of (a) pristine GO film and GO films irradiated by 40 keV  $C^+$  at fluences of: (b)  $1 \times 10^{15} \text{ ions}\cdot\text{cm}^{-2}$ , (c)  $5 \times 10^{15} \text{ ions}\cdot\text{cm}^{-2}$ , (d)  $1 \times 10^{16} \text{ ions}\cdot\text{cm}^{-2}$ , (e)  $5 \times 10^{16} \text{ ions}\cdot\text{cm}^{-2}$  and (f)  $1 \times 10^{17} \text{ ions}\cdot\text{cm}^{-2}$  with calculated roughness values.

### 3.2. Chemical state analysis

Crystal structures of pristine and ion beam irradiated GO films were examined by recording the XRD patterns (Fig. 4). The XRD pattern of pristine GO film showed a strong peak centered at  $\sim 9.8^\circ$   $2\theta$  corresponding to the characteristic peak (001) of GO.<sup>46</sup> With the increase of the ion fluence, the relative intensity of full GO characteristic peaks became weaker. The languishing GO characteristic peak reveals the increasing degree of deoxygenation or reduction of the GO, consistent with previous studies.<sup>47-48</sup> Notably, the ion fluence of  $1 \times 10^{16}$  ions $\cdot$ cm $^{-2}$  is also the threshold regarding the existence of full GO characteristic peak since the peak disappeared when irradiated at an ion fluence above this threshold. This result might also explain the threshold phenomenon from the above-mentioned morphological analysis.

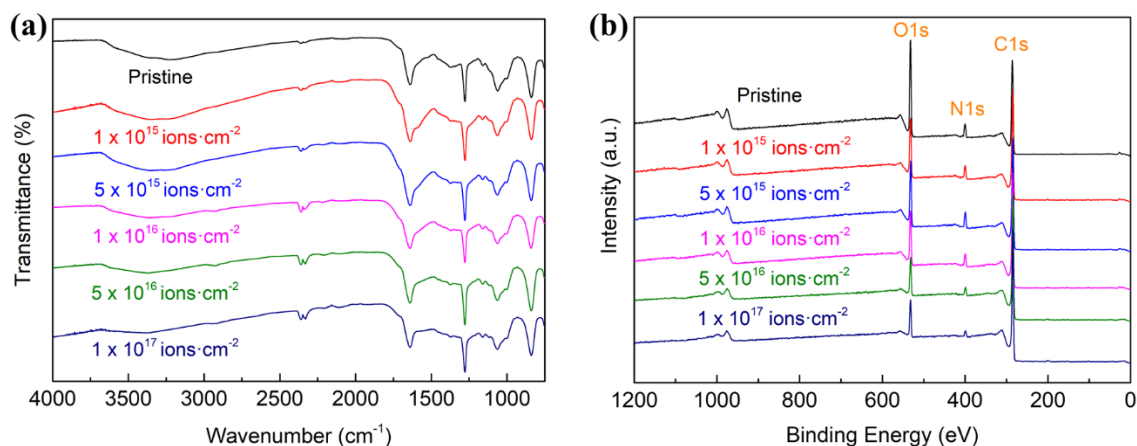




**Fig. 4.** XRD patterns of pristine GO film and GO films irradiated by 40 keV  $C^+$  at fluences of:  $1 \times 10^{15} \text{ ions}\cdot\text{cm}^{-2}$ ,  $5 \times 10^{15} \text{ ions}\cdot\text{cm}^{-2}$ ,  $1 \times 10^{16} \text{ ions}\cdot\text{cm}^{-2}$ ,  $5 \times 10^{16} \text{ ions}\cdot\text{cm}^{-2}$  and  $1 \times 10^{17} \text{ ions}\cdot\text{cm}^{-2}$ .

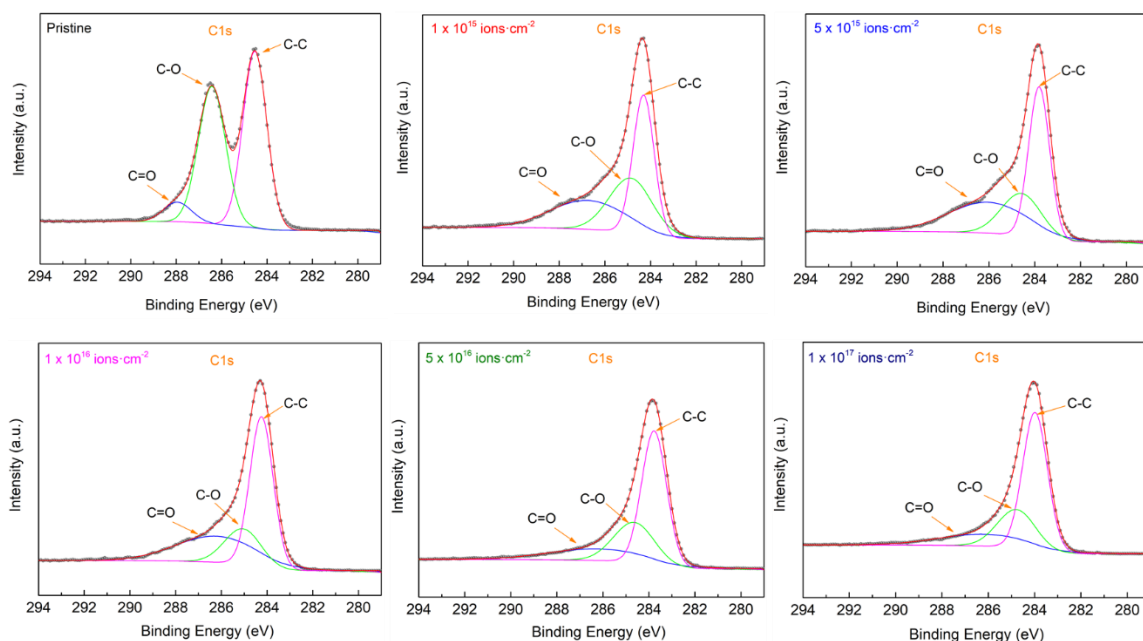
The functional groups of the as-prepared GO films were studied by FTIR (Fig. 5a). The pristine and ion beam irradiated GO films show identical FTIR spectra. Typical GO peaks at  $1037 \text{ cm}^{-1}$ ,  $1223 \text{ cm}^{-1}$ ,  $1619 \text{ cm}^{-1}$ ,  $1738 \text{ cm}^{-1}$  and  $1630 \text{ cm}^{-1}$  representing C-O, C-OH, C=C, C-O, and O-H bonds, were recorded. The peak centered at around  $625 \text{ cm}^{-1}$  corresponds to C-C stretching vibration by ethylenediamine.<sup>25</sup> This suggests that ion beam irradiation could not completely eliminate the existing functional groups on the GO surface. In addition, wide-scan XPS spectra confirmed that carbon, oxygen and nitrogen were retained after  $C^+$  ion beam irradiation (Fig. 5b). The relative intensity of the O1s peak is a little higher than that of the C1s peak in pristine GO film, while the opposite result that C1s peaks were much higher than O1s, was found for all ion beam irradiated GO films. This

indicates the carbon component is predominant after ion beam irradiation despite oxygen-containing groups being retained.



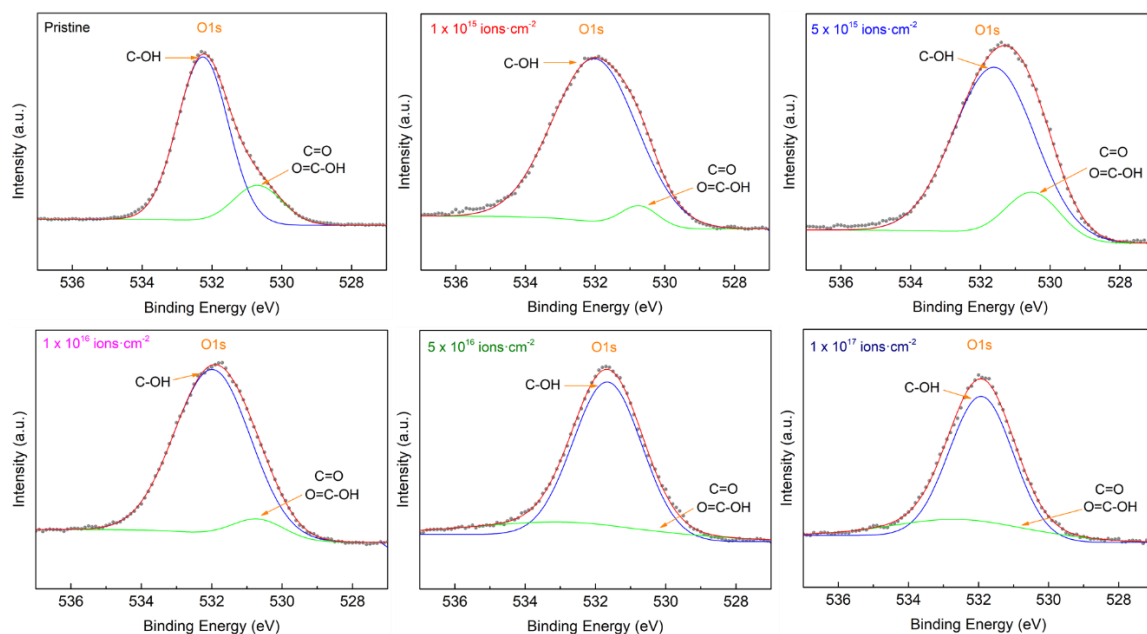
**Fig. 5.** (a) FTIR spectra and (b) wide-scan XPS spectra of pristine GO film and GO films irradiated by 40 keV C<sup>+</sup> at fluences of: 1 × 10<sup>15</sup> ions·cm<sup>-2</sup>, 5 × 10<sup>15</sup> ions·cm<sup>-2</sup>, 1 × 10<sup>16</sup> ions·cm<sup>-2</sup>, 5 × 10<sup>16</sup> ions·cm<sup>-2</sup> and 1 × 10<sup>17</sup> ions·cm<sup>-2</sup>.

To quantitatively investigate the effects of the C<sup>+</sup> ion beam on the GO films, C1s, O1s and N1s XPS core-level analysis was conducted with detailed composition analyses of the GO films (Table 1). Fig. 6 is C1s core-level XPS spectra of the GO film before and after ion beam irradiation. Previous reported analyses of GO using XPS,<sup>49</sup> show the C1s spectra of GO films could be deconvoluted into three peaks at positions of 284.5 eV, 286.7 eV, and 288.4 eV, corresponding to C-C, C-O, and C=O, respectively. In the C1s spectra of the pristine GO film, two strong peaks representing the C-C and C-O groups were observed. However, all spectra were nearly unimodal for ion beam irradiated GO films, where the graphitic peak<sup>50</sup> located at binding energy of 284.5 ± 0.7 eV was predominant and the carbon-oxygen components (i.e. C-O and C=O groups) were largely eliminated in each sample.



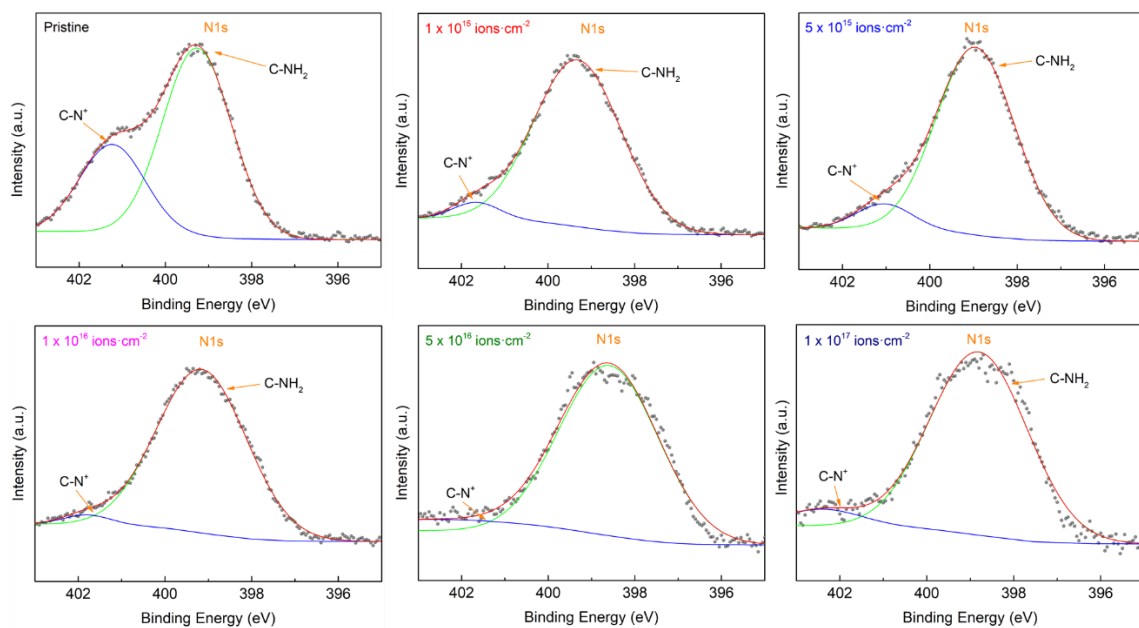
**Fig. 6.** XPS C1s core-level spectra of pristine GO film and GO films irradiated by 40 keV  $C^+$  at fluences of  $1 \times 10^{15} \text{ ions} \cdot \text{cm}^{-2}$ ,  $5 \times 10^{15} \text{ ions} \cdot \text{cm}^{-2}$ ,  $1 \times 10^{16} \text{ ions} \cdot \text{cm}^{-2}$ ,  $5 \times 10^{16} \text{ ions} \cdot \text{cm}^{-2}$  and  $1 \times 10^{17} \text{ ions} \cdot \text{cm}^{-2}$ .

The O1s core-level of the GO films were further characterized (Fig. 7). Peaks at 530.6 eV and 532.9 eV represent the C=O double bond (e.g. C=O or O=C-OH) and the C-O single bond (C-OH), respectively.<sup>51</sup> A significant decrease in intensity of C=O species was found for all irradiated GO films and C=O double bonds in the GO films almost disappeared when irradiated at fluences greater than  $1 \times 10^{16} \text{ ions} \cdot \text{cm}^{-2}$ . The calculated atomic O1s percentage for  $5 \times 10^{16} \text{ ions} \cdot \text{cm}^{-2}$  and  $1 \times 10^{17} \text{ ions} \cdot \text{cm}^{-2}$  irradiated GO films are very close (10.69 % and 10.02 %, respectively) (Table 1). We believe that the C-O single bond comprises of the remaining oxygen component, and it is more stable than the C=O double bond under ion beam irradiation. This is a clear indication that GO films were reduced by the ion beam treatment and that oxygen loss was attributed to the unstable C=O species. We also found that there was a difference in the N1s spectra between the pristine and the ion beam irradiated GO films (Fig. 8).



**Fig. 7.** XPS O1s core-level spectra of pristine GO film and GO films irradiated by 40 keV  $C^+$  at fluences of:  $1 \times 10^{15} \text{ ions} \cdot \text{cm}^{-2}$ ,  $5 \times 10^{15} \text{ ions} \cdot \text{cm}^{-2}$ ,  $1 \times 10^{16} \text{ ions} \cdot \text{cm}^{-2}$ ,  $5 \times 10^{16} \text{ ions} \cdot \text{cm}^{-2}$  and  $1 \times 10^{17} \text{ ions} \cdot \text{cm}^{-2}$ .

The N1s spectra of the GO films could be deconvoluted into two peaks with binding energies of 399.7 and 401.2 eV, corresponding to  $C-NH_2$  and  $C-N^+$ , respectively.<sup>49</sup> The  $C-N^+$  bond on GO film surfaces reduced after ion beam irradiation, with disappearance when treated with an ion beam at fluences above  $1 \times 10^{16} \text{ ions} \cdot \text{cm}^{-2}$ , which is similar to the changes for the  $C=O$  species. Nevertheless, the atomic N1s percentage of the GO films treated with  $1 \times 10^{17} \text{ ions} \cdot \text{cm}^{-2}$  is much lower than that of  $5 \times 10^{16} \text{ ions} \cdot \text{cm}^{-2}$  (4.15 % and 2.76 %, respectively), which implies that the large  $C^+$  ion fluence applied could lead to further loss of the  $C-NH_2$  bond. Ion beam irradiation could efficiently reduce the GO films and the C/O ratio of those irradiated films increased with increasing ion fluence (Table 1). From the quantitative chemical analyses, we found that ion fluence of  $1 \times 10^{16} \text{ ions} \cdot \text{cm}^{-2}$  is the critical transition between GO and the specific “ $C=O$  reduced GO”, which explains and corroborates the changes to morphology and structure revealed using X-ray diffractometry.



**Fig. 8.** XPS N1s core-level spectra of pristine GO film and GO films irradiated by 40 keV  $C^+$  at fluences of:  $1 \times 10^{15} \text{ ions} \cdot \text{cm}^{-2}$ ,  $5 \times 10^{15} \text{ ions} \cdot \text{cm}^{-2}$ ,  $1 \times 10^{16} \text{ ions} \cdot \text{cm}^{-2}$ ,  $5 \times 10^{16} \text{ ions} \cdot \text{cm}^{-2}$  and  $1 \times 10^{17} \text{ ions} \cdot \text{cm}^{-2}$ .

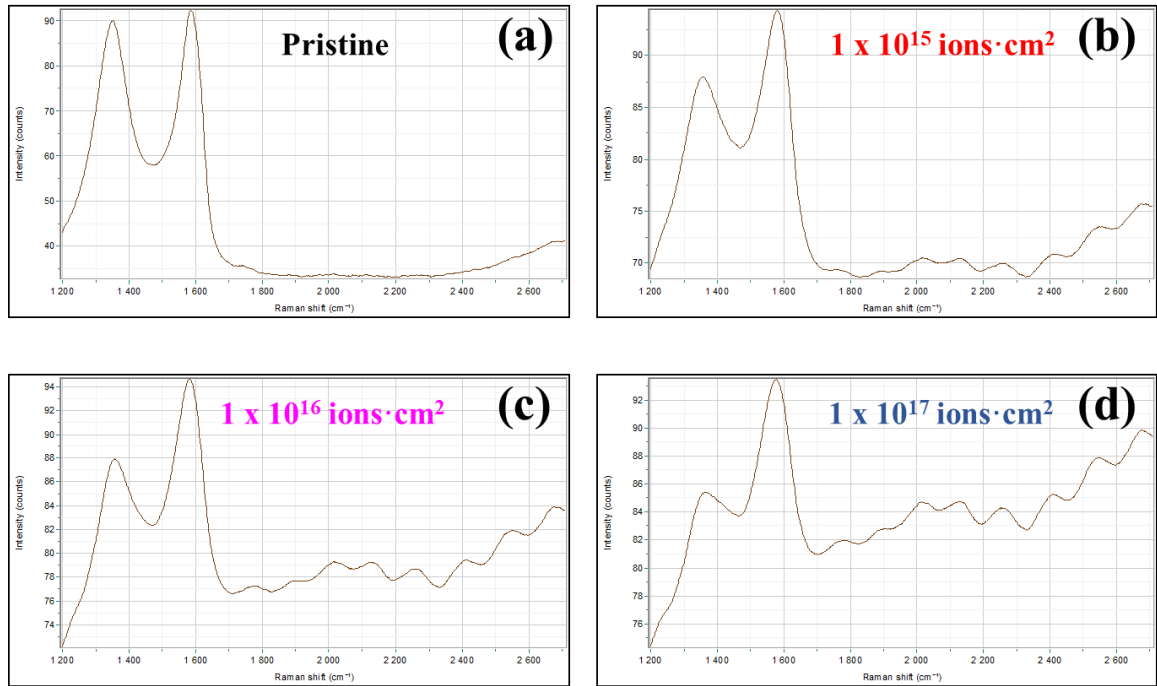
**Table 1** XPS analysis of surface atomic percentage of C1s, O1s and N1s for GO films.

	Atomic C1s [%] <sup>a</sup>	Atomic O1s [%] <sup>b</sup>	Atomic N1s [%] <sup>c</sup>	C/O ratio [-]
Pristine GO film	69.05	24.90	6.05	2.77
$1 \times 10^{15} \text{ cm}^{-2}$	77.14	16.81	6.05	4.59
$5 \times 10^{15} \text{ cm}^{-2}$	77.70	16.46	5.84	4.72
$1 \times 10^{16} \text{ cm}^{-2}$	79.16	15.23	5.61	5.20
$5 \times 10^{16} \text{ cm}^{-2}$	85.15	10.69	4.15	7.97
$1 \times 10^{17} \text{ cm}^{-2}$	87.22	10.02	2.76	8.70

Note: a C1s binding energy: 279.1-297.9 eV; b O1s binding energy: 525.1.1-544.9 eV; c N1s binding energy: 392.1-403.6 eV.

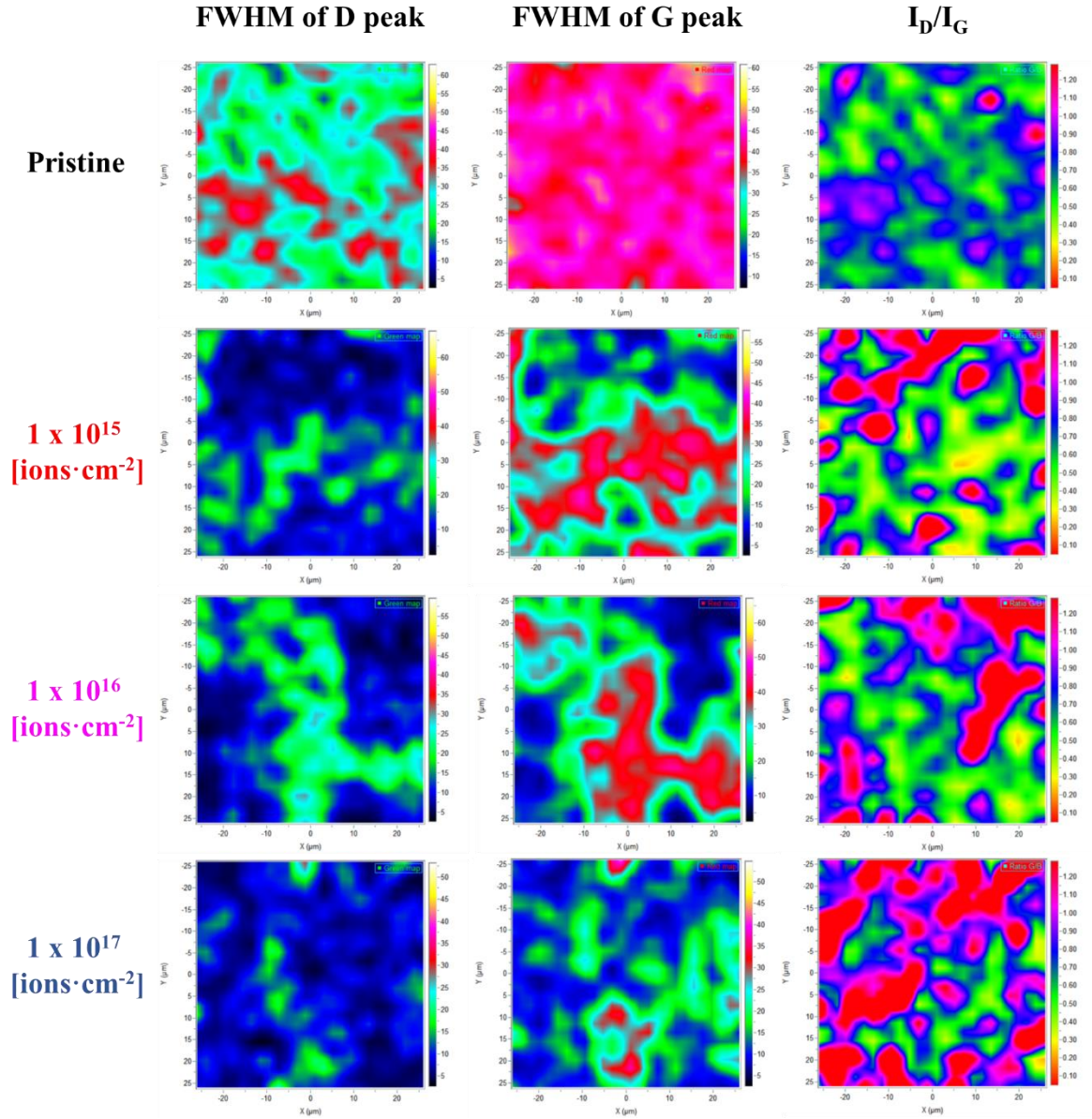
### 3.3. Defect analysis

Raman spectra are widely used to understand defect information of graphene-based materials.<sup>52</sup> For Raman spectra of graphene-based materials, the D peak at about 1330–1340  $\text{cm}^{-1}$  originates from the activated defects of the breathing modes of six-membered rings and the G peak at 1580-1600  $\text{cm}^{-1}$  is attributed to the  $E_{2g}$  phonon at the Brillouin zone center.<sup>53</sup> Generally, GO can also exhibit both intense D and G peaks and the intensity ratio of the D- and G- peaks ( $I_D/I_G$ ) is about 1 with slight fluctuations. The ratio in Raman spectra can be used to evaluate the density and size of defect in GO.<sup>54-55</sup> Fig. 9 demonstrates the average Raman spectra of the pristine GO film and the GO films irradiated by 40 keV  $\text{C}^+$  at fluences of  $1 \times 10^{15} \text{ ions} \cdot \text{cm}^{-2}$ ,  $1 \times 10^{16} \text{ ions} \cdot \text{cm}^{-2}$  and  $1 \times 10^{17} \text{ ions} \cdot \text{cm}^{-2}$  for the selected mapping area of each sample. The pristine GO film exhibited similar intensities for the D and G Raman peak (i.e.  $I_D/I_G \approx 0.98$ ). However, we found all intensities of G peaks in the ion beam irradiated GO films were higher than those of the D peaks, indicating that ion beam irradiation led to defect engineering on the corresponding GO films. The average  $I_D/I_G$  ratios of the three  $\text{C}^+$  irradiated GO films were in the range of 0.90 - 0.93. Eigler et al. established the relation that under laser excitation wavelength of 532 nm, the mean distance between two defects ( $L_D$ ) increase with the increase of  $I_D/I_G$  ratio, given that  $I_D/I_G$  is below 3 and  $L_D$  is between about 1-3 nm.<sup>56</sup> According to their results,  $L_D$  for the three  $\text{C}^+$  irradiated GO films in this work was about 1.42-1.46 nm.



**Fig. 9.** Average Raman spectra of pristine GO film and GO films irradiated by 40 keV C<sup>+</sup> at fluences of:  $1 \times 10^{15}$  ions·cm<sup>-2</sup>,  $1 \times 10^{16}$  ions·cm<sup>-2</sup> and  $1 \times 10^{17}$  ions·cm<sup>-2</sup> for the corresponding mapping area.





**Fig. 10.** Raman maps of D and G FWHM peaks and  $I_D/I_G$  for pristine GO film and GO films irradiated by 40 keV  $C^+$  at fluences of:  $1 \times 10^{15}$  ions·cm $^{-2}$ ,  $1 \times 10^{16}$  ions·cm $^{-2}$  and  $1 \times 10^{17}$  ions·cm $^{-2}$

Fig. 10 shows the intensity maps of D and G full width at half-maximum (FWHM) Raman peaks for pristine GO film and GO films irradiated by 40 keV  $C^+$  at fluences of  $1 \times 10^{15}$  ions·cm $^{-2}$ ,  $1 \times 10^{16}$  ions·cm $^{-2}$  and  $1 \times 10^{17}$  ions·cm $^{-2}$ . The colour bar indicates the intensity of the corresponding peak from weak to strong with the varying colour from blue to yellow. The Raman map for the D FWHM peak of the pristine GO film mainly consisted of green

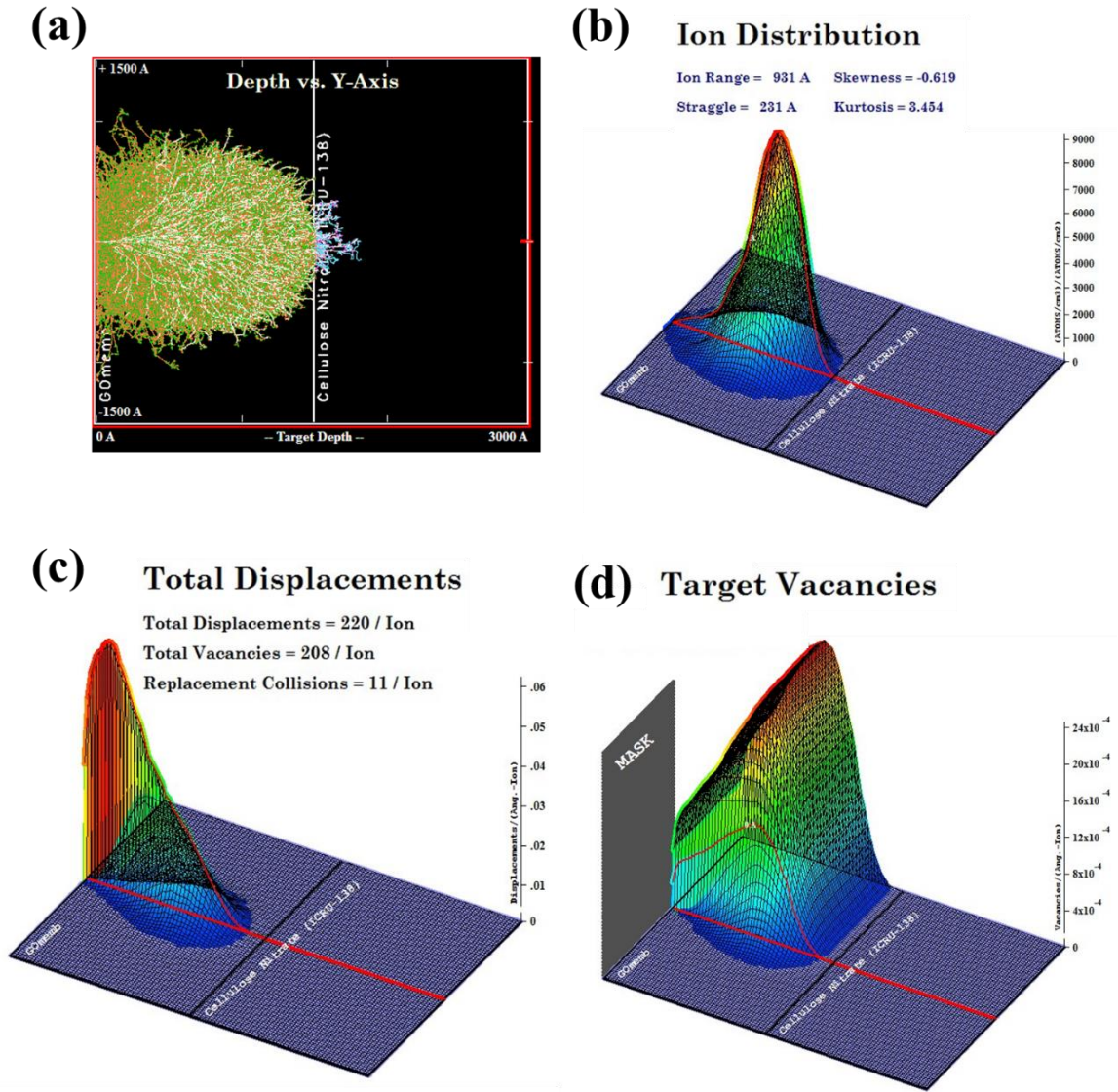


and red regions, while the maps for the D FWHM peaks of the three irradiated GO films mainly consisted of green and blue regions. For the Raman map of G FWHM peaks, the pristine film was almost pink-red while the three irradiated films were blue-red. Therefore, the similar changing tendency in the  $I_D/I_G$  Raman maps of the irradiated GO films confirmed that  $C^+$  irradiation caused similar defect-engineering impact on the films. Significant color changes were observed in FWHM G peak maps of the four GO films, and the size of red regions in the irradiated samples decreased with the increase of the ion fluence. This result indicates that higher ion fluences can drill more defects on GO film surfaces, because the G peak in Raman analysis is highly related to defects in carbon materials.<sup>57-58</sup> We note that analysis of the G peak in Raman spectra for understanding defects in graphene-based materials has been controversial for some time<sup>59</sup> and it is still difficult to precisely analyze defects in GO films using Raman spectroscopy.

### 3.4. SRIM Simulations

To study the treatment of GO films with  $C^+$  beamlines and calculate vacancies generated in the GO films from a theoretical perspective, SRIM simulations were conducted. Figure 11 shows SRIM simulation results for a cubic target cell (XYZ, Z-depth) with each side equal to 300 nm. The 2D presentation of randomly simulated ion cascades in the YZ plane is shown in Fig. 11a. White colored lines represent trajectories of moving incident  $C^+$ . Secondary cascades produced by recoiled C atoms are presented in orange, while green dots represent the calculated resting positions of recoiled (or incident) C atoms (or ions). The 2D projection of spatial distribution of final resting positions of  $C^+$  irradiated in the sample is shown in Fig. 11b. From both Fig. 11a and 11b, the vast majority of ion-target atom interactions took place and the final resting positions of reaction products are within the GO film. Only a very small portion of ion projectiles or secondary recoils reach the substrate filter. The calculated

penetration depth of 40 keV carbon ions in the sample is  $93 \pm 23$  nm. The average lateral straggling is approximately 20 nm. The 2D projection of the calculated average spatial distribution of atomic displacements, i.e. carbon vacancies, generated per ion (impinging normal to the sample surface at  $Y=0$ ) is shown in Fig. 11c. The vacancy distribution is the largest close to the point of entry which is the same for all ions in the simulation, and decreasing (spreading) further deeper in the film as random ion cascades deviate from the initial entry direction along the Z-axis. The raster scanned ion beam causes the movement of the point of entry of ion projectile in the XY plane, so the net result of ion irradiation through a mask is the typical vacancy distribution depth profile shown in Fig. 11d, which is very different from the vacancy profile per ion having the same entry point and direction shown in Fig. 11c. The average linear depth profile of atomic displacement density created in thin GO film increases from  $\sim 1.0 \times 10^{-3} \text{ A}^{-1} \cdot \text{ion}^{-1}$  at the surface to a maximum value of  $2.6 \times 10^{-3} \text{ A}^{-1} \cdot \text{ion}^{-1}$  and decreases sharply to zero close to the end of the ion projected range which is smaller than the thickness of prepared GO film. According to SRIM simulation, an average of 208 carbon vacancies were created in the GO film per impinging  $\text{C}^+$  (Fig. 11c). Assuming that the vacancy depth range coincides with the thickness of GO film (150 nm), the total vacancy concentration ( $V_C$ ) averaged across the whole GO film thickness, which is obtained for irradiation of GO film with ion fluences of  $1 \times 10^{15} \text{ ions} \cdot \text{cm}^{-2}$ ,  $1 \times 10^{16} \text{ ions} \cdot \text{cm}^{-2}$  and  $1 \times 10^{17} \text{ ions} \cdot \text{cm}^{-2}$ , is approximately equal to  $1.4 \times 10^{20} \text{ cm}^{-3}$ ,  $1.4 \times 10^{21} \text{ cm}^{-3}$  and  $1.4 \times 10^{22} \text{ cm}^{-3}$ , respectively.



**Fig. 11.** SRIM simulations of (a) ion cascades, (b) 3D ion distribution, (c) 3D total displacements and (d) vacancies distribution for the process of  $C^+$  irradiation on a pristine GO film.

**Table 2** The approximate average vacancy concentration in GO films simulated by SRIM.

Sample No	$\Phi$ [ $\text{cm}^{-2}$ ]	I [A]	T [min]	$V_c$ [ $\text{cm}^{-3}$ ]
1	$1 \times 10^{15}$	1	4	$1.4 \times 10^{20}$
2	$5 \times 10^{15}$	2	10	$6.9 \times 10^{20}$
3	$1 \times 10^{16}$	4	10	$1.4 \times 10^{21}$
4	$5 \times 10^{16}$	6	20	$6.9 \times 10^{21}$
5	$1 \times 10^{17}$	8	55	$1.4 \times 10^{22}$

Note:  $\Phi$ ,  $I$ ,  $T$  and  $V_C$  represent ion fluence, ion beam current, irradiation time and average vacancy concentration, respectively.

#### 4. Conclusions

We investigated the effects of low energy  $C^+$  ion beam irradiation on ultrathin GO films supported by CN filters. Under the same accelerating energy of 40 keV, five ion fluences ranging from  $1 \times 10^{15} \text{ ions}\cdot\text{cm}^{-2}$  to  $1 \times 10^{17} \text{ ions}\cdot\text{cm}^{-2}$  were compared. The physicochemical properties of our films before and after irradiation were characterized by a combination of SEM, AFM, XRD, FTIR, XPS and Raman techniques. The thicknesses of the GO films were unchanged after irradiation, while their surface morphologies were significantly modified by ion beam irradiation. A threshold ion fluence of  $1 \times 10^{16} \text{ ions}\cdot\text{cm}^{-2}$  was found for transitioning between two types of surface morphologies, which was further explained by reduction of the GO films and reflected in the crystal structure in the X-ray diffractometry. We found carbon ion beam irradiation could not change the chemical structure of the GO films, but the unstable functional groups (e.g.  $C=O$  species) were easily removed by ion beam irradiation. Mapping Raman spectroscopy confirmed a mass of defects with mean distance of about 1.4 nm were generated in the GO films after irradiation, and a larger ion fluence resulted in more defects. Based on SRIM simulation, the total vacancy concentrations were  $1.4 \times 10^{20} \text{ cm}^{-3}$ ,  $1.4 \times 10^{21} \text{ cm}^{-3}$  and  $1.4 \times 10^{22} \text{ cm}^{-3}$ , corresponding to ion fluences of  $1 \times 10^{15} \text{ ions}\cdot\text{cm}^{-2}$ ,  $1 \times 10^{16} \text{ ions}\cdot\text{cm}^{-2}$  and  $1 \times 10^{17} \text{ ions}\cdot\text{cm}^{-2}$ , respectively. Our findings offer a promising strategy for controllable post-synthesis modification ultrathin GO membranes with nano-scaled pores for the applications in gas separation and ion sieving.

#### Acknowledgements

I acknowledge the National Collaborative Research Infrastructure Strategy (NCRIS) funding provided by the Australian Government for this research. I thank the Australian Government for my International Research Training Program (iRTP) scholarship. I thank Dr Chao Shen from the Microscopy Unit in the Faculty of Science and Engineering, Macquarie University, Australia for technical assistance.

### **Conflict of Interest**

I declare that I have no conflict of interest.

## References

- (1) Geim, A. K. Graphene: status and prospects. *Science* **2009**, *324* (5934), 1530-4, DOI: 10.1126/science.1158877.
- (2) Geim, A. K.; Novoselov, K. S. The rise of graphene. *Nat Mater* **2007**, *6* (3), 183-91, DOI: 10.1038/nmat1849.
- (3) Perreault, F.; Fonseca de Faria, A.; Elimelech, M. Environmental applications of graphene-based nanomaterials. *Chem Soc Rev* **2015**, *44* (16), 5861-96, DOI: 10.1039/c5cs00021a.
- (4) Stankovich, S.; Dikin, D. A.; Dommett, G. H.; Kohlhaas, K. M.; Zimney, E. J.; Stach, E. A.; Piner, R. D.; Nguyen, S. T.; Ruoff, R. S. Graphene-based composite materials. *Nature* **2006**, *442* (7100), 282-6, DOI: 10.1038/nature04969.
- (5) Zhu, Y.; Murali, S.; Cai, W.; Li, X.; Suk, J. W.; Potts, J. R.; Ruoff, R. S. Graphene and graphene oxide: synthesis, properties, and applications. *Adv Mater* **2010**, *22* (35), 3906-24, DOI: 10.1002/adma.201001068.
- (6) Huang, X.; Yin, Z.; Wu, S.; Qi, X.; He, Q.; Zhang, Q.; Yan, Q.; Boey, F.; Zhang, H. Graphene-based materials: synthesis, characterization, properties, and applications. *Small* **2011**, *7* (14), 1876-902, DOI: 10.1002/smll.201002009.
- (7) Britnell, L.; Gorbachev, R. V.; Jalil, R.; Belle, B. D.; Schedin, F.; Mishchenko, A.; Georgiou, T.; Katsnelson, M. I.; Eaves, L.; Morozov, S. V.; Peres, N. M.; Leist, J.; Geim, A. K.; Novoselov, K. S.; Ponomarenko, L. A. Field-effect tunneling transistor based on vertical graphene heterostructures. *Science* **2012**, *335* (6071), 947-50, DOI: 10.1126/science.1218461.

- (8) Zhu, Y.; Murali, S.; Stoller, M. D.; Ganesh, K. J.; Cai, W.; Ferreira, P. J.; Pirkle, A.; Wallace, R. M.; Cychosz, K. A.; Thommes, M.; Su, D.; Stach, E. A.; Ruoff, R. S. Carbon-based supercapacitors produced by activation of graphene. *Science* **2011**, 332 (6037), 1537-41, DOI: 10.1126/science.1200770.
- (9) Dan, Y.; Lu, Y.; Kybert, N. J.; Luo, Z.; Johnson, A. T. Intrinsic response of graphene vapor sensors. *Nano Lett* **2009**, 9 (4), 1472-5, DOI: 10.1021/nl8033637.
- (10) Yang, Q.; Su, Y.; Chi, C.; Cherian, C. T.; Huang, K.; Kravets, V. G.; Wang, F. C.; Zhang, J. C.; Pratt, A.; Grigorenko, A. N.; Guinea, F.; Geim, A. K.; Nair, R. R. Ultrathin graphene-based membrane with precise molecular sieving and ultrafast solvent permeation. *Nat Mater* **2017**, 16 (12), 1198-1202, DOI: 10.1038/nmat5025.
- (11) Bunch, J. S.; Verbridge, S. S.; Alden, J. S.; van der Zande, A. M.; Parpia, J. M.; Craighead, H. G.; McEuen, P. L. Impermeable atomic membranes from graphene sheets. *Nano Lett* **2008**, 8 (8), 2458-62, DOI: 10.1021/nl801457b.
- (12) Sint, K.; Wang, B.; Kral, P. Selective Ion Passage through Functionalized Graphene Nanopores. *J Am Chem Soc* **2008**, 130 (49), 16448-+, DOI: 10.1021/ja804409f.
- (13) Jiang, D. E.; Cooper, V. R.; Dai, S. Porous Graphene as the Ultimate Membrane for Gas Separation. *Nano Lett* **2009**, 9 (12), 4019-4024, DOI: 10.1021/nl9021946.
- (14) Cohen-Tanugi, D.; Lin, L. C.; Grossman, J. C. Multilayer Nanoporous Graphene Membranes for Water Desalination. *Nano Lett* **2016**, 16 (2), 1027-33, DOI: 10.1021/acs.nanolett.5b04089.



- (15) O'Hern, S. C.; Boutilier, M. S.; Idrobo, J. C.; Song, Y.; Kong, J.; Laoui, T.; Atieh, M.; Karnik, R. Selective ionic transport through tunable subnanometer pores in single-layer graphene membranes. *Nano Lett* **2014**, *14* (3), 1234-41, DOI: 10.1021/nl404118f.
- (16) Surwade, S. P.; Smirnov, S. N.; Vlassiounk, I. V.; Unocic, R. R.; Veith, G. M.; Dai, S.; Mahurin, S. M. Water desalination using nanoporous single-layer graphene. *Nat Nanotechnol* **2015**, *10* (5), 459-64, DOI: 10.1038/nnano.2015.37.
- (17) Compton, O. C.; Nguyen, S. T. Graphene oxide, highly reduced graphene oxide, and graphene: versatile building blocks for carbon-based materials. *Small* **2010**, *6* (6), 711-23, DOI: 10.1002/sml.200901934.
- (18) Gao, W. The chemistry of graphene oxide. In *Graphene oxide*; Springer: 2015; pp 61-95.
- (19) Liu, G.; Jin, W.; Xu, N. Graphene-based membranes. *Chem Soc Rev* **2015**, *44* (15), 5016-30, DOI: 10.1039/c4cs00423j.
- (20) Chen, L.; Shi, G.; Shen, J.; Peng, B.; Zhang, B.; Wang, Y.; Bian, F.; Wang, J.; Li, D.; Qian, Z.; Xu, G.; Liu, G.; Zeng, J.; Zhang, L.; Yang, Y.; Zhou, G.; Wu, M.; Jin, W.; Li, J.; Fang, H. Ion sieving in graphene oxide membranes via cationic control of interlayer spacing. *Nature* **2017**, *550* (7676), 380-383, DOI: 10.1038/nature24044.
- (21) Abraham, J.; Vasu, K. S.; Williams, C. D.; Gopinadhan, K.; Su, Y.; Cherian, C. T.; Dix, J.; Prestat, E.; Haigh, S. J.; Grigorieva, I. V.; Carbone, P.; Geim, A. K.; Nair, R. R. Tunable sieving of ions using graphene oxide membranes. *Nat Nanotechnol* **2017**, *12* (6), 546-550, DOI: 10.1038/nnano.2017.21.

- (22) Vlassiounk, I. V. Water treatment: A scalable graphene-based membrane. *Nat Nanotechnol* **2017**, *12* (11), 1022-1023, DOI: 10.1038/nnano.2017.184.
- (23) Cheng, C.; Jiang, G.; Garvey, C. J.; Wang, Y.; Simon, G. P.; Liu, J. Z.; Li, D. Ion transport in complex layered graphene-based membranes with tuneable interlayer spacing. *Sci Adv* **2016**, *2* (2), e1501272, DOI: 10.1126/sciadv.1501272.
- (24) Guan, K.; Zhao, D.; Zhang, M.; Shen, J.; Zhou, G.; Liu, G.; Jin, W. 3D nanoporous crystals enabled 2D channels in graphene membrane with enhanced water purification performance. *J Membr Sci* **2017**, *542*, 41-51, DOI: 10.1016/j.memsci.2017.07.055.
- (25) Wei, Y.; Zhu, Y.; Jiang, Y. Photocatalytic self-cleaning carbon nitride nanotube intercalated reduced graphene oxide membranes for enhanced water purification. *Chem Eng J* **2019**, *356*, 915-925, DOI: 10.1016/j.cej.2018.09.108.
- (26) Dey, A.; Chroneos, A.; Braithwaite, N. S. J.; Gandhiraman, R. P.; Krishnamurthy, S. Plasma engineering of graphene. *Appl Phys Rev* **2016**, *3* (2), DOI: 10.1063/1.4947188.
- (27) Yoo, J. H.; Kim, E.; Hwang, D. J. Femtosecond laser patterning, synthesis, defect formation, and structural modification of atomic layered materials. *Mrs Bull* **2016**, *41* (12), 1002-1007, DOI: 10.1557/mrs.2016.248.
- (28) Teweldebrhan, D.; Balandin, A. A. Modification of graphene properties due to electron-beam irradiation. *Appl Phys Lett* **2009**, *94* (1), DOI: 10.1063/1.3062851.
- (29) Tapaszto, L.; Dobrik, G.; Nemes-Incze, P.; Vertesy, G.; Lambin, P.; Biro, L. P. Tuning the electronic structure of graphene by ion irradiation. *Phys Rev B* **2008**, *78* (23), DOI: ARTN 23340710.1103/PhysRevB.78.233407.

- (30) Al-Harhi, S. H.; Kara'a, A.; Hysen, T.; Elzain, M.; Al-Hinai, A. T.; Myint, M. T. Z. Evolution of surface morphology and electronic structure of few layer graphene after low energy Ar<sup>+</sup> ion irradiation. *Appl Phys Lett* **2012**, *101* (21), DOI: 10.1063/1.4767290.
- (31) Kim, S.; Ievlev, A. V.; Jakowski, J.; Vlassiuk, I. V.; Sang, X.; Brown, C.; Dyck, O.; Unocic, R. R.; Kalinin, S. V.; Belianinov, A.; Sumpter, B. G.; Jesse, S.; Ovchinnikova, O. S. Multi-purposed Ar gas cluster ion beam processing for graphene engineering. *Carbon* **2018**, *131*, 142-148, DOI: 10.1016/j.carbon.2018.01.098.
- (32) Jang, C. W.; Kim, J. H.; Lee, D. H.; Shin, D. H.; Kim, S.; Choi, S.-H.; Hwang, E.; Elliman, R. G. Effect of stopping-layer-assisted boron-ion implantation on the electrical properties of graphene: Interplay between strain and charge doping. *Carbon* **2017**, *118*, 343-347, DOI: 10.1016/j.carbon.2017.03.058.
- (33) Ahlberg, P.; Johansson, F. O. L.; Zhang, Z. B.; Jansson, U.; Zhang, S. L.; Lindblad, A.; Nyberg, T. Defect formation in graphene during low-energy ion bombardment. *APL Mater* **2016**, *4* (4), DOI: 10.1063/1.4945587.
- (34) Wang, Q.; Shao, Y.; Ge, D.; Yang, Q.; Ren, N. Surface modification of multilayer graphene using Ga ion irradiation. *J Appl Phys* **2015**, *117* (16), DOI: 10.1063/1.4919071.
- (35) Wang, Q.; Mao, W.; Ge, D.; Zhang, Y.; Shao, Y.; Ren, N. Effects of Ga ion-beam irradiation on monolayer graphene. *Appl Phys Lett* **2013**, *103* (7), DOI: 10.1063/1.4818458.
- (36) Xu, Y.; Zhang, K.; Brüsewitz, C.; Wu, X.; Hofsäss, H. C. Investigation of the effect of low energy ion beam irradiation on mono-layer graphene. *AIP Adv* **2013**, *3* (7), DOI: 10.1063/1.4816715.

- (37) Gawlik, G.; Ciepielewski, P.; Jagielski, J.; Baranowski, J. Modification of graphene by ion beam. *Nucl Instrum Meth B* **2017**, *406*, 683-688, DOI: 10.1016/j.nimb.2017.04.054.
- (38) Li, Z.; Chen, F. Ion beam modification of two-dimensional materials: Characterization, properties, and applications. *Appl Phys Rev* **2017**, *4* (1), DOI: 10.1063/1.4977087.
- (39) Malinsky, P.; Mackova, A.; Miksova, R.; Kovacikova, H.; Cutroneo, M.; Luxa, J.; Bousa, D.; Strochova, B.; Sofer, Z. Graphene oxide layers modified by light energetic ions. *Phys Chem Chem Phys* **2017**, *19* (16), 10282-10291, DOI: 10.1039/c6cp08937b.
- (40) Ammar, M. R.; Rouzaud, J. N.; Vaudey, C. E.; Toulhoat, N.; Moncoffre, N. Characterization of graphite implanted with chlorine ions using combined Raman microspectrometry and transmission electron microscopy on thin sections prepared by focused ion beam. *Carbon* **2010**, *48* (4), 1244-1251, DOI: 10.1016/j.carbon.2009.11.049.
- (41) Zhang, Y.; Zhang, S.; Chung, T. S. Nanometric Graphene Oxide Framework Membranes with Enhanced Heavy Metal Removal via Nanofiltration. *Environ Sci Technol* **2015**, *49* (16), 10235-42, DOI: 10.1021/acs.est.5b02086.
- (42) Pastuovic, Z.; Button, D.; Cohen, D.; Fink, D.; Garton, D.; Hotchkis, M.; Ionescu, M.; Long, S.; Levchenko, V.; Mann, M.; Siegele, R.; Smith, A.; Wilcken, K. SIRIUS – A new 6 MV accelerator system for IBA and AMS at ANSTO. *Nucl Instrum Meth B* **2016**, *371*, 142-147, DOI: 10.1016/j.nimb.2015.09.047.
- (43) Mikšová, R.; Macková, A.; Malinský, P.; Sofer, Z. The stopping power and energy straggling of light ions in graphene oxide foils. *Nucl Instrum Meth B* **2017**, *406*, 173-178, DOI: 10.1016/j.nimb.2017.02.069.

- (44) McKenna, A. J.; Trevethan, T.; Latham, C. D.; Young, P. J.; Heggie, M. I. Threshold displacement energy and damage function in graphite from molecular dynamics. *Carbon* **2016**, *99*, 71-78, DOI: 10.1016/j.carbon.2015.11.040.
- (45) Jayalakshmi, G.; Saravanan, K.; Arun, T.; Suresh, K.; Sundaravel, B.; Panigrahi, B. K.; Kanjilal, D. Structure and electron field emission properties of ion beam reduced graphene oxide sheets. *Carbon* **2017**, *119*, 172-178, DOI: 10.1016/j.carbon.2017.04.034.
- (46) Tan, M. H.; Yang, G. H.; Wang, T. J.; Vitidsant, T.; Li, J.; Wei, Q. H.; Ai, P. P.; Wu, M. B.; Zheng, J. T.; Tsubaki, N. Active and regioselective rhodium catalyst supported on reduced graphene oxide for 1-hexene hydroformylation. *Catal Sci Technol* **2016**, *6* (4), 1162-1172, DOI: 10.1039/c5cy01355k.
- (47) Chen, J.; Zhang, G.; Luo, B.; Sun, D.; Yan, X.; Xue, Q. Surface amorphization and deoxygenation of graphene oxide paper by Ti ion implantation. *Carbon* **2011**, *49* (9), 3141-3147, DOI: 10.1016/j.carbon.2011.03.045.
- (48) Pandey, A.; Qureshi, A. Surface modified graphene oxide nanosheets by gold ion implantation as a substrate for surface enhanced Raman scattering. *J Alloy Comp* **2017**, *703*, 500-507, DOI: 10.1016/j.jallcom.2017.02.020.
- (49) Wei, Y.; Jang, C.-H. Liquid crystal as sensing platforms for determining the effect of graphene oxide-based materials on phospholipid membranes and monitoring antibacterial activity. *Sensor Actuat B-Chem* **2018**, *254*, 72-80, DOI: 10.1016/j.snb.2017.07.057.
- (50) Yumitori, S. Correlation of C-1s chemical state intensities with the O-1s intensity in the XPS analysis of anodically oxidized glass-like carbon samples. *J Mater Sci* **2000**, *35* (1), 139-146, DOI: Doi 10.1023/A:1004761103919.

- (51) Oh, Y.; Yoo, J.; Kim, Y.; Yoon, J.; Yoon, H.; Kim, J.; Park, S. Oxygen functional groups and electrochemical capacitive behavior of incompletely reduced graphene oxides as a thin-film electrode of supercapacitor. *Electrochimica Acta* **2014**, *116*, 118, DOI: 10.1016/j.electacta.2013.1.1.040.
- (52) Lucchese, M. M.; Stavale, F.; Ferreira, E. H. M.; Vilani, C.; Moutinho, M. V. O.; Capaz, R. B.; Achete, C. A.; Jorio, A. Quantifying ion-induced defects and Raman relaxation length in graphene. *Carbon* **2010**, *48* (5), 1592-1597, DOI: 10.1016/j.carbon.2009.12.057.
- (53) Cancado, L. G.; Jorio, A.; Ferreira, E. H.; Stavale, F.; Achete, C. A.; Capaz, R. B.; Moutinho, M. V.; Lombardo, A.; Kulmala, T. S.; Ferrari, A. C. Quantifying defects in graphene via Raman spectroscopy at different excitation energies. *Nano Lett* **2011**, *11* (8), 3190-6, DOI: 10.1021/nl201432g.
- (54) Stankovich, S.; Dikin, D. A.; Piner, R. D.; Kohlhaas, K. A.; Kleinhammes, A.; Jia, Y.; Wu, Y.; Nguyen, S. T.; Ruoff, R. S. Synthesis of graphene-based nanosheets via chemical reduction of exfoliated graphite oxide. *Carbon* **2007**, *45* (7), 1558-1565, DOI: 10.1016/j.carbon.2007.02.034.
- (55) Krishnamoorthy, K.; Veerapandian, M.; Yun, K.; Kim, S. J. The chemical and structural analysis of graphene oxide with different degrees of oxidation. *Carbon* **2013**, *53*, 38-49, DOI: 10.1016/j.carbon.2012.10.013.
- (56) Eigler, S.; Dotzer, C.; Hirsch, A. Visualization of defect densities in reduced graphene oxide. *Carbon* **2012**, *50* (10), 3666-3673, DOI: 10.1016/j.carbon.2012.03.039.
- (57) Ferrari, A. C.; Meyer, J. C.; Scardaci, V.; Casiraghi, C.; Lazzeri, M.; Mauri, F.; Piscanec, S.; Jiang, D.; Novoselov, K. S.; Roth, S.; Geim, A. K. Raman spectrum of graphene and

graphene layers. *Phys Rev Lett* **2006**, 97 (18), 187401, DOI: 10.1103/PhysRevLett.97.187401.

(58) Ferrari, A. C. Raman spectroscopy of graphene and graphite: Disorder, electron–phonon coupling, doping and nonadiabatic effects. *Solid State Commun* **2007**, 143 (1-2), 47-57, DOI: 10.1016/j.ssc.2007.03.052.

(59) Feicht, P.; Eigler, S. Defects in Graphene Oxide as Structural Motifs. *ChemNanoMat* **2018**, 4 (3), 244-252, DOI: 10.1002/cnma.201700357.



# Chapter 5 Ion Beam Engineered Graphene Oxide Membranes for Mono-/Di-valent Metal Ion Separation

This chapter consists of:

- Overview
- Motivations and contributions
- Story behind the article
- The article-

Abstract

1. Introduction

2. Materials and methods

2.1. Materials

2.2. Preparation of pristine and ion beam irradiated GO membranes

2.3. Characterization

2.4. Ion permeation tests of membranes

3. Results and discussion

3.1. Characterization of pristine and ion beam irradiated GO membranes

3.2. Analysis of ion-beam induced nanostructure

3.3. Mono-/di-valent metal ion separation performance

4. Conclusions

Reference

Supplementary Information

## 5.1 Overview

The research article forming this chapter has been submitted for publication. Chapter 4 is the first attempt that uses ion beam to modify ultra-thin GO films, focusing on the effects of ion fluence on the change in chemistry and structure of the GO films. This chapter is also a part of the ANSTO collaborative project, which focuses on the preparation of ion beam irradiated GO membranes for ion sieving. The effect of the two key parameters - GO membrane thickness and ion fluence - on the GO structure and the consequent mono-/di-valent metal ions separation performance was investigated. The ion beam induced strategy was also

successfully extended to diamine cross-linked GO membranes for enhanced selectivity, which proves itself in a universal way. The work represents a step towards the development of high-performance GO-based membranes for potential use in water desalination and biomedical applications.

## **5.2 Motivations and contributions**

Like Chapter 4, the motivation for this chapter was to develop ion beam irradiated GO membranes for practical applications. Based on fundamental understanding of the effects of ion beams on thin GO films, the final goal of fabricating GO membranes was attempted in this Chapter.

Y. W. had the idea of tailoring porous structure of GO membrane using ion beams. Y. W. and Z.P. designed and performed the ion beam irradiation experiments. Z. P. performed ion beam implantation and simulations. Y. W. tested and conducted metal ion separation experiments. C. S. and Y. W. characterized the membranes. D. B. Gore supervised the whole project, participated in some experiments and critically revised the manuscript. All authors contributed to data analyse, discussions and manuscript preparation.

## **5.3 Story behind the article**

We were excited when we got the results as presented in Chapter 4, and we stepped forwards to our final goal, making ion beam irradiated GO membranes with high performance. According to the experience from the initial study in Chapter 4, it is possible to develop desalination membranes for ion sieving and gas separation membranes for H<sub>2</sub> separation.

However, when we used the ion beam to treat  $\alpha$ -Al<sub>2</sub>O<sub>3</sub>-supported GO membranes, a very disappointing result was obtained, as the GO layer was damaged by the ion beam (see the photo below). It seemed that more effort should be made if we wanted to find practical outcomes of ion beam modification of the GO membranes.

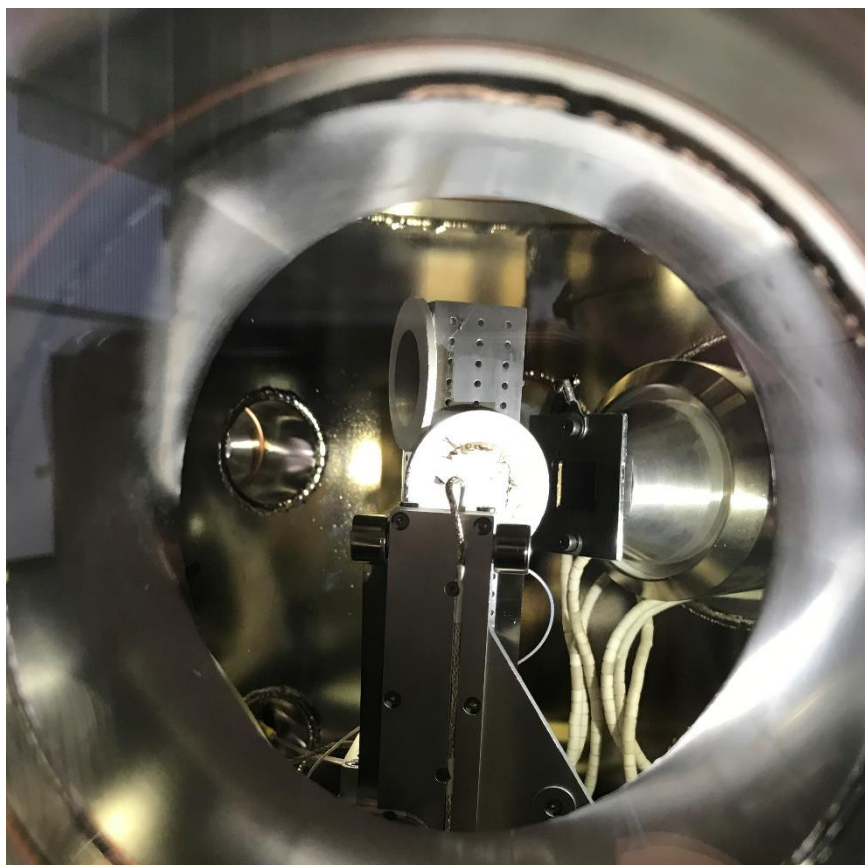


Figure 5.1. Photograph of the damaged  $\alpha$ -Al<sub>2</sub>O<sub>3</sub>-supported GO membranes after ion beam irradiation in the modification chamber.

For ion-sieving application, it is difficult to choose the testing systems. Because the ion beam could only irradiate the GO membrane with the size of  $2\text{ cm} \times 2\text{ cm}$ , the small effective area requires a well-designed and custom-made device if we wanted to know its ion-sieving performance. We have considered gravity-driven filtration and cross-flow filtration. The former exhibited extremely low water permeability because of the small pore size of the as prepared GO membranes; while making a suitable membrane module for the latter is even more difficult. Finally, we decided to use the concentration-driven process to investigate the ion permeation rate for the as-prepared GO membranes.

Although some scientifically interesting findings were collected through this work, more work is worthy of investigating in the near future. For example, the accurate experimental and theoretical approaches of characterizing nano- or sub-nanometer defects created by ion beam modification are yet to be established, and the ion transportation model through the porous reduced GO membranes should be explored. The project will continue to provide more answers to ion beam irradiated 2D-material membranes.

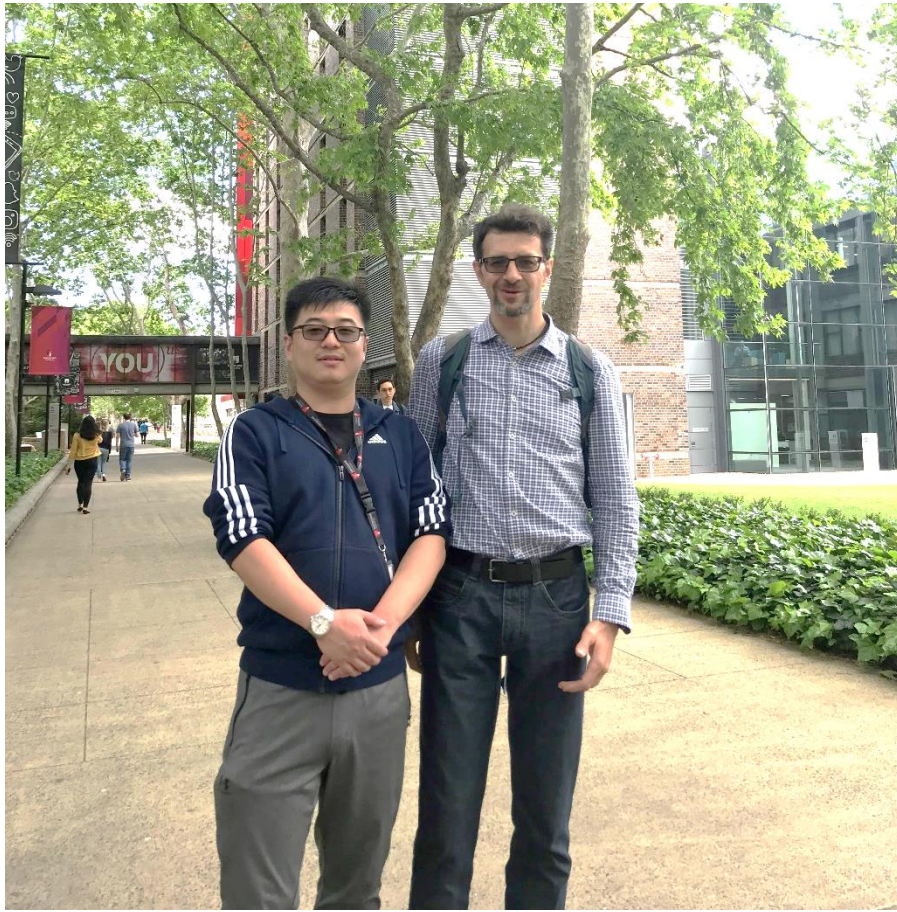


Figure 5.2. Photograph of Yibin and Zeljko in the beautiful Macquarie University North Ryde campus.

## 5.4 The article-

### **Ion beam engineered graphene oxide membranes for mono-/di-valent metal ion separation**

Yibin Wei <sup>a\*</sup>, Zeljko Pastuovic <sup>b</sup>, Chao Shen <sup>c</sup> Damian B. Gore <sup>a</sup>

a. Department of Environmental Sciences, Macquarie University, Sydney, NSW 2109, Australia

b. Centre for Accelerator Science, Australian Nuclear Science and Technology Organization, Sydney, NSW 2234, Australia

c. Faculty of Science and Engineering, Macquarie University, Sydney, NSW 2109, Australia

To whom all correspondence should be addressed.

*\*Tel: +61-2-9850-8337; E-mail: yibin.wei@hdr.mq.edu.au (Y. Wei)*

## Abstract

Graphene oxide (GO) membranes with precisely controlled nanopore are promising for selective ion separation. Here, an ion beam was used to efficiently and simply modify GO membranes, creating nanopores in a controllable manner. We compared the influence of GO membrane thickness and ion fluence on the GO structure and the consequent mono-/di-valent metal ion separation performance. Experimental results indicate all GO membranes exhibited improved  $K^+$  selectivity with respect to other ions after ion beam irradiation. Moreover, the  $K^+$  ion permeation rate of the optimal membranes is up to  $1.4 \times 10^{-3} \text{ mol} \cdot \text{m}^{-2} \cdot \text{h}^{-1}$  and the membrane shows extremely high  $K^+$  separation factor to di-valent ions. Remarkably, this method could be used as an *in-situ* post-treatment for already vacuum-assembled GO membranes. We believe that this strategy offers novel insights into fabricating nanoporous membranes constructed by two-dimensional nanomaterials for a variety of fields including energy, desalination and biomedical applications.

**Keywords:** Graphene oxide; membrane; ion beam; ion sieving; defect

## 1. Introduction

Nanoporous graphene for ionic separation has generated considerable interest for its unparalleled potential in applications such as batteries, biosensors and separation membranes.<sup>[1]</sup> To date, several strategies have been developed to fabricate nanoporous graphene membranes for ion-sieving, including electron beam irradiation,<sup>[2]</sup> ion beam irradiation,<sup>[3]</sup> and electrical pulse.<sup>[4]</sup> However, there remains challenge in fabricating large-scale graphene-based membranes with low cost for practical applications.

The oxidized form of graphene, graphene oxide (GO), has attracted much attention as the alternative product to graphene due to lower production cost. In addition to the inherent properties of graphene, the abundant oxygen-containing groups of GO provides it with diverse possibilities in functionalization.<sup>[5]</sup> Therefore, among graphene-based membranes, GO constructed membranes have been considered the most promising for the sieving of ions and molecules.<sup>[6]</sup> In addition, Hosseini et al.<sup>[7]</sup> predicted that nanoporous GO membranes could exhibit much better water flux and salt rejection when used for reverse osmosis (RO) compared with the performance of graphene, due to the hydrophilic functional groups in GO. Despite this, fabrication of porous GO membranes with ion selectivity is still lacking investigation, because very few effective approaches are capable of achieving precise dimensional control at nanometer-sized pores. Very recently, Li et al.<sup>[8]</sup> reported a combustion synthesis method by partial combustion of hydrotalcite covered GO. They found the resulting nanoporous GO membranes exhibited high selectivity for  $K^+$  to  $Na^+$  with a separation factor of 3.84, but the method still included complicated pretreatment. Hence, general, rapid, simplebut highly controllable routes for fabrication of nanoporous GO membranes are keen to be developed.



Surface modification by ion beam irradiation has been used to create molecular-scale holes (also known as vacancies, defects or pores in different research fields) for monolayer graphene membrane.<sup>[1c]</sup> Such generated nanopores function as membrane channels that regulate ionic flow and molecular transport across the graphene membrane. When massive ions accelerated by dozens of keV impinge on the graphene surface, atomic-scale erosion removes approximately one atom from the surface for every incident ion.<sup>[9]</sup> Moreover, my recent work also confirmed that ion beam irradiation could efficiently alter the chemistry and structure of ultra-thin GO films, along with creating nano-sized pores as well (Chapter 4). Therefore, in this study, I for the first time propose an ion beam-induced method for fabrication of ion-selective GO membranes, with controllable reduction and defect engineering. As opposed to other methods, this process is a facile post-treatment for GO membranes, which does not require a long time. Fundamental understanding of ion beam-induced nanoporous GO membranes were revealed, and structure-property relationships of the ion beam irradiated GO membranes were explored.

## **2. Materials and Methods**

### **2.1. Materials**

Graphene oxide (GO) water dispersion (4 mg/mL) was purchased from Graphenea Corporation. Sodium chloride (NaCl, anhydrous,  $\geq 99.0\%$ ), ethylenediamine (EDA,  $\geq 99.8\%$ ), hydrochloric acid (ACS reagent, 37 %), anhydrous ethanol tris(hydroxymethyl) aminomethane (Tris, ACS reagent,  $\geq 99.8\%$ ) and dopamine hydrochloride ( $\geq 99\%$ ) were purchased from Sigma Aldrich. Potassium chloride (KCl, anhydrous,  $\geq 99.9\%$ ) magnesium chloride ( $\text{MgCl}_2$ , anhydrous,  $\geq 99.0\%$ ), calcium chloride ( $\text{CaCl}_2$ , anhydrous,  $\geq 99.0\%$ ) were purchased from Merck. Cellulose acetate (CA) membranes (diameter: 47 mm; pore size:

0.45  $\mu\text{m}$ ) were purchased from Sterlitech Corporation. Deionized (DI) water ( $18.2 \text{ M}\Omega\cdot\text{cm}^{-1}$  at  $25^\circ\text{C}$ ) was generated by a Milli-Q system and used throughout this study.

## 2.2. Preparation of pristine and ion beam irradiated GO membranes

Pure GO membranes were prepared as similar as one of our previous studies.<sup>[10]</sup> Briefly, CA membrane substrates were pre-treated with polydopamine (PDA) to enhance their adhesive force to GO separation layer. 0.005 mg/mL GO water dispersion was used as membrane casting solution and the loading amount of GO could be controlled by the volume of the GO solution added. Pure GO membranes were then prepared by assembling GO onto PDA-pretreated CA substrates via vacuum suction at room temperature. Finally, pristine GO membranes were obtained after overnight drying at room temperature.

For comparison, diamine and cation cross-linked GO membranes were also prepared. The diamine-modified GO membranes were prepared in the same way as the pure GO membranes preparation procedure except 1 wt% EDA was added to the GO casting solution for cross-linking GO layers. KCl was used as cation source to cross-link GO membrane following a reported method.<sup>[11]</sup> KCl cross-linked GO membranes were produced by immersing pristine GO membranes in 0.25 M KCl solution at room temperature for 1 h and taking them out for overnight drying.

The low energy and high current  $\text{C}^+$  ion beam was produced by a low energy implanter for *in-situ* GO membranes modification. All irradiation was performed using a rapidly-scanning focused carbon beam through a  $2 \text{ cm} \times 2 \text{ cm}$  mask in order to achieve homogenous irradiation. The beam current (i.e. ion fluence) was varied from  $1 \times 10^{15}$  to  $1 \times 10^{17} \text{ ions}\cdot\text{cm}^{-2}$ .

<sup>2</sup>. Details on synthetic parameters of the as-prepared membranes are in Table 1.

Table 1 Comparison of synthetic parameters of M1-M9.

Membrane	Ion fluence (ions/cm <sup>2</sup> )	GO loading amount (mg)	Modification*
M1	$1 \times 10^{16}$	0.25	No
M2	$1 \times 10^{16}$	0.5	No
M3	$1 \times 10^{16}$	1.0	No
M4	$1 \times 10^{15}$	0.5	No
M5	$1 \times 10^{17}$	0.5	No
M6	$1 \times 10^{16}$	0.5	EDA
M7	$1 \times 10^{16}$	0.5	KCl
M8	$1 \times 10^{16}$	1.0	EDA
M9	$1 \times 10^{16}$	1.0	KCl

Note: C<sup>+</sup> ion beam with accelerated energy of 40 keV was used throughout this study. M1-M5 are pure GO membranes irradiated by ion beam only; EDA presents diamine-induced cross-linking of GO by using ethylenediamine before ion beam irradiation; KCl presents cationic ion-induced cross-linking of GO using KCl before ion beam irradiation.

### 2.3. Characterization

Membrane surface morphologies and roughness was analyzed by atomic force microscopy (AFM, Innova, Bruker) with the scan size of  $2.5 \times 2.5 \mu\text{m}$ . Cross-section morphologies of membranes was observed by field emission scanning electron microscopy (FESEM, JSM-7100F, JEOL). An attenuated total reflection Fourier transform infrared (ATR-FTIR, Thermo Nicolet 6700, Thermo Fisher Scientific) spectroscopy was used to record the chemical states of the prepared membranes. The crystalline structure of as-prepared membranes was analyzed by X-ray diffractometry (XRD, X'pert Pro MPD, PANalytical) using Cu K $\alpha$  radiation ( $\lambda = 1.54060 \text{ \AA}$ ) at 40 kV and 15 mA. Raman spectra were recorded on LabRAM (HORIBA) with 512 nm wavelength incident laser light. An X-ray

photoelectron spectrometer (XPS) (ESCALAB 250Xi, Thermo Fisher) equipped with a monochromated Al K $\alpha$  (1486.68 eV) operating at 150 W was used for quantitative elemental analysis. Using the sessile drop method, water contact angles (WCA) of the prepared membranes were measured by a contact angle analyzer (DSA30, KRUSS).

#### 2.4. Ion permeation tests of membranes

The ion permeation performance of pristine and ion beam irradiated GO membranes were comparatively investigated using a home-made diffusion cell (Fig. S1). The membranes were first thoroughly wetted with DI water and then mounted with two gaskets before being clamped onto the cell. The effective membrane area was 0.785 cm<sup>2</sup>. In a typical experiment, one compartment referred to as the feed side was created with 80 mL salt solution (e.g. 0.25 M KCl, NaCl, MgCl<sub>2</sub>, CaCl<sub>2</sub>) while the other compartment referred to as the permeation side, was filled with 80 mL DI water. Continuous magnetic stirring at 500 rpm was introduced to both sides to avoid potential concentration polarization. All experiments were conducted under steady state at 25 °C. The concentration of ions in the permeation side was continuously monitored by an electrical conductivity probe (HACH, HQ40d multi).

The ion permeability P (mol·h<sup>-1</sup>·m<sup>-2</sup>) can be calculated by:

$$P = \frac{\Delta C \times V}{A \times \Delta t} \quad (1)$$

where  $\Delta C$  (mol·L<sup>-1</sup>) is the concentration change in permeation side, V (L) is the volume for permeation side, A (m<sup>2</sup>) is the effective membrane area and  $\Delta t$  (h) is the test time.

The ideal separation factor ( $\alpha$ , i.e. selectivity) was defined as follows:

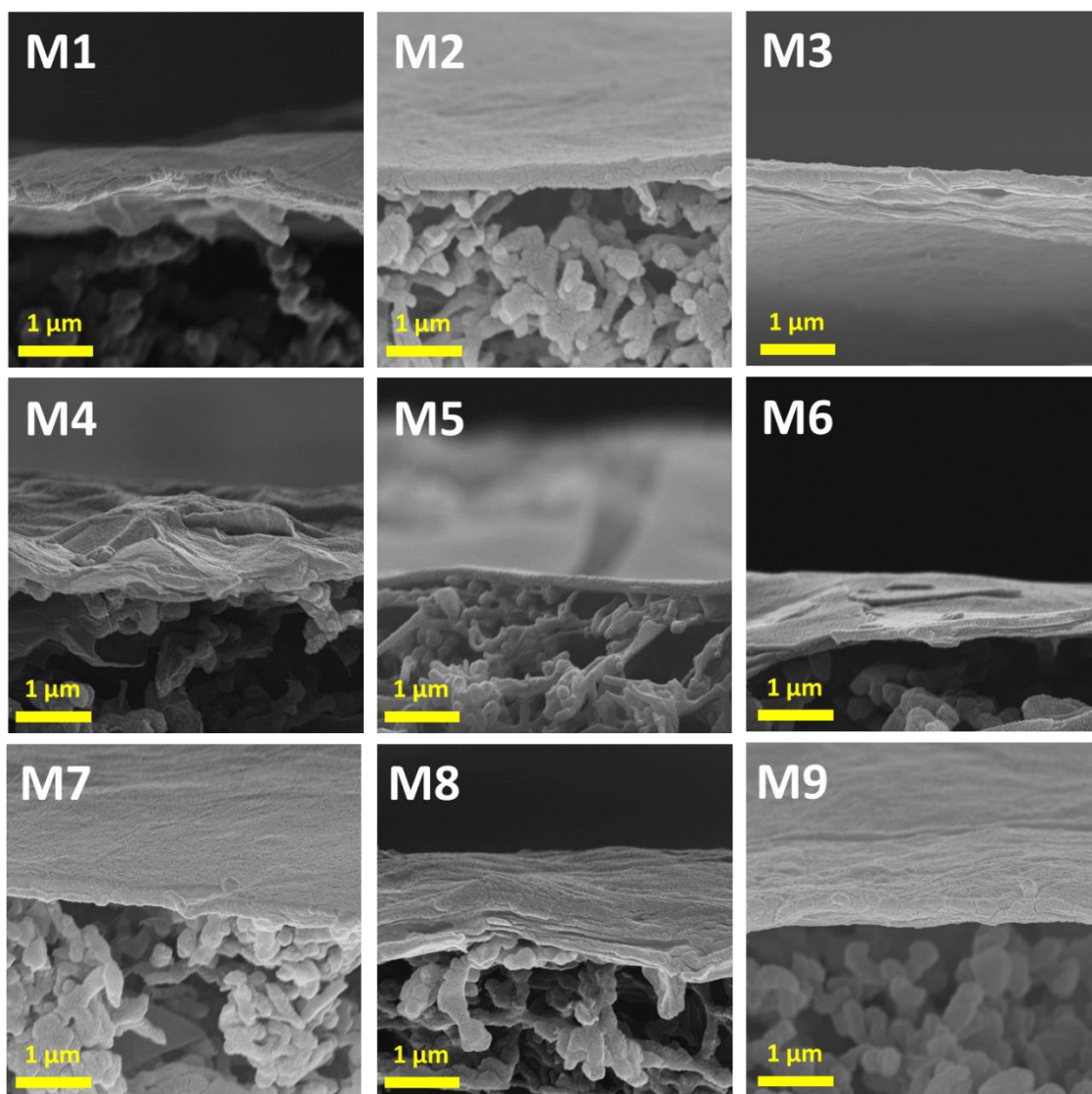
$$\alpha = \frac{P_i}{P_j} \quad (2)$$

where  $P_i$  and  $P_j$  are the ion permeation rates for components  $i$  and  $j$ , respectively.

### **3. Results and Discussion**

#### *3.1. Characterization of pristine and ion beam irradiated GO membranes*

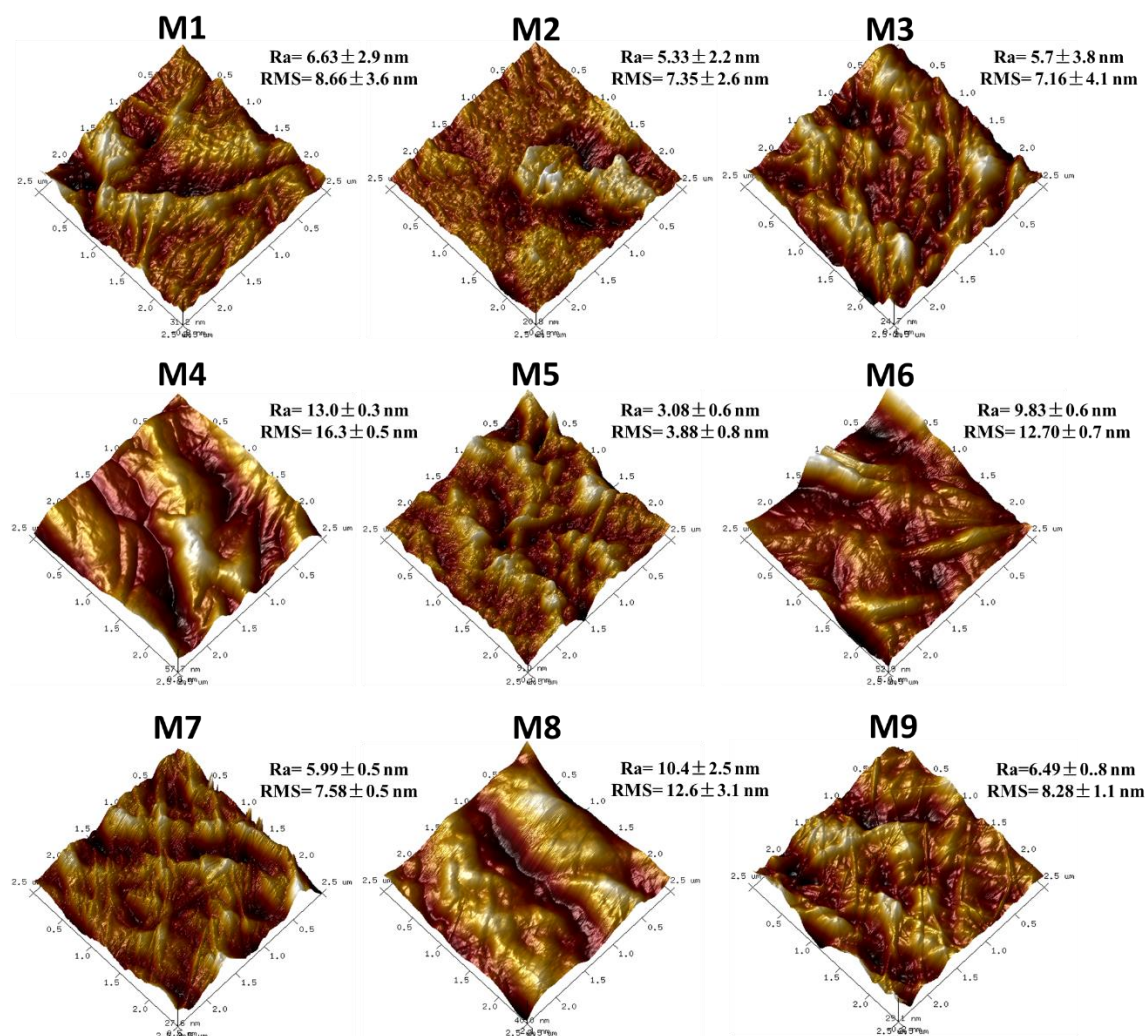
The appearance of the as-prepared GO membranes before and after ion beam irradiation was observed (Fig. S2). The dark regions with size of  $2\text{ cm} \times 2\text{ cm}$  in each sample were irradiated by ion beams while the light regions in each sample are pristine GO membranes. The pristine M1, M2 and M3 are light yellow, yellow and brown, respectively. This suggests that pristine GO membranes with different GO loading amounts were successfully prepared. All ion beam irradiated regions became darker compared with their pristine states. Thus, we can deduce that the pristine GO could be reduced by ion beams under vacuum.



**Fig. 1.** Cross-sectional SEM images of the as-prepared ion beam irradiated membranes.

The cross-sectional morphologies of as-prepared GO membranes before and after ion beam irradiation were imaged using SEM (Fig. S3 and Fig. 1). A crumpled laminar nanostructure of GO was captured in all samples and the laminar structure is attributed to the oxygenated groups and interlayer spacing and the nanosheet folding effect during the deposition.<sup>[12]</sup> Samples M1, M2 and M3 shows GO layers with estimated thickness of 100 nm, 200 nm and 400 nm, respectively (Fig. S3 a-c). This suggests that a higher loading amount of GO led to a thicker layer of GO. In addition, EDA and KCl modification of GO membranes cannot

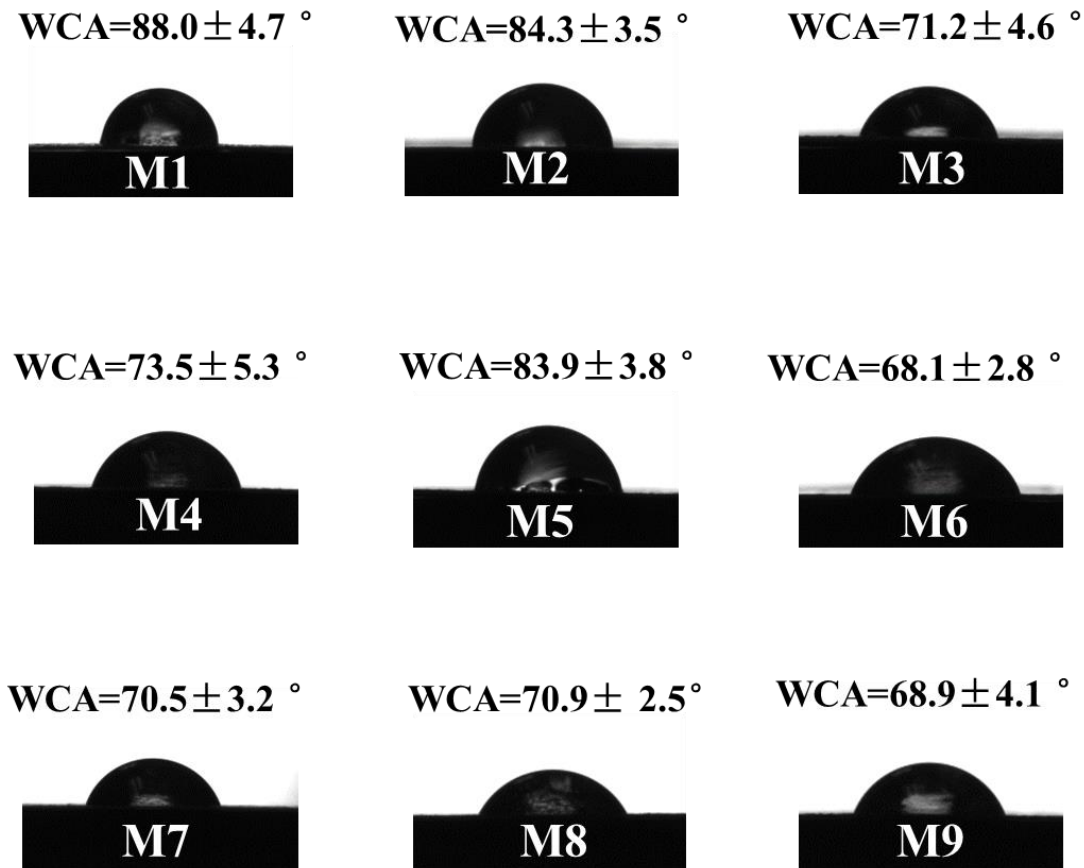
significantly alter the GO crumpled laminar nanostructure. Fig.1 demonstrated that GO laminar nanostructure could be completely preserved after ion beam irradiation.



**Fig. 2.** AFM images of the as-prepared ion beam irradiated membranes.

However, the surface morphologies of GO membranes were obviously changed by ion beam irradiation. Fig. S4 shows the three-dimensional AFM images with roughness parameters of pure GO membrane, and EDA modified GO membrane. The sand dune-like surface structures with valleys and gullies were observed on the three types of GO membranes. The arithmetical roughness (Ra) and root mean squared roughness (RMS) of the pure GO membrane were  $21.8 \pm 3.4$  nm and  $26.6 \pm 4.2$  nm, respectively. The two modified GO

membranes showed significant decreases in surface roughness. In Fig. 2, all of the ion beam irradiated GO membranes exhibited lower roughness compared with their pristine state before irradiation. M4 had the largest roughness values (Ra  $13.0 \pm 0.3$  nm and RMS  $16.3 \pm 0.5$  nm), while M5 had the smallest roughness (Ra  $3.08 \pm 0.6$  nm and RMS  $3.88 \pm 0.8$  nm). This finding suggests the intensity of ion beam could significantly influence the surface morphology of GO membranes and more wrinkles were eliminated by the ion beam, which is consistent with the finding in -Chapter. 4-. Moreover, the roughness of M6 and M8 is similar, which may imply that by using the same ion dose the effect of thickness on surface roughness of the EDA-modified GO membrane is negligible. This also applies to KCl-modified GO membranes since there is no significant roughness change between M7 and M9.

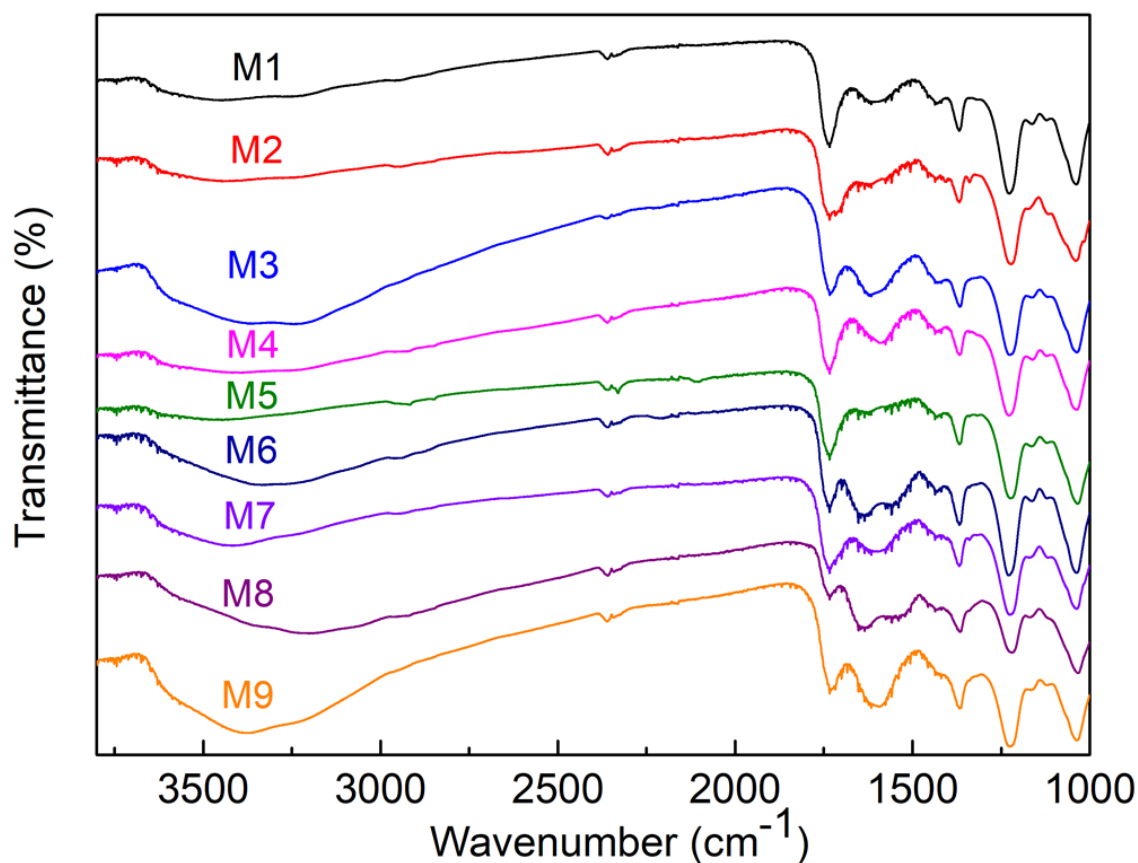


**Fig. 3.** Water contact angles of the as-prepared ion beam irradiated membranes.



WCA analysis is widely used to evaluate surface wettability. The pure GO membrane shows a WCA of  $58.8 \pm 7.7^\circ$ , and the EDA- and KCl- modified GO membranes are a little more hydrophilic with WCA of  $50.9 \pm 4.5^\circ$  and  $52.5 \pm 6.1^\circ$ , respectively (Fig. S4). Fig.3 compares the WCAs of the nine ion beam irradiated GO membranes. All these membranes became relatively hydrophobic after irradiation, which could be explained by the loss of oxygen-containing groups by ion beam treatment. The WCAs of M1, M2 and M3 are  $88.0 \pm 4.7^\circ$ ,  $84.3 \pm 3.5^\circ$  and  $71.2 \pm 4.6^\circ$ , respectively, which suggests that the more hydrophilic oxygen-containing groups were eliminated on the thinnest GO surfaces when treated by the same intensity of ion beam (i.e. ion fluence). M4 and M5 exhibited WCAs of  $73.5 \pm 5.3^\circ$  and  $83.9 \pm 3.8^\circ$ , respectively, and the WCA of M5 is similar to that of M2. This indicates that the ion beam intensity plays a dominant role in GO membrane surface wettability for such GO membranes with same thickness, but there is a threshold for shifting surface wettability. When the ion beam fluence is below  $1 \times 10^{16}$  ions/cm<sup>2</sup> the ion beam could effectively improve the hydrophobicity of pure GO surface, but the hydrophobicity is maintained when using a much higher ion fluence. A similar phenomenon was also in line with findings in -Chapter 4-.

The chemical states of the as-prepared GO membranes were investigated by FTIR. FTIR spectra of pristine CA, pure GO, EDA-modified GO and KCl-modified GO membranes are in Fig. S5a. Typical GO peaks at 1037 cm<sup>-1</sup>, 1223 cm<sup>-1</sup>, 1619 cm<sup>-1</sup>, 1738 cm<sup>-1</sup> and 1630 cm<sup>-1</sup> represent C-O, C-OH, C=C, C=O, and O-H bonds, respectively.<sup>[13]</sup> In the FTIR spectra for ion beam irradiated GO membranes, the peaks representing the above-mentioned oxygen-containing functional groups were found, suggesting that ion beam irradiation could not completely remove the existing functional groups on GO surface.



**Fig. 4.** FTIR spectra of the as-prepared ion beam irradiated membranes.

To further understand the chemical composition changes of GO membranes after ion beam irradiation, XPS analysis was conducted. The details for atomic percentage of carbon, oxygen and nitrogen elements of GO membranes irradiated by different intensity of carbon ions are in Table 2. Pure GO does not contain elemental nitrogen, thus the N1s peak detected in the XPS spectra was sourced from the PDA pre-treatment. The C1s, O1s and N1s XPS core-level analysis were based on peaks at binding energies between the ranges of 279.01-298.91eV, 526.01.1-545.91 eV and 393.01-406.21 eV, respectively. The C/O ratios of pure GO membranes is as low as 2.48, while the GO membrane irradiated by the ion beam with fluence of  $1 \times 10^{17}$  ions/cm<sup>2</sup> exhibited a relatively high C/O ratio of 7.04. The C/O ratios of M2 and M4 are 4.29 and 4.15, respectively. These results confirm that ion beam irradiation is an efficient approach to partially reduce GO. It should be noted that the chemical

composition of M2 and M4 are similar, which also confirms that the ion intensity of  $1 \times 10^{16}$  ions/cm<sup>2</sup> is a threshold when treating GO membranes.

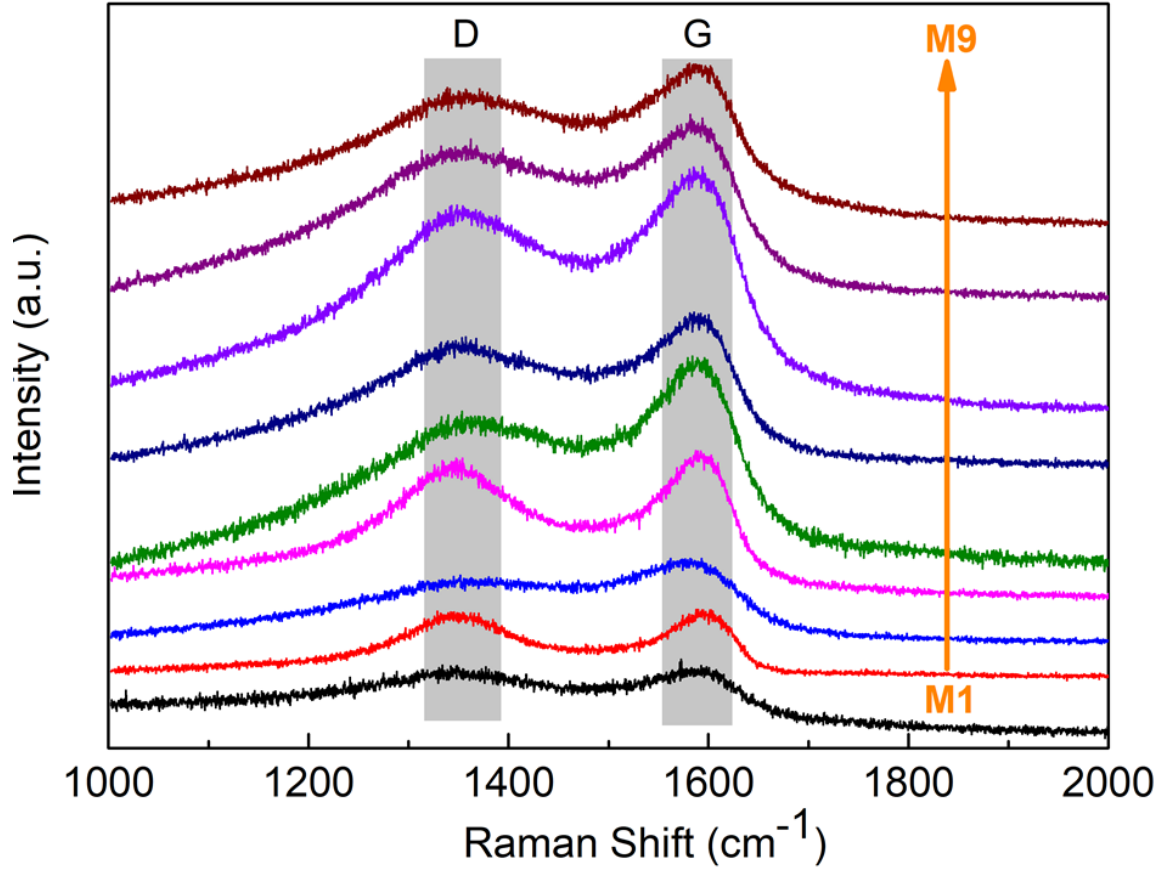
Table 2 XPS analysis of surface atomic percentage of C1s, O1s and N1s for the pure and ion beam irradiated GO membranes with different fluence of ions.

	C1s [%] <sup>a</sup>	O1s [%] <sup>b</sup>	N1s [%] <sup>c</sup>	C/O ratio [-]
Pure GO membrane	69.61	28.10	2.29	2.48
M4 ( $1 \times 10^{15}$ cm <sup>-2</sup> )	79.13	19.07	1.8	4.15
M2 ( $1 \times 10^{16}$ cm <sup>-2</sup> )	79.68	18.58	1.74	4.29
M5 ( $1 \times 10^{17}$ cm <sup>-2</sup> )	86.70	12.30	1	7.04

Note: a C1s binding energy: 279.01-298.91 eV; b O1s binding energy: 526.01-545.91 eV; N1s binding energy: 393.01-406.21 eV.

### 3.2. Analysis of ion-beam induced nanostructure

Raman spectra are widely used to analyse the quality of graphene and its derivatives.<sup>[14]</sup> Pure GO and chemical modified GO membranes exhibit two strong adsorption bands at 1346 and 1596 cm<sup>-1</sup> (Fig. S5b), which correspond to the D- and G-bands, respectively. The intensity ratio of D- and G-band ( $I_D/I_G$ ) can be used for qualitative analysis of the graphene-based material structure, especially defect density and size.<sup>[15]</sup> Fig. 5 is the Raman spectra of ion beam irradiated GO membranes and Table 3 compares the  $I_D/I_G$  ratios of these membranes before and after ion beam irradiation.



**Fig. 5.** Raman spectra of the as-prepared ion beam irradiated membranes.

Raman analysis is established on the model that a defect on the graphene surface causes a circular structural disorder area (region S), which is surrounded by a so-called activated region (region A).<sup>[16]</sup> The gap between the two regions contribute strongly to the D band, whereas the rest area on graphene outside region S contributes to the G band. Structural disorder region S contributes weakly to the D band owing to breakdown of the lattice structure. Defects generated by ion beams at low fluence mostly results in long distances between one defect to another, and the mean distance between defect ( $L_D$ ) is always many times higher than the size of defect. According to the supplement by Cancado et al.<sup>[17]</sup>, when the model is applied to a low-defect density regime ( $L_D \geq 10$  nm) with the radius difference between region A and region S (i.e.  $r_A - r_S$ ) of  $\sim 1$ -2 nm,  $L_D$  could be described as:

$$L_D^2(\text{nm}^2) = \frac{(4.3 \pm 1.3) \times 10^3}{E_L^4} \times \left(\frac{I_D}{I_G}\right)^{-1} \quad (3)$$

The defect density  $n_D$  can be expressed as:

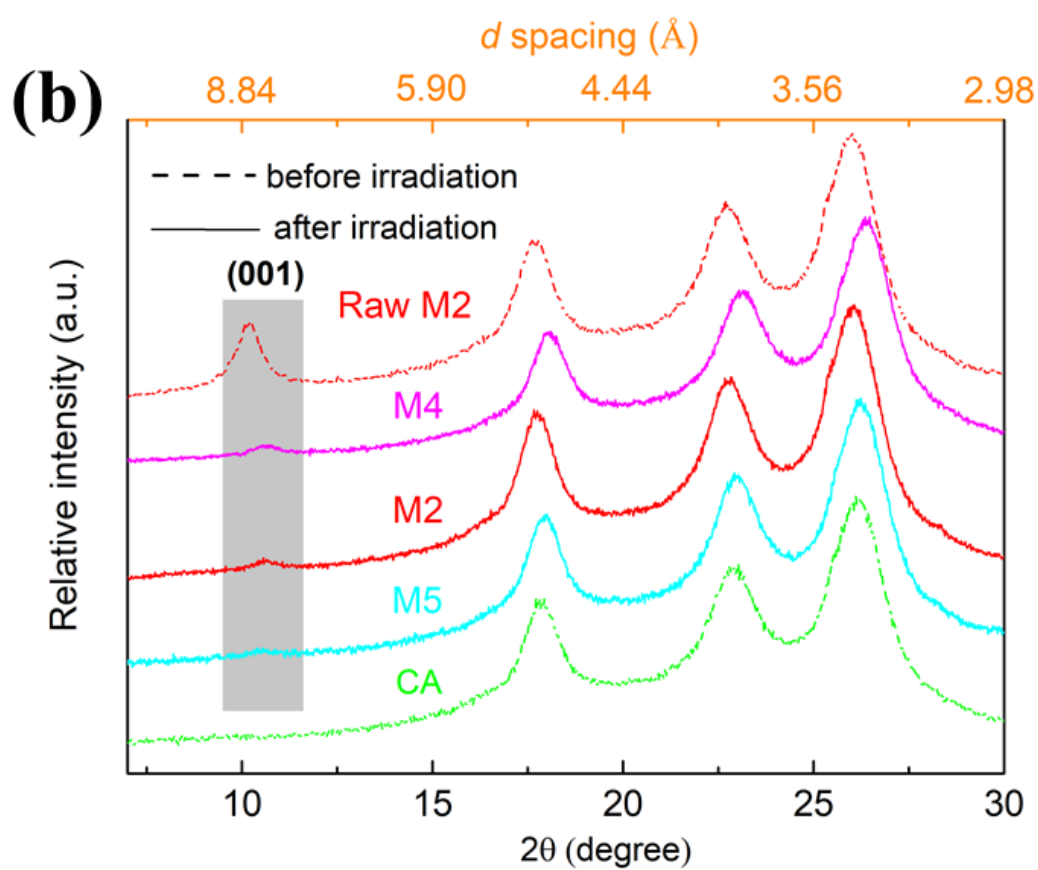
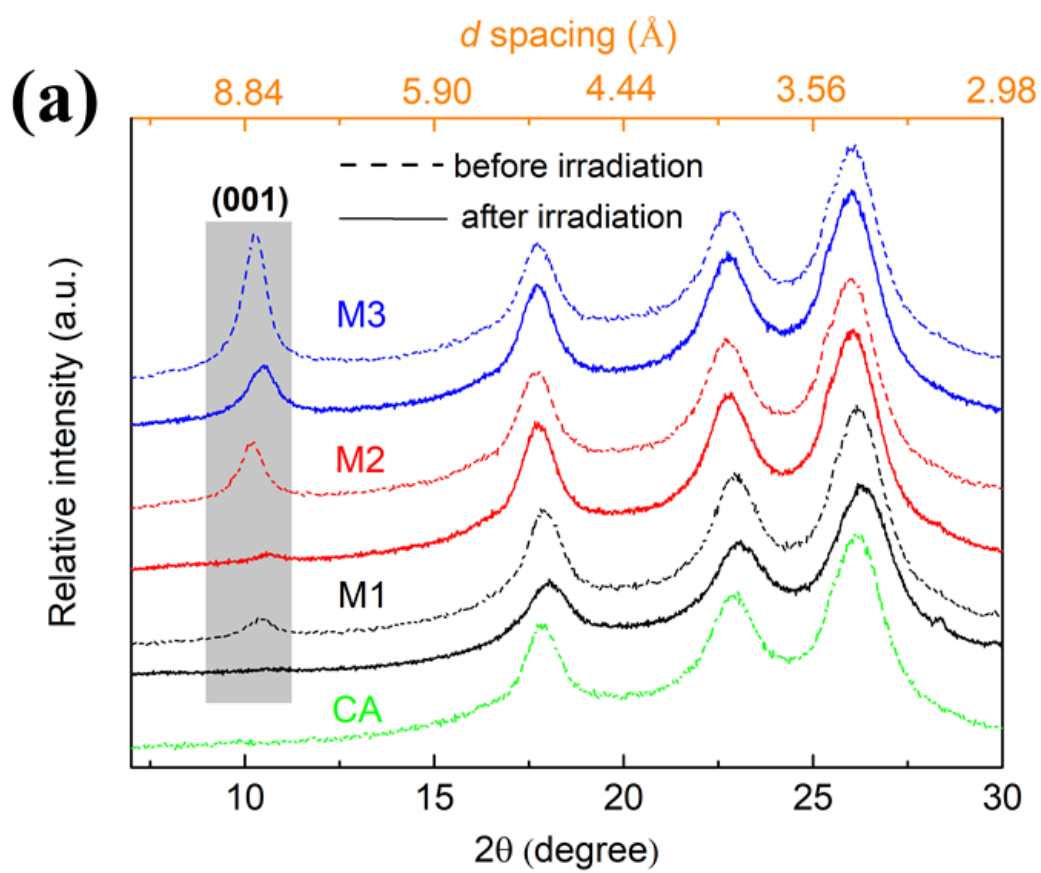
$$n_D(\text{cm}^{-2}) = \frac{1}{L_D^2} \quad (4)$$

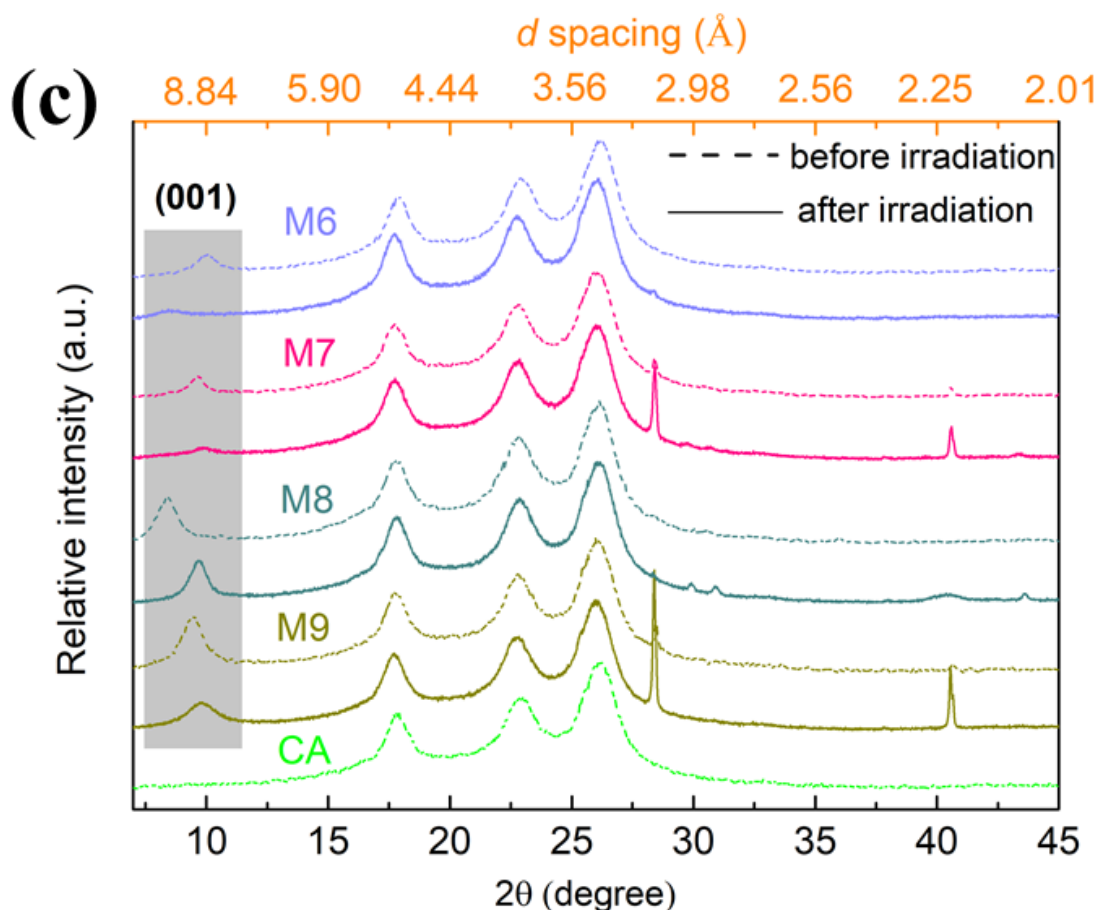
The defect density refers to the density of structural defects in the GO layer, thus it cannot be used to describe point defects on the GO surface. Similar defect densities obtained in this study suggest that carbon ion beams of the energies tested (Table 3) could not change GO two-dimensional nanosheet structures and the point defects created by the ion beam (e.g. resonant scatterers, substitutional atoms) do not have a strong influence on  $I_D/I_G$  ratios. This result matches well with that reported by Cancado et al.<sup>[17]</sup>, indicating nanometer scale point defects  $\sim 1\text{-}2$  nm were also generated as hypothesized. To further understand these point defects from Raman signals, the shape of the G peak might be analysed because strain, intercalants, charged impurities and zigzag edges have strong influences on the G peak.<sup>[18]</sup> However, the existing mechanisms and methods remain controversial.

Table 3 Comparison of  $I_D/I_G$ ,  $L_D$  and  $n_D$  for as-prepared GO membranes analyzed by Raman spectra.

Membrane	$I_D/I_G$	$L_D$ (nm)	$n_D$ (cm <sup>-2</sup> )
Pure GO	$1.03 \pm 0.02$	11.89	0.0071
EDA-GO	$1.07 \pm 0.11$	11.70	0.0073
KCl-GO	$1.27 \pm 0.19$	10.74	0.0087
M1	$1.01 \pm 0.01$	12.04	0.0069
M2	$0.94 \pm 0.05$	12.46	0.0064
M3	$0.88 \pm 0.03$	12.86	0.0060
M4	$0.96 \pm 0.02$	13.33	0.0066
M5	$0.81 \pm 0.02$	12.38	0.0056
M6	$0.88 \pm 0.04$	12.86	0.0060
M7	$0.90 \pm 0.02$	12.76	0.0061
M8	$0.94 \pm 0.08$	12.43	0.0064
M9	$0.87 \pm 0.02$	12.96	0.0060

XRD pattern can be used to analyze the laminar nanostructure of GO-based membranes. The width of 100% GO diffraction peak could be used to study the uniformity of the laminar nanostructure.<sup>[19]</sup> The narrower GO full width at half maximum (FWHM) peak represents a highly concentrated distribution of nanochannel height signals, which implies higher regularity (i.e. greater crystallinity) of the 2D nanostructure. In addition, according to Bragg's Law,<sup>[20]</sup> the interlayer spacing (i.e.  $d$  spacing) of GO membranes could be analysed by the angular position of the GO diffraction peaks. The shift of the GO diffraction peak to lower angle represents the increase of interlayer spacings, while the increase in angle of the GO diffraction peaks represents a decrease in interlayer spacings. Pure GO showed the largest diffraction peak centered at  $\sim 10^\circ$  (Fig 6), corresponding to the characteristic peak (001) of GO.<sup>[21]</sup>





**Fig. 6.** XRD patterns of the as-prepared ion beam irradiated membranes (a) M1-M3, (b) M2, M4-M5 and (c) M6-M9.

Pristine M1, M2 and M3 displays sharply defined GO diffraction peaks, and the GO membrane with a higher GO loading amount showed a relatively strong peak (Fig. 6a). After carbon ion beam irradiation ( $1 \times 10^{16}$  ions/cm<sup>2</sup>), the GO peak in M1 disappeared. Diffraction peaks of GO in M2 and M3 increased in angle suggesting collapse of the interlayer distance, and the diffraction peak of GO in M3 is weaker than that of M2 after ion beam irradiation, indicating a loss of regularity. These results indicate that the GO membrane with low loading amount is easier to be reduced by the ion beam and the interlayer spacing of those GO membranes decreases during reduction. Moreover, with the increase of ion fluence, the relative intensity of GO diffraction peaks of the GO membrane with same thickness became



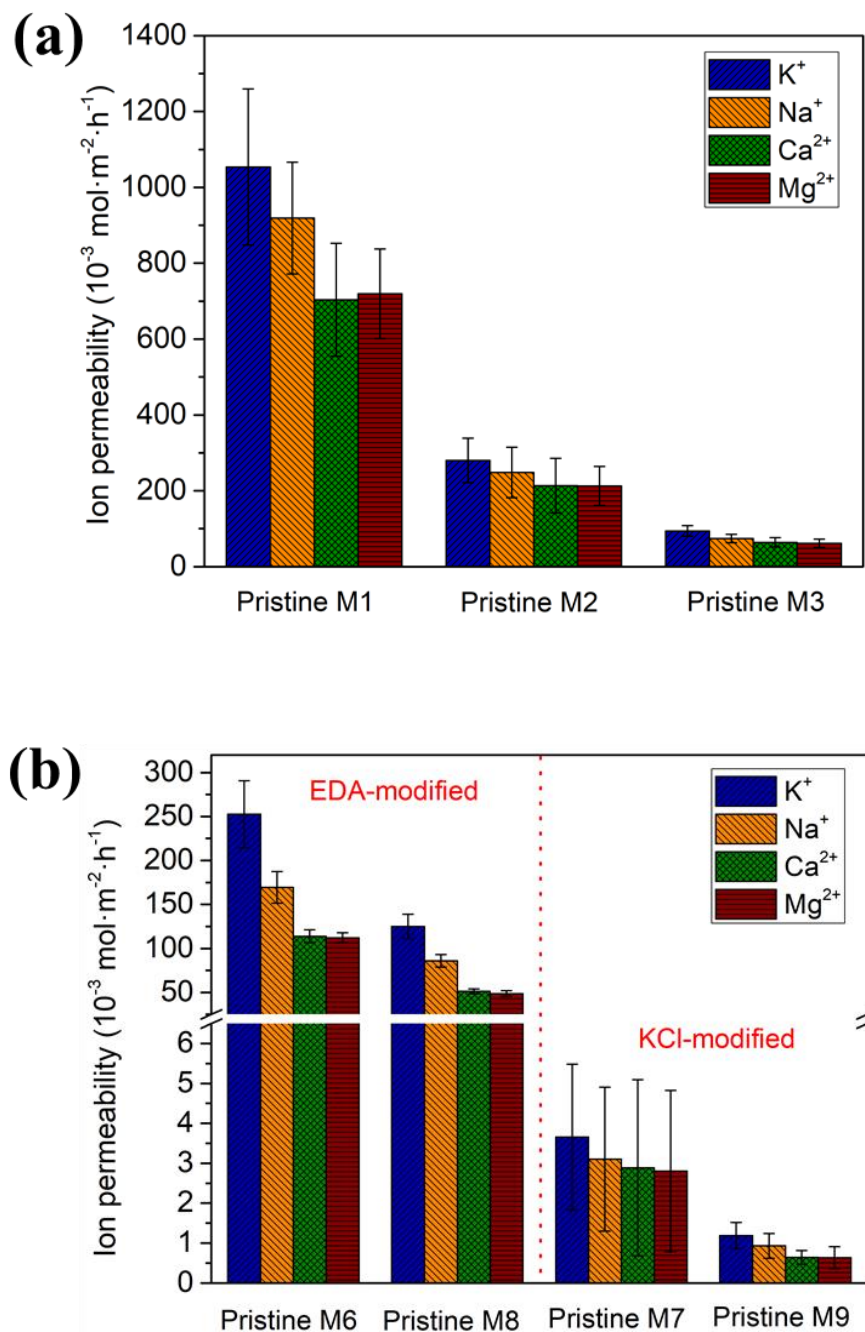
weaker and eventually disappeared (Fig. 6b). The increase in diffracted angle also indicates that the interlayer space became smaller as well. The diminishing GO diffraction peak revealed the increasing degree of deoxygenation or reduction of the GO, which agrees with my previous work -Chapter 4-.

For chemically modified GO membranes, all the GO diffraction peaks of M6, M7, M8 and M9 became weak after irradiation by  $1 \times 10^{16}$  ions·cm<sup>-2</sup> carbon ions. M7 and M9 are KCl-modified GO membranes with GO loading amount of 0.5 mg and 1.0 mg, respectively. In addition to the GO characteristic peak, two strong peaks at 28.3° and 40.6° representing the (200) and (220) planes,<sup>[22]</sup> respectively, were detected, which is an indication that K<sup>+</sup> was successfully incorporated into the GO layers. It is found that the GO peaks for M7 and M9 increased in diffracted angle and became smaller after ion beam irradiation, which is consistent with the change of pure GO membranes (M1-M5). It is worthy of noting that the two peaks corresponding to K<sup>+</sup> became larger after ion beam irradiation.

### 3.3. Mono-/di-valent metal ions separation performance

The mono-/di-valent metal ions sieving performance was tested using a side-by-side diffusion cell. The ion-sieving performances of four metal ions, K<sup>+</sup>, Na<sup>+</sup>, Ca<sup>2+</sup> and Mg<sup>2+</sup> (hydrated radii of 3.31 Å, 3.58 Å, 4.12 Å and 4.28 Å, respectively),<sup>[23]</sup> were tested. The ion permeabilities of K<sup>+</sup>, Na<sup>+</sup>, Ca<sup>2+</sup> and Mg<sup>2+</sup> for M1 without ion beam irradiation (i.e. pristine M1) are 1.05, 0.91, 0.70 and 0.72 mol·m<sup>-2</sup>·h<sup>-1</sup>, respectively (Fig. 7a). Pristine M2 exhibited lower ion permeabilities (K<sup>+</sup>: 0.28 mol·m<sup>-2</sup>·h<sup>-1</sup>, Na<sup>+</sup>: 0.24 mol·m<sup>-2</sup>·h<sup>-1</sup>, Ca<sup>2+</sup>: 0.21 mol·m<sup>-2</sup>·h<sup>-1</sup> and Mg<sup>2+</sup>: 0.21 mol·m<sup>-2</sup>·h<sup>-1</sup>) compared with that of pristine M1. Pristine M3 showed the lowest ion permeabilities of K<sup>+</sup>, Na<sup>+</sup>, Ca<sup>2+</sup> and Mg<sup>2+</sup>, with values of 0.09, 0.07, 0.06 and 0.06 mol·m<sup>-2</sup>·h<sup>-1</sup>, respectively. These results suggest that pure GO membranes could provide nanochannels for ionic transportation and the thickness of the pure GO membrane plays a

dominant role in its ion permeation performance. This may be explained by thinner GO membranes having a lower ion transport resistance.



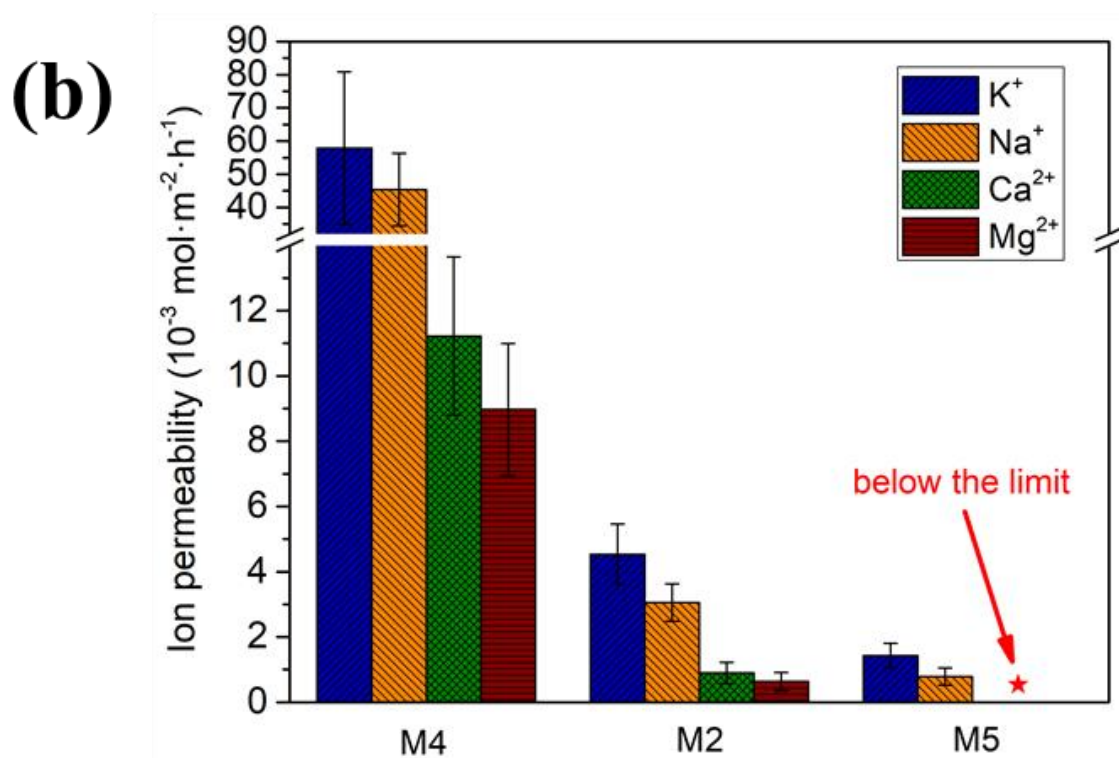
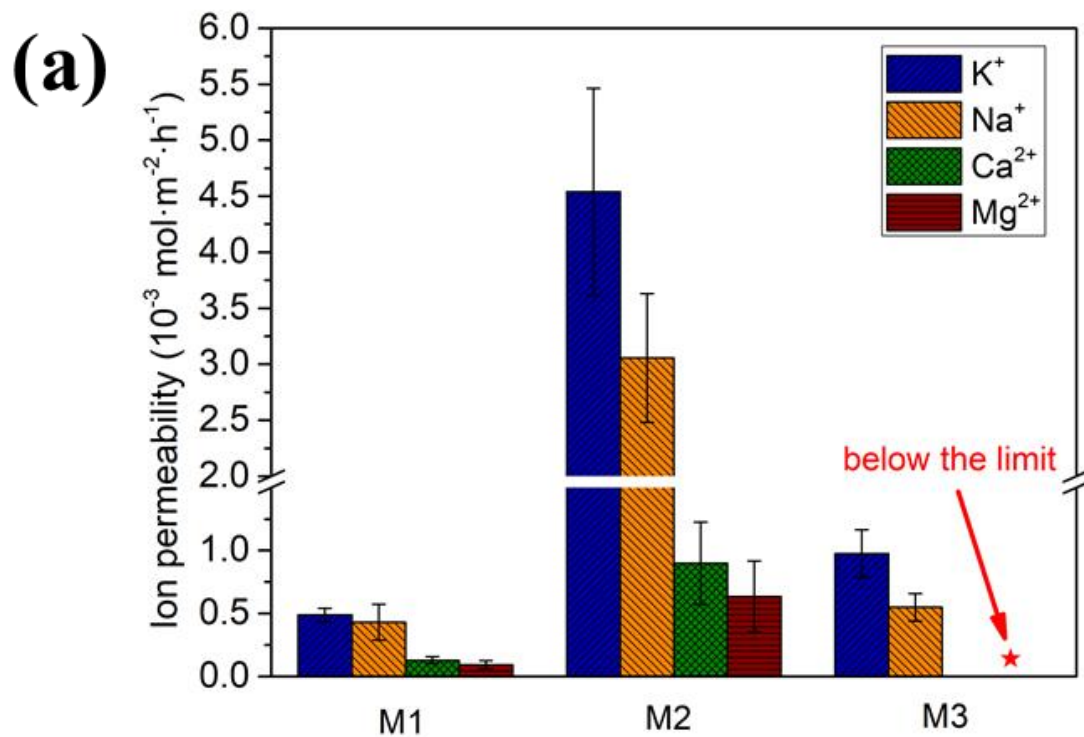
**Fig. 7.** (a) Ion permeabilities of  $\text{K}^+$ ,  $\text{Na}^+$ ,  $\text{Ca}^{2+}$  and  $\text{Mg}^{2+}$  for Pristine M1, Pristine M2 and Pristine M3; (b) ion permeabilities of  $\text{K}^+$ ,  $\text{Na}^+$ ,  $\text{Ca}^{2+}$  and  $\text{Mg}^{2+}$  for Pristine M6, Pristine M7, Pristine M8 and Pristine M9.

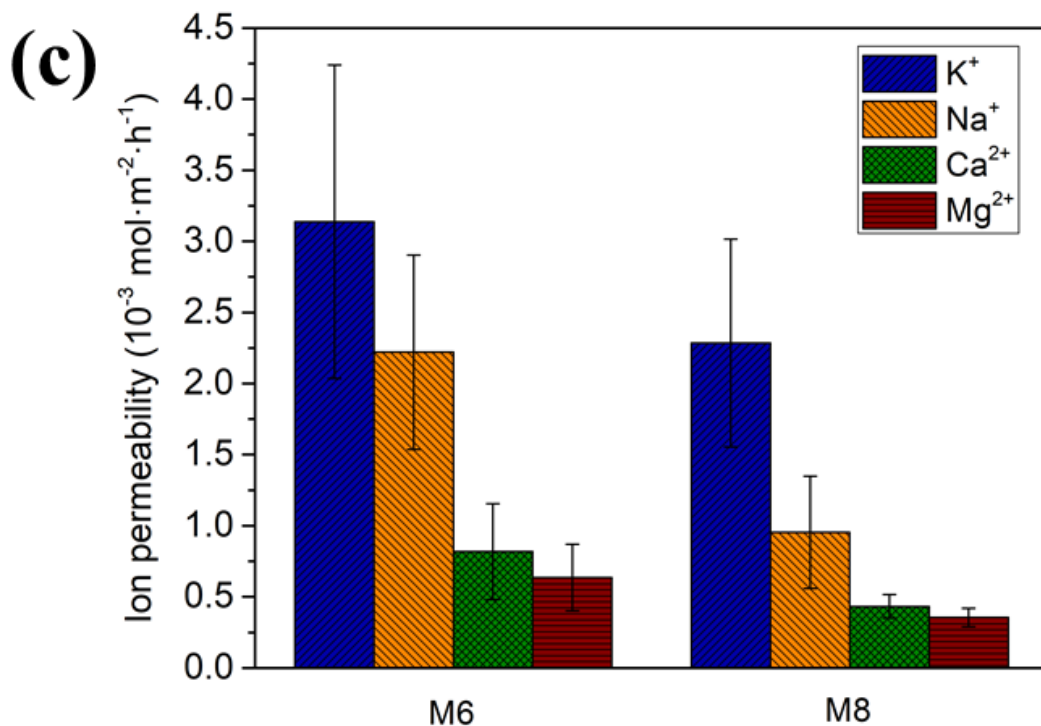
Fig.7b demonstrates the ion permeabilities of  $K^+$ ,  $Na^+$ ,  $Ca^{2+}$  and  $Mg^{2+}$  for EDA- and KCl-modified pristine GO membranes. The ion permeabilities of  $K^+$ ,  $Na^+$ ,  $Ca^{2+}$  and  $Mg^{2+}$  for pristine M6 are 0.25, 0.16, 0.11 and 0.11  $\text{mol}\cdot\text{m}^{-2}\cdot\text{h}^{-1}$ , respectively, and the ion transport performance of pristine M6 is similar to that of pristine M2. However, the  $K^+$  permeability of pristine M6 is more than twice as high as the permeabilities of  $Ca^{2+}$  and  $Mg^{2+}$ , which implies that the EDA-modified GO membranes exhibits selectivity from monovalent to divalent ions. Pristine M8 is EDA-modified GO membranes with a GO loading amount of 1 mg, and the ion permeabilities of the membrane are 0.12, 0.08, 0.05 and 0.05  $\text{mol}\cdot\text{m}^{-2}\cdot\text{h}^{-1}$  for  $K^+$ ,  $Na^+$ ,  $Ca^{2+}$  and  $Mg^{2+}$ , respectively. This result also confirms that thick membranes lead to high ion transport resistance and that the EDA-modified membrane could be used for mono-/di-valent metal ions sieving but with a low separation factor.

The KCl-modified GO membranes showed ultra-low ion permeabilities for  $K^+$ ,  $Na^+$ ,  $Ca^{2+}$  and  $Mg^{2+}$  (Fig, 7b). The ion permeabilities of  $K^+$ ,  $Na^+$ ,  $Ca^{2+}$  and  $Mg^{2+}$  for pristine M7 are  $3.7\times 10^{-3}$   $\text{mol}\cdot\text{m}^{-2}\cdot\text{h}^{-1}$ ,  $3.1\times 10^{-3}$   $\text{mol}\cdot\text{m}^{-2}\cdot\text{h}^{-1}$ ,  $2.9\times 10^{-3}$   $\text{mol}\cdot\text{m}^{-2}\cdot\text{h}^{-1}$  and  $2.8\times 10^{-3}$   $\text{mol}\cdot\text{m}^{-2}\cdot\text{h}^{-1}$ , respectively. Pristine M9 showed much lower ion permeabilities for  $K^+$ ,  $Na^+$ ,  $Ca^{2+}$  and  $Mg^{2+}$  ( $1.2\times 10^{-3}$   $\text{mol}\cdot\text{m}^{-2}\cdot\text{h}^{-1}$ ,  $9.3\times 10^{-4}$   $\text{mol}\cdot\text{m}^{-2}\cdot\text{h}^{-1}$ ,  $6.4\times 10^{-4}$   $\text{mol}\cdot\text{m}^{-2}\cdot\text{h}^{-1}$  and  $6.3\times 10^{-4}$   $\text{mol}\cdot\text{m}^{-2}\cdot\text{h}^{-1}$ , respectively). This result confirms that  $K^+$  could efficiently control the laminar structure of GO membrane for outstanding ion rejection, consistent with a previous report.<sup>[11]</sup>

Fig. 8 shows the ion permeation performance of ion beam irradiated GO membranes. Using the same ion fluence, the effect of GO membrane thickness on the ion permeation performance of ion beam irradiated GO membranes was investigated. M2 exhibited the highest ion permeation rates for the four ions ( $4.5\times 10^{-3}$   $\text{mol}\cdot\text{m}^{-2}\cdot\text{h}^{-1}$  for  $K^+$ ,  $3.1\times 10^{-3}$   $\text{mol}\cdot\text{m}^{-2}\cdot\text{h}^{-1}$  for  $Na^+$ ,  $9.0\times 10^{-4}$   $\text{mol}\cdot\text{m}^{-2}\cdot\text{h}^{-1}$  for  $Ca^{2+}$  and  $6.3\times 10^{-4}$   $\text{mol}\cdot\text{m}^{-2}\cdot\text{h}^{-1}$  for  $Mg^{2+}$  (Fig. 8a). The separation factors for  $K^+/Na^+$ ,  $K^+/Ca^{2+}$  and  $K^+/Mg^{2+}$  were 1.5, 5.1 and 7.1, respectively. The

ion permeation of  $K^+$  for M1 is  $4.9 \times 10^{-4} \text{ mol} \cdot \text{m}^{-2} \cdot \text{h}^{-1}$ , and M1 also displayed good metal ion selectivity with separation factors of 1.1, 3.8 and 5.2 for  $K^+/Na^+$ ,  $K^+/Ca^{2+}$  and  $K^+/Mg^{2+}$ . In addition, the ion permeabilities for  $K^+$  and  $Na^+$  were as low as  $1.9 \times 10^{-3} \text{ mol} \cdot \text{m}^{-2} \cdot \text{h}^{-1}$  and  $1.1 \times 10^{-3} \text{ mol} \cdot \text{m}^{-2} \cdot \text{h}^{-1}$ , respectively. It was surprising that the ion permeabilities for di-valent ions ( $Ca^{2+}$  and  $Mg^{2+}$ ) for M3 were too small to be detected (the detection limits are  $4.8 \times 10^{-5} \text{ mol} \cdot \text{m}^{-2} \cdot \text{h}^{-1}$  for  $Ca^{2+}$  and  $5.6 \times 10^{-5} \text{ mol} \cdot \text{m}^{-2} \cdot \text{h}^{-1}$  for  $Mg^{2+}$ , respectively), indicating that M3 could allow mono-valent ions to pass through with low permeation rate and block divalent ions. Combined with the ion permeation performance of pure GO membranes before and after ion beam irradiation, it can be deduced that ion beam irradiation could significantly reduce the ion permeation rate of the membrane and improve the selectivity for mono/divalent metal ion separation performance due to *in-situ* reduction and nanoscale defect engineering for GO structure, consistent with results in -Chapter 4-.





**Fig. 8.** (a) Ion permeabilities of K<sup>+</sup>, Na<sup>+</sup>, Ca<sup>2+</sup> and Mg<sup>2+</sup> for M1, M2 and M3; (b) ion permeabilities of K<sup>+</sup>, Na<sup>+</sup>, Ca<sup>2+</sup> and Mg<sup>2+</sup> for M2, M4 and M5; (c) ion permeabilities of K<sup>+</sup>, Na<sup>+</sup>, Ca<sup>2+</sup> and Mg<sup>2+</sup> for M6 and M8.

The effect of ion fluence on ion-sieving performance of pure GO membranes was also studied. Fig. 8b compares ion permeation rates of the four ions for M2, M4 and M5. Irradiated by low ion fluence, M4 showed a relatively high ion permeation rate for the four ions. M4 shows K<sup>+</sup> permeation rate of  $2.2 \times 10^{-2} \text{ mol} \cdot \text{m}^{-2} \cdot \text{h}^{-1}$  and its selectivity to other ions are 1.3 for Na<sup>+</sup>, 5.1 for Ca<sup>2+</sup> and 6.4 for Mg<sup>2+</sup>. Notably, the ion permeabilities of K<sup>+</sup> and Na<sup>+</sup> for M5 are  $1.4 \times 10^{-3} \text{ mol} \cdot \text{m}^{-2} \cdot \text{h}^{-1}$  and  $7.9 \times 10^{-4} \text{ mol} \cdot \text{m}^{-2} \cdot \text{h}^{-1}$ , while the ion permeabilities of Ca<sup>2+</sup> and Mg<sup>2+</sup> are below detection limits as well. Based on these results, we believe that ion fluence is a key parameter for tuning the nanostructure of pure GO membranes. The well-known trade-off effect between permeability and selectivity exists in the ion beam irradiated GO membranes.

The effects of ion beams on ion-sieving performance of the chemically modified GO membranes was explored. After irradiation by the carbon ion beam, the KCl-modified GO membranes (M7 and M9) were unstable in water. The GO layers of M7 and M9 were peeled off immediately when immersed in DI water, thus, M7 and M9 could not be used for ion permeation tests. Fig. 8c shows the ion permeation performance of M6 and M8. The  $K^+$  permeabilities of M6 and M8 are  $3.1 \times 10^{-3} \text{ mol} \cdot \text{m}^{-2} \cdot \text{h}^{-1}$  and  $2.2 \times 10^{-3} \text{ mol} \cdot \text{m}^{-2} \cdot \text{h}^{-1}$ , respectively, and the separation factors of  $K^+$  to  $Na^+$  of the two membranes are 1.4 and 2.4. The separation factors of  $K^+$  to divalent metal ions of M6 ( $K^+/Ca^{2+}$  and  $K^+/Mg^{2+}$ ) are 3.8 and 4.9. The  $K^+$ /divalent metal ions separation performance of M6 is slightly higher than that of M8, with separation factors of 5.2 and 6.4 for  $K^+/Ca^{2+}$  and  $K^+/Mg^{2+}$ , respectively. These results suggest that the ion beam technique could be extended to diamine cross-linked GO membranes for enhanced ion sieving performance.

#### 4. Conclusions

In summary, an efficient approach for simultaneous *in-situ* reduction and defect engineering of GO membranes has been developed, by using carbon ion beams. The laminar structure of GO membranes could be controllably tuned in terms of reducing interlayer space and tailoring nanoscale pores, which was reported for the first time. I found that the thickness of the GO layer and the ion fluence applied have enormous influence on the ion beam irradiated GO structure and the consequent mono-/di-valent metal ion separation performance. All of the ion beam irradiated GO membranes exhibited enhanced  $K^+$  selectivity with respect to other ions, when compared with the ion separation performance of the corresponding GO membranes without ion beam treatment. Pure GO membrane with loading amount of 0.5 mg exhibited a  $K^+$  ion permeation rate up to  $1.4 \times 10^{-3} \text{ mol} \cdot \text{m}^{-2} \cdot \text{h}^{-1}$  and the infinite separation factor to divalent ions was found based on our experiment, after ion beam irradiation with

fluence of  $1 \times 10^{16}$  ions·cm<sup>-2</sup>. I found that the ion beam induced strategy was also successfully extended to EDA-modified GO membranes for enhanced selectivity, which holds promise for much broader applicability as well. Overall, this work represents a step towards the development of high-performance GO-based membranes for potential use in water desalination, gas separation and biomedical applications.

### **Acknowledgements**

I thank National Collaborative Research Infrastructure Strategy (NCRIS) funding provided by the Australian Government for this research, the Australian Government for an International Research Training Program (iRTP) scholarship, and staff at the Microscopy Unit, Faculty of Science and Engineering at Macquarie University.

### **Conflict of Interest**

I declare that I have no conflict of interest.



## References

- [1] a) Y. Ito, Y. Tanabe, H. J. Qiu, K. Sugawara, S. Heguri, N. H. Tu, K. K. Huynh, T. Fujita, T. Takahashi, K. Tanigaki, M. Chen, *Angew Chem Int Ed Engl* **2014**, 53, 4822; b) Z. S. Siwy, M. Davenport, *Nat Nanotechnol* **2010**, 5, 697; c) S. P. Surwade, S. N. Smirnov, I. V. Vlassiuk, R. R. Unocic, G. M. Veith, S. Dai, S. M. Mahurin, *Nat Nanotechnol* **2015**, 10, 459; d) H. Lee, T. K. Choi, Y. B. Lee, H. R. Cho, R. Ghaffari, L. Wang, H. J. Choi, T. D. Chung, N. Lu, T. Hyeon, S. H. Choi, D. H. Kim, *Nat Nanotechnol* **2016**, 11, 566; e) Q. Yang, Y. Su, C. Chi, C. T. Cherian, K. Huang, V. G. Kravets, F. C. Wang, J. C. Zhang, A. Pratt, A. N. Grigorenko, F. Guinea, A. K. Geim, R. R. Nair, *Nat Mater* **2017**, 16, 1198; f) L. Madauss, J. Schumacher, M. Ghosh, O. Ochedowski, J. Meyer, H. Lebius, B. Ban-d'Etat, M. E. Toimil-Molares, C. Trautmann, R. G. H. Lammertink, M. Ulbricht, M. Schleberger, *Nanoscale* **2017**, 9, 10487; g) Z. Bai, L. Zhang, H. Li, L. Liu, *ACS Appl Mater Interfaces* **2016**, 8, 24803.
- [2] a) A. J. Storm, J. H. Chen, X. S. Ling, H. W. Zandbergen, C. Dekker, *Nat Mater* **2003**, 2, 537; b) M. D. Fischbein, M. Drndić, *Appl Phys Lett* **2008**, 93, 113107.
- [3] a) Q. Wen, D. Yan, F. Liu, M. Wang, Y. Ling, P. Wang, P. Kluth, D. Schauries, C. Trautmann, P. Apel, W. Guo, G. Xiao, J. Liu, J. Xue, Y. Wang, *Adv Funct Mater* **2016**, 26, 5796; b) Z. Li, Y. Liu, Y. Zhao, X. Zhang, L. Qian, L. Tian, J. Bai, W. Qi, H. Yao, B. Gao, J. Liu, W. Wu, H. Qiu, *Anal Chem* **2016**, 88, 10002.
- [4] R. C. Rollings, A. T. Kuan, J. A. Golovchenko, *Nat Commun* **2016**, 7, 11408.
- [5] Y. Zhu, S. Murali, W. Cai, X. Li, J. W. Suk, J. R. Potts, R. S. Ruoff, *Adv Mater* **2010**, 22, 3906.
- [6] I. V. Vlassiuk, *Nat Nanotechnol* **2017**, 12, 1022.
- [7] M. Hosseini, J. Azamat, H. Erfan-Niya, *Appl Surf Sci* **2018**, 427, 1000.
- [8] Z. Li, X. Zhang, H. Tan, W. Qi, L. Wang, M. C. Ali, H. Zhang, J. Chen, P. Hu, C. Fan, H. Qiu, *Adv Funct Mate* **2018**, 28, 1805026.

- [9] J. Li, D. Stein, C. McMullan, D. Branton, M. J. Aziz, J. A. Golovchenko, *Nature* **2001**, 412, 166.
- [10] Y. Wei, Y. Zhu, Y. Jiang, *Chem Eng J* **2019**, 356, 915.
- [11] L. Chen, G. Shi, J. Shen, B. Peng, B. Zhang, Y. Wang, F. Bian, J. Wang, D. Li, Z. Qian, G. Xu, G. Liu, J. Zeng, L. Zhang, Y. Yang, G. Zhou, M. Wu, W. Jin, J. Li, H. Fang, *Nature* **2017**, 550, 380.
- [12] M. Hu, B. Mi, *Environ Sci Technol* **2013**, 47, 3715.
- [13] Y. Wei, C.-H. Jang, *Sensor Actuat B-Chem* **2018**, 254, 72.
- [14] L. M. Malard, M. A. Pimenta, G. Dresselhaus, M. S. Dresselhaus, *Phys Rep* **2009**, 473, 51.
- [15] J. Chen, G. Zhang, B. Luo, D. Sun, X. Yan, Q. Xue, *Carbon* **2011**, 49, 3141.
- [16] M. M. Lucchese, F. Stavale, E. H. M. Ferreira, C. Vilani, M. V. O. Moutinho, R. B. Capaz, C. A. Achete, A. Jorio, *Carbon* **2010**, 48, 1592.
- [17] L. G. Cancado, A. Jorio, E. H. Ferreira, F. Stavale, C. A. Achete, R. B. Capaz, M. V. Moutinho, A. Lombardo, T. S. Kulmala, A. C. Ferrari, *Nano Lett* **2011**, 11, 3190.
- [18] K.-i. Sasaki, M. Yamamoto, S. Murakami, R. Saito, M. S. Dresselhaus, K. Takai, T. Mori, T. Enoki, K. Wakabayashi, *Phys Rev B* **2009**, 80.
- [19] Y. H. Xi, Z. Liu, J. Y. Ji, Y. Wang, Y. Faraj, Y. D. Zhu, R. Xie, X. J. Ju, W. Wang, X. H. Lu, L. Y. Chu, *J Membr Sci* **2018**, 550, 208.
- [20] W. H. Bragg, W. L. Bragg, *P Roy Soc A* **1913**, 88, 428.
- [21] J. Shen, G. Liu, K. Huang, Z. Chu, W. Jin, N. Xu, *Acs Nano* **2016**, 10, 3398.
- [22] K. S. Lin, Y. J. Mai, S. R. Li, C. W. Shu, C. H. Wang, *J Nanomater* **2012**, DOI: 10.1155/2012/939683.
- [23] E. R. Nightingale, *J Phys Chem* **1959**, 63, 1381.

## **Supplementary Information**

### **Ion beam engineered graphene oxide membranes for mono-/di-valent metal ion separation**

Yibin Wei <sup>a\*</sup>, Zeljko Pastuovic <sup>b</sup>, Chao Shen <sup>c</sup> Damian B. Gore <sup>a</sup>

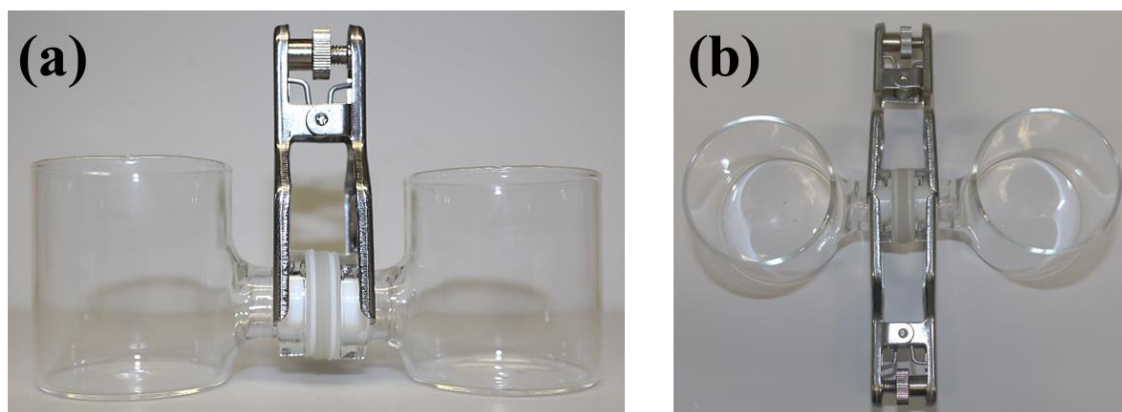
a. Department of Environmental Sciences, Macquarie University, Sydney, NSW 2109, Australia

b. Centre for Accelerator Science, Australian Nuclear Science and Technology Organization, Sydney, NSW 2234, Australia

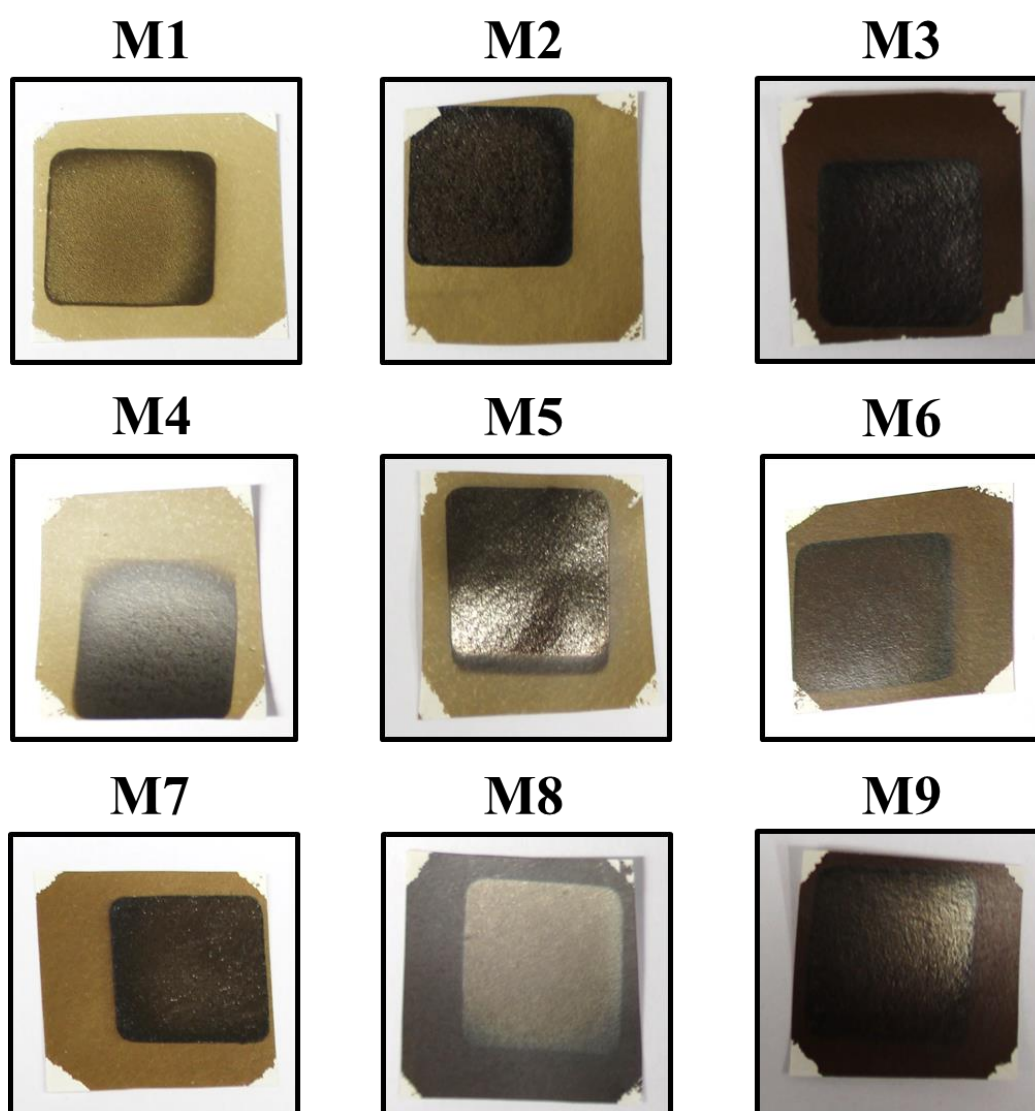
c. Faculty of Science and Engineering, Macquarie University, Sydney, NSW 2109, Australia

To whom all correspondence should be addressed.

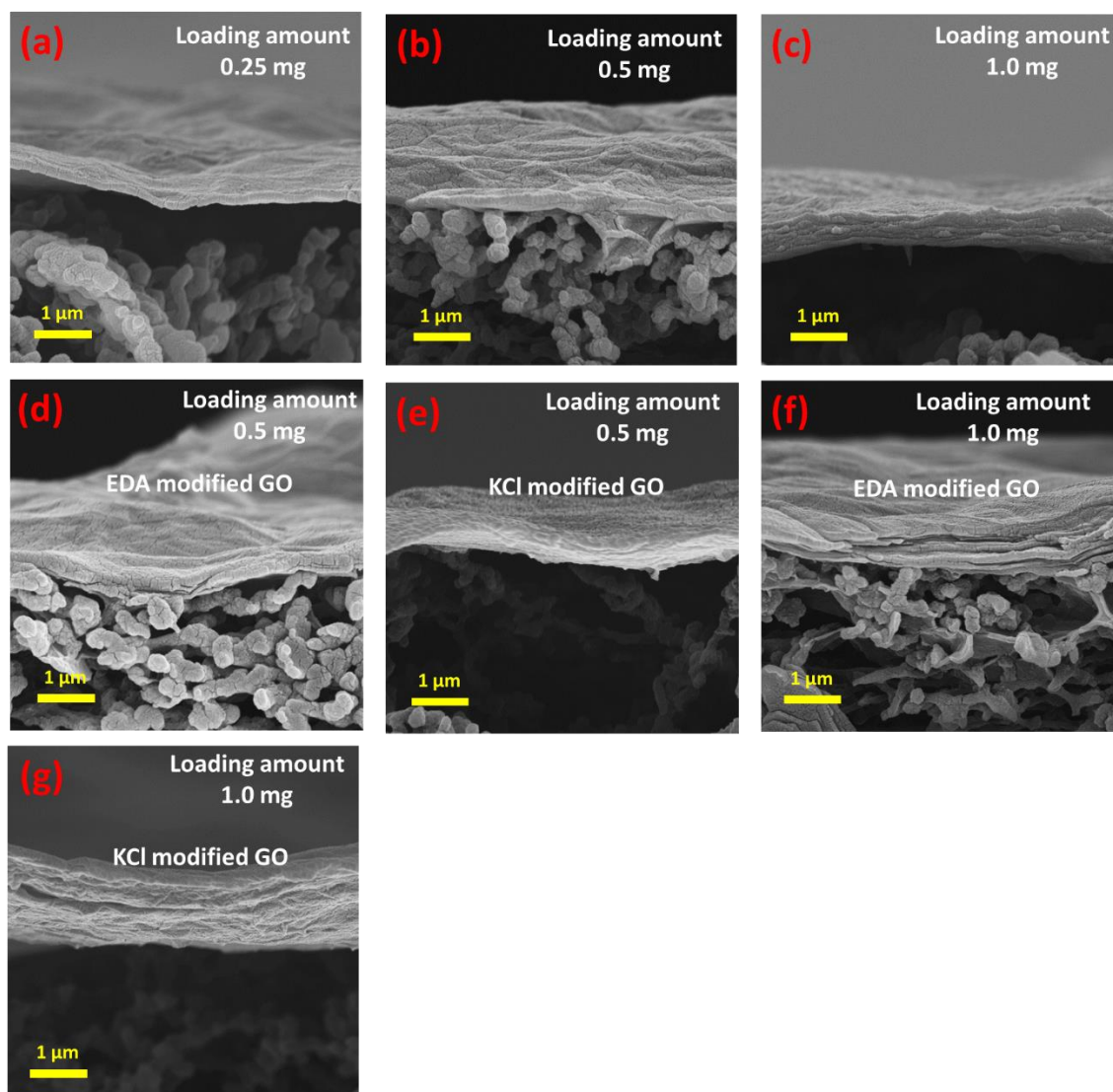
*\*Tel: +61-2-9850-8337; E-mail: yibin.wei@hdr.mq.edu.au (Y. Wei)*



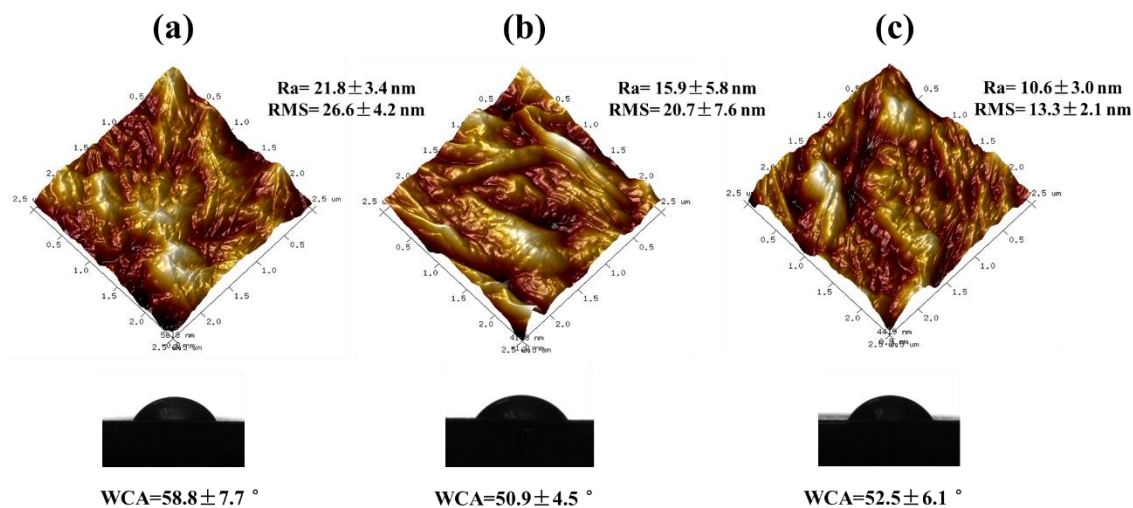
**Fig. S1.** Photographs of the diffusion cell for metal ion sieving: (a) front-view and (b) top-view.



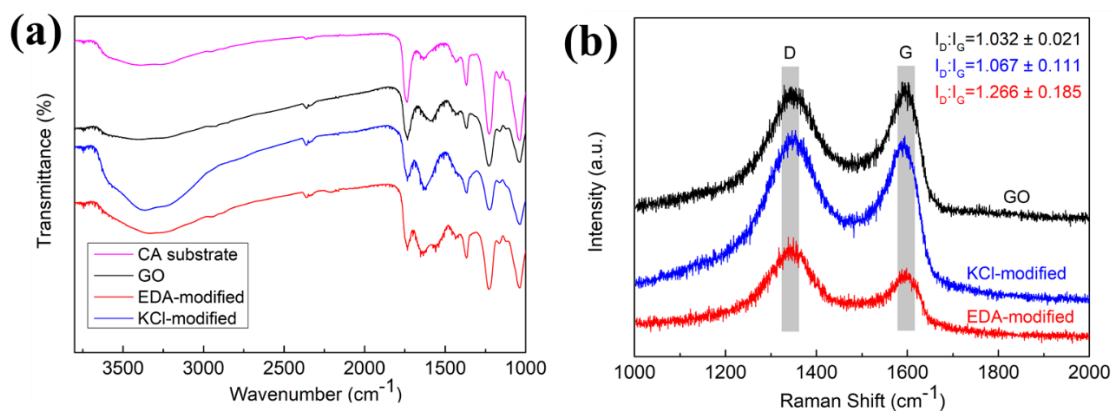
**Fig. S2.** Photographs of the ion beam irradiated GO membranes.



**Fig. S3.** Cross-sectional SEM images of the as-prepared pristine GO membranes: (a) pure GO membranes with GO loading amount of 0.25 mg; (b) 0.5 mg; (c) 1mg; EDA-modified GO membranes with loading amount of (d) 0.5 mg and (f) 1 mg; KCl-modified GO membranes with loading amount of (e) 0.5 mg and (g) 1mg.



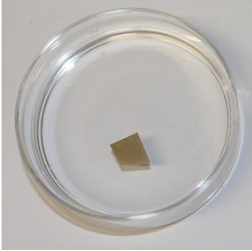
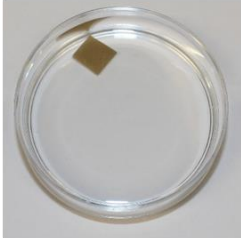
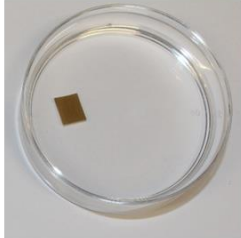
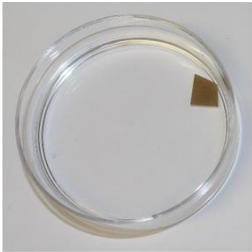
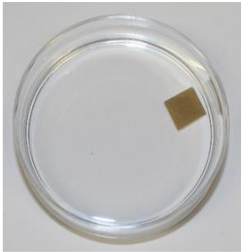
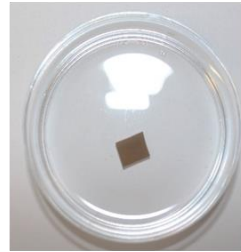
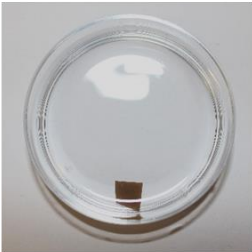

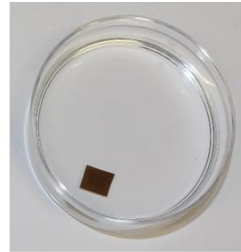
**Fig. S4.** AFM and WCA analysis of (a) pure GO membrane surface, (b) EDA modified GO membrane surface and (c) KCl modified GO membrane surface.



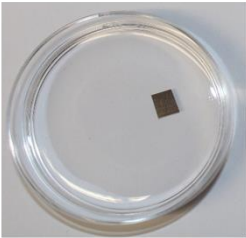
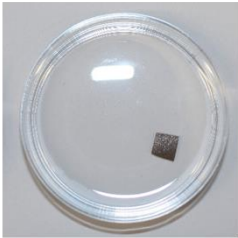
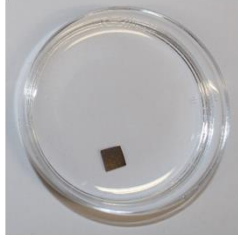
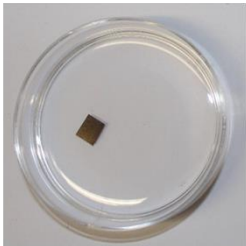
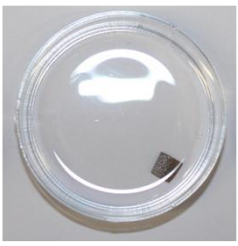
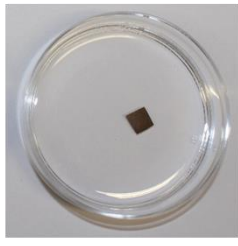
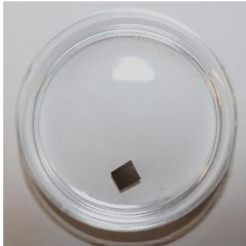
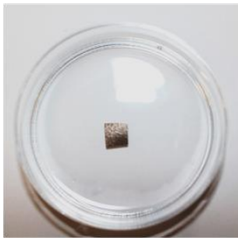
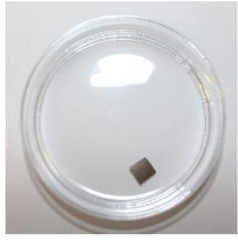
**Fig. S5.** (a) FTIR and (b) Raman spectra of pure GO, EDA-modified and KCl-modified GO membranes.

### *Test of membrane stability in aqueous solutions*

Pure and ion beam irradiated GO membranes (i.e. M2 before and after ion beam irradiation) were cut into about  $0.4\text{ cm} \times 0.4\text{ cm}$  square pieces, and immersed in pure DI water, HCl aqueous solution ( $\text{pH} = 1.8$ ) and NaOH aqueous solution ( $\text{pH} = 11.5$ ) at room temperature in a petri dish. The changes of the immersed membranes were captured for 1 day, 1 week and 1 month, respectively.

<b>(a)</b>	<b>DI water</b>	<b>pH=1.8</b>	<b>pH=11.5</b>
<b>1 day</b>			
<b>1 week</b>			
<b>1 month</b>			



<b>(b)</b>	<b>DI water</b>	<b>pH=1.8</b>	<b>pH=11.5</b>
<b>1 day</b>			
<b>1 week</b>			
<b>1 month</b>			

**Fig. S6.** Photograph of M2 (a) before and (b) after ion beam irradiation when immersed in DI water, acid and base solutions with different time interval.

Fig. S6 demonstrates that pure GO membrane prepared with GO loading amount of 0.5 mg before and after ion beam irradiation displayed excellent stability in DI water, acid and alkali aqueous conditions.



## Chapter 6 Discussion and Summary

This chapter consists of:

- Discussion
  - Summary
  - References
- 

### 6.1 Discussion

The overall aim of the research, which was to tune the laminar structure of GO membranes for improved separation performance based on the two strategies described in the Introduction, has been achieved. The research articles, presented as data chapters (chapters 3-5) within this thesis, form a coherent body of research that provides knowledge and perception of how to construct these state-of-the-art laminar-structured GO membranes for water treatment.

The research article contributing to Chapter 3 has been selected as the 2018 *Grant Edwards Higher Degree Research Paper Award*, in the Department of Environmental Sciences, Macquarie University. The research compared the intercalation effects of different dimensional nanofillers on the laminar structure and separation performance of GO NF membranes. The intercalated  $g\text{-C}_3\text{N}_4$  photocatalysts endowed the composite membranes with visible-light photocatalytic activity for removing organic dyes from polluted water. Intercalated laminar GO structures and photocatalytic membranes are two extremely important areas in current membrane research.

I hypothesized that the introduction of  $g\text{-C}_3\text{N}_4$  photocatalysts into reduced GO laminar structures could improve the water permeability and removal rate for organic pollutants. Based on a comparison of the dye-containing wastewater treatment performance of our composite membranes with other recently reported GO-based NF membranes (Table 6.1), the performance of my  $g\text{-C}_3\text{N}_4/\text{rGO}$  composite NF membranes, especially the  $g\text{-C}_3\text{N}_4\text{NT/rGO}$  membrane, is relatively competitive when applied to the purification of dye-containing wastewater.

When attapulgite (APT) nanorods were intercalated into GO laminates via grafting modification, the water permeability of APT/GO membranes sharply increases to about  $10 \text{ L}\cdot\text{m}^{-2}\cdot\text{h}^{-1}\cdot\text{bar}^{-1}$  while preserving high rejection to dyes [1]. Similarly, Chen et al. [2] successfully developed a series of polyamide (PA)/GO NF membranes and then they investigated the effect of intercalating different nanomaterials into GO laminar structures on the separation performance of the membranes. They also found the intercalation can improve water permeability ( $11.39\text{--}14.82 \text{ L}\cdot\text{m}^{-2}\cdot\text{h}^{-1}\cdot\text{bar}^{-1}$ ) of their membranes while maintaining high dye removal efficiencies ( $> 99\%$ ). In addition, 1D carbon or halloysite NTs and 3D UiO-66 were used to improve rGO NF membranes and these membranes also exhibited excellent performance in purifying dye-containing wastewater [3-5]. Although intercalating different dimensional nano-spacers into GO-based laminar structures is an efficient strategy for tuning the separation performance of the resultant rGO membranes, the long-term operation stability and antifouling property of those membranes could not be ignored.

Constructing NF membrane materials with a photo-induced self-cleaning property gives rise to an emerging organic contaminant water purification technology. Pan's group also reported a  $\alpha\text{-Fe}_2\text{O}_3\text{@rGO}$ /polyacrylonitrile (PAN) nanofiber membrane for the treatment of dye polluting water [6]. Their photocatalytic experiments show that their membrane can effectively degrade a variety of organic dyes, among which the degradation rate of  $20 \text{ mg}\cdot\text{mL}^{-1}$  RhB is  $69.2\%$  within 2 h. However, they didn't report any membrane filtration results. Lv et al. [7] prepared a  $\beta\text{-FeOOH}$  nanorod doped PDA/polyethyleneimine (PEI) photocatalytic NF membrane with large water permeability and enhanced RhB removal performance, but their RhB removal rate ( $77.3\%$ ) was still unsatisfied. Therefore, my data support the idea that 1D intercalation is more efficient in improving water permeability of GO laminar structures. My photocatalytic  $g\text{-C}_3\text{N}_4\text{/rGO}$  composite NF membranes show a high RhB removal rate and excellent long-term stability.

Table 6.1. Comparison of the as-prepared membranes in this work with other reported membranes in terms of organic dyes removal rates.

Membrane	WP (LMH·bar <sup>-1</sup> )	Dye	Removal (%)	Refs.
APT/GO	~9.9	RhB	80	1
PA 6/GO (120)	7.62	MO	99.47	2
PA 6/GO (120)/TiO <sub>2</sub>	13.77	MO	99.36	2
PA 6/GO (120)/SiO <sub>2</sub>	11.39	MO	99.62	2
PA 6/GO (120)/Si <sub>3</sub> N <sub>4</sub>	14.82	MO	99.28	2
CNT/rGO	13	MO	98.2	3
PDA/rGO/HNT	9.95	MB	99.7	4
UiO-66/rGO	14.4	RhB	98.2	5
α-Fe <sub>2</sub> O <sub>3</sub> @rGO/PAN	N/A	RhB	69.2	6
β-FeOOH/PDA-PEI	~9.97	RhB	77.3	7
rGO	2.26	RhB	98.9	This work
<i>g</i> -C <sub>3</sub> N <sub>4</sub> NS/rGO (light)	3.49	RhB	98.7	This work
<i>g</i> -C <sub>3</sub> N <sub>4</sub> NT/rGO (light)	4.77	RhB	98.5	This work

Abbreviations: WP, water permeability; LHM= L·m<sup>-2</sup>·h<sup>-1</sup>; MO, methyl orange; MB, methylene blue; APT, attapulgite; PA, polyamide.

Chapters 4 and 5 are linked studies fabricating nanoporous GO membranes by ion beam modification. Beam line scientists and the leader of Accelerator Science at ANSTO have expressed great interest in my ion beam-modified GO membranes project and will support

future research activities using ion beam technologies to modify 2D materials and 2D material-based separation membranes. The research framework is summarised in Fig. 6.1.

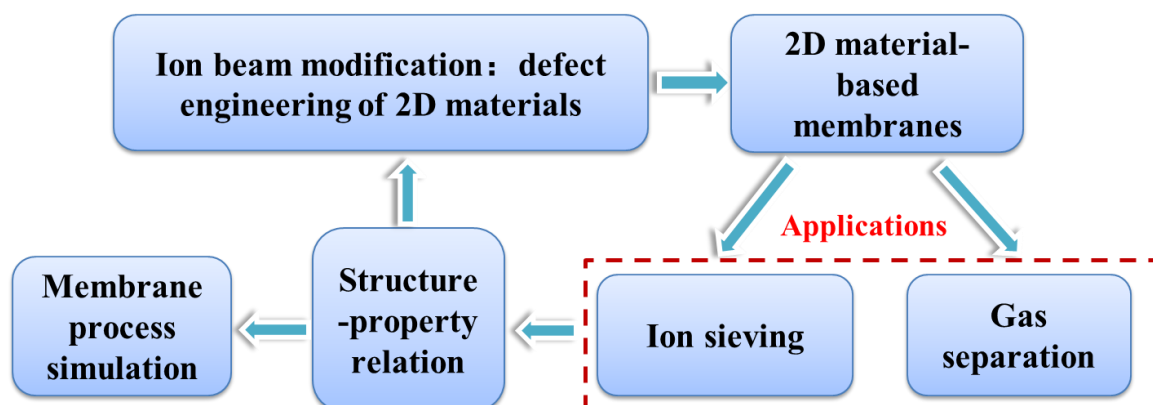


Figure 6.1. Schematic illustration of the project framework for ion beam modification of 2D material-based membranes.

The first attempt at the project that deals with carbon ion beam irradiated GO membranes, provides a robust assessment of the creation of nanopores on thin GO membranes along with reduction of GO. Technical merits of nanoporous GO membranes have been predicted by many theoretical studies (Chapter 4). However, effective approaches for fabrication of such membranes have been reported only rarely. I proposed that ion beam irradiation might offer a wide choice of ion beam ion species and energies, which could be used to achieve on-demand modification of thin GO membranes for the first time. This ground-breaking research makes a distinct and original contribution to our knowledge and understanding of the effect of ion beam irradiation on GO membranes. To address this knowledge gap and gain a preliminary understanding, I embarked on a journey of discovery by testing various types of GO substrate, ion source, ion energy and ion fluence.

Very recently, several experiments have demonstrated that graphene or GO could be efficiently modified by diverse ion beams [8-15] and the irradiation of 2D materials may trigger three main effects including structural modification, defect engineering, and doping effects [16]. For example, O'Hern et al. [17] successfully introduced sub-nanometer defects into a single layer of graphene by an ion beam in a controllable manner, which demonstrated the great potential for development of nanoporous separation membranes. However, Malinsky et al. [18] found that there were no significant compositional changes in the bulk of GO film with thickness  $\sim 50 \mu\text{m}$  associated with ion beam irradiation. In addition, using 250 keV chlorine ions at a fluence of  $5 \times 10^{13} \text{ ions}\cdot\text{cm}^{-2}$ , Ammar et al. [19] believed that

their ion beam could only penetrate through approximately 200 nm of a graphite surface due to dissipation of the irradiating ion energy. These results may suggest that ion beams could create sub-nanometer pores on graphene but that the penetration depth of ions was limited to a shallow depth. To the best of my knowledge, there is still no report on ion beam irradiated thin GO laminar structures with thickness of a few hundreds of nanometers. Therefore, using a low energy carbon ion beam with fluences ranging from  $1 \times 10^{15}$  ions/cm<sup>2</sup> to  $1 \times 10^{17}$  ions·cm<sup>-2</sup>, my results revealed that surface morphologies and chemical states of 150 nm-thick GO films could be efficiently tuned by adjusting the ion fluence. Raman spectral analyses and SRIM simulations experimentally and theoretically confirmed that considerable nano-scaled defects with mean defect distance of about 1.4 nm can be created in GO films through ion beam irradiation. The total vacancy concentrations - point defect concentration- ranges from  $1.4 \times 10^{20}$  -  $1.4 \times 10^{22}$  cm<sup>-3</sup> using ion fluence of  $1 \times 10^{15}$  -  $1 \times 10^{17}$  ions·cm<sup>-2</sup>. These findings support the idea that ion beam irradiated GO laminar structures are tight and porous which make them usable for membrane separation applications.

The ion beam modification approach in Chapter 4 proved to be appropriate for the development of high performance nanoporous GO membranes because it can simultaneously reduce GO and drill nanoscale pores on GO surfaces in a controllable manner. Consequently, ion beam irradiated GO membranes were prepared to sieve mono- and di-valent ions using a diffusion cell (Chapter 5). Although nanoporous GO membranes can exhibit unique performance for water treatment, fabrication of GO with nano-sized pores still lacks investigation (Chapter 5). Unlike other existing methods [20], ion beam modification is a facile and rapid post-treatment for GO membranes. All of the ion beam irradiated GO membranes exhibited improved K<sup>+</sup> selectivity with respect to other ions, when compared with the ion separation performance of the corresponding GO membranes without ion beam treatment. My results also confirmed that ion beam irradiation could be used to modify diamine cross-linked GO membranes. In this research, a fundamental understanding of ion beam-induced nanoporous GO membranes was established, and structure-property relationships of the ion beam irradiated GO membranes were revealed.

There are very few reports available on research of ion beam modified membranes. Back in 1995, Escoubes et al. [21] investigated the effect of ion beam modification on polyimide (PI) membranes and their gas separation (H<sub>2</sub>/CH<sub>4</sub>) performance. They believed that ion beam

modification was extremely significant in their study, because the permeability and selectivity of  $N^+$  irradiated membranes (irradiation energy of 170 keV and fluence of  $2-5 \times 10^{15}$  ions·cm<sup>-2</sup>) were considerably enhanced. In addition, Chennamsetty and Escobar [22] studied the effect of ion beam modification on NF membranes. They post-modified polyamine (PA) and polysulfone (Psf) NF membranes using low energy  $H^+$  ions (fluence of  $1 \times 10^{13}$  -  $5 \times 10^{14}$  ions·cm<sup>-2</sup> at 25 keV). They found that ion beam irradiation resulted in rearrangement of atoms in the membrane, microstructural alterations of the surface layer, and a decrease in surface roughness. My findings support and augment their results as well. However, their ion beam irradiation led to an increase in water flux but keeping the same selectivity, which is the reverse of my results of improved selectivity and decreased permeability for GO membranes. This contrast can be understood by the difference in structure of the two membranes: the separation layer of PA and Psf membranes is porous polymeric matrix while the separation layer of GO membranes is a GO laminar nanostructure. Thus, tuning the laminar structure of 2D material-based membranes (including GO-based membranes) using ion beam post-treatment has been attempted previously yet remains a novel strategy for producing high performance 2D material membranes.

## 6.2 Summary

Membrane technologies are widely utilized for tackling the world-class challenge of purifying water, due to their high separation efficiency and relatively simplistic operation. However, traditional membrane materials suffer from a variety of problems, such as high production cost and huge energy consumption. 2D nanomaterials, especially GO-based materials, have opened new possibilities to construct membrane materials for water treatment with low cost and high performance. Key findings of this thesis are summarized below.

In **Chapter 2**, a literature review was given on bioinspired membranes with special wettability for oily water treatment. Significant advances in the field of bioinspired manufacture have opened new possibilities to improve membrane materials and their performance in separation processes.

In **Chapter 3**, photocatalytic GO-based membranes with self-cleaning characteristics were successfully prepared by reduction of GO and enlarging the interlayer spaces of their laminar structure.  $g-C_3N_4/rGO$  composite NF membranes were successfully fabricated by

intercalating 1D  $g\text{-C}_3\text{N}_4$  NT or 2D  $g\text{-C}_3\text{N}_4$  NS photocatalysts into rGO laminates. Different dimensional intercalation of  $g\text{-C}_3\text{N}_4$  photocatalysts for rGO membranes was investigated for water transport and dye-contaminated water purification. I found that 1D intercalation exhibited more advantages over 2D intercalation for the nanocomposites. The rGO membrane with  $g\text{-C}_3\text{N}_4$  NT exhibited higher water permeability than that with  $g\text{-C}_3\text{N}_4$  NS. The NF and photodegradation of dye contaminants can be achieved in one integrated process for both composite membranes. Upon visible-light irradiation, the as-prepared  $g\text{-C}_3\text{N}_4/\text{rGO}$  membranes exhibited excellent RhB removal efficiencies in long-term operation. This study demonstrated that intercalating 1D nanoscale photocatalysts into rGO membranes offers a new strategy for developing efficient photocatalytic membrane materials.

In **Chapter 4**, a new strategy of ion beam GO membrane modification was proposed for preparation of porous reduced GO membranes. I experimentally confirmed low energy  $\text{C}^+$  could efficiently tune the surface morphologies of GO thin films which was evidenced by the change of reduction degree in GO plane. I found  $\text{C}^+$  selectively removed the unstable functional groups (e.g.  $\text{C}=\text{O}$  species) which may increase structural stability of the GO films. Raman mapping analysis confirmed a mass of defects with mean defect distance of about 1.4 nm were generated in the GO films after irradiation and a higher ion fluence resulted in more defects. SRIM simulation results suggested the total point defect concentrations were  $1.4 \times 10^{20} \text{ cm}^{-3}$ ,  $1.4 \times 10^{21} \text{ cm}^{-3}$  and  $1.4 \times 10^{22} \text{ cm}^{-3}$  for the GO films irradiated at ion fluence of  $1 \times 10^{15} \text{ ions}\cdot\text{cm}^{-2}$ ,  $1 \times 10^{16} \text{ ions}\cdot\text{cm}^{-2}$  and  $1 \times 10^{17} \text{ ions}\cdot\text{cm}^{-2}$ , respectively. These findings confirm that ion beam irradiation may be an efficient tool for post-synthesis of ultrathin GO membranes with nano-scaled pores in a controllable manner in the applications of gas separation and ion sieving.

In **Chapter 5**, I successfully applied ion beam irradiation for simultaneous *in-situ* reduction and defect engineering of GO membranes. The laminar structure of GO membranes could be controllably tuned for reduction of interlayer spaces and tailoring nanoscale pores, which was investigated in this thesis for the first time (to the best of my knowledge). The thickness of the GO layer and the ion fluence utilized have a significant influence on the resultant GO structure. Mono-/di-valent metal ion separation performance by these membranes depends on their structure.  $\text{K}^+$  selectivity (compared with other ions) improved with all GO membranes following ion beam irradiation. Moreover, ion beam irradiation could be extended to EDA-modified GO membranes.

Overall, this thesis shows that nanotechnology plays a growing role in membrane fabrication techniques, and 2D nanomaterial-based membranes have enriched the membrane family. Tuning laminar structures of GO-based membranes may bring further innovations in water treatment industries. However, the GO membranes prepared in this research have very small areas due to technical limitations in production. GO membranes are also required to exhibit high water permeability, prolonged high salt and dye rejection under harsh conditions as well. Therefore, to achieve real industrial practice, more efforts are needed to fabricate robust high-performance GO membranes with large membrane areas and excellent industrial manufacturability.

### 6.3 References

- [1] C.-Y. Wang, W.-J. Zeng, T.-T. Jiang, X. Chen, X.-L. Zhang, Incorporating attapulgite nanorods into graphene oxide nanofiltration membranes for efficient dyes wastewater treatment, *Sep. Purif. Technol.* (2018).
- [2] L. Chen, N. Li, Z. Wen, L. Zhang, Q. Chen, L. Chen, P. Si, J. Feng, Y. Li, J. Lou, L. Ci, Graphene oxide based membrane intercalated by nanoparticles for high performance nanofiltration application, *Chem. Eng. J.* 347 (2018) 12-18.
- [3] X. Chen, M. Qiu, H. Ding, K. Fu, Y. Fan, A reduced graphene oxide nanofiltration membrane intercalated by well-dispersed carbon nanotubes for drinking water purification, *Nanoscale* 8 (2016) 5696-5705.
- [4] Y. Liu, W. Tu, M. Chen, L. Ma, B. Yang, Q. Liang, Y. Chen, A mussel-induced method to fabricate reduced graphene oxide/halloysite nanotubes membranes for multifunctional applications in water purification and oil/water separation, *Chem. Eng. J.* 336 (2018) 263-277.
- [5] K. Guan, D. Zhao, M. Zhang, J. Shen, G. Zhou, G. Liu, W. Jin, 3D nanoporous crystals enabled 2D channels in graphene membrane with enhanced water purification performance, *J. Membr. Sci.* 542 (2017) 41-51.
- [6] K. Sun, L. Wang, C. Wu, J. Deng, K. Pan, Fabrication of  $\alpha$ -Fe<sub>2</sub>O<sub>3</sub>@rGO/PAN nanofiber composite membrane for photocatalytic degradation of organic dyes, *Adv. Mater. Interface.* 4 (2017) 1700845.



- [7] Y. Lv, C. Zhang, A. He, S.-J. Yang, G.-P. Wu, S.B. Darling, Z.-K. Xu, Photocatalytic nanofiltration membranes with self-cleaning property for wastewater treatment, *Adv. Funct. Mater.* 27 (2017) 1700251.
- [8] S. H. Al-Harhi, A. Kara'a, T. Hysen, M. Elzain, A. T. Al-Hinai; M. T. Z. Myint, Evolution of surface morphology and electronic structure of few layer graphene after low energy Ar<sup>+</sup> ion irradiation. *Appl. Phys. Lett.* 21 (2012) 101.
- [9] S. Kim, A. V. Ievlev, J. Jakowski, I. V. Vlassiuk, X. Sang; C. Brown, O. Dyck, R. R. Unocic, S. V. Kalinin, A. Belianinov, B. G. Sumpter, S. Jesse, O. S. Ovchinnikova, Multi-purposed Ar gas cluster ion beam processing for graphene engineering. *Carbon* 131 (2018) 142-148.
- [10] C. W. Jang, J. H. Kim, D. H. Lee, D. H. Shin, S. Kim, S.-H. Choi, E. Hwang, R. G. Elliman, Effect of stopping-layer-assisted boron-ion implantation on the electrical properties of graphene: Interplay between strain and charge doping. *Carbon* 118 (2017) 343-347.
- [11] P. Ahlberg, F. O. L. Johansson, Z. B. Zhang, U. Jansson, S. L. Zhang, A. Lindblad, T. Nyberg, Defect formation in graphene during low-energy ion bombardment. *APL Mater.* 4 (2016) 4.
- [12] Q. Wang, Y. Shao, D. Ge, Q. Yang, N. Ren, Surface modification of multilayer graphene using Ga ion irradiation. *J. Appl. Phys.* 117 (2015) 16.
- [13] Q. Wang, W. Mao, D. Ge, Y. Zhang, Y. Shao, N. Ren, Effects of Ga ion-beam irradiation on monolayer graphene. *Appl. Phys. Lett.* 103 (2013) 7.
- [14] Y. Xu, K. Zhang, C. Brüsewitz, X. Wu, H. C. Hofsäss, Investigation of the effect of low energy ion beam irradiation on mono-layer graphene. *AIP Advances* 7 (2013) 3.
- [15] G. Gawlik, P. Ciepielewski, J. Jagielski, J. Baranowski, Modification of graphene by ion beam. *Nucl. Instrum. Meth. B* 406 (2017) 683-688.
- [16] Z. Li, F. Chen, Ion beam modification of two-dimensional materials: Characterization, properties, and applications. *Appl. Phys. Rev.* 1 (2017) 4.

- [17] S. C. O'Hern, M. S. Boutilier, J. C. Idrobo, Y. Song, J. Kong, T. Laoui, M. Atieh, R. Karnik, Selective ionic transport through tunable subnanometer pores in single-layer graphene membranes. *Nano Lett.* 14 (2014) 1234-41.
- [18] Malinsky, P.; Mackova, A.; Miksova, R.; Kovacikova, H.; Cutroneo, M.; Luxa, J.; Bousa, D.; Strochova, B.; Sofer, Z., Graphene oxide layers modified by light energetic ions. *Phys. Chem. Chem. Phys.* 19 (2017) 10282-10291.
- [19] M. R. Ammar, J. N. Rouzaud, C. E. Vaudey, N. Toulhoat, N. Moncoffre, Characterization of graphite implanted with chlorine ions using combined Raman microspectrometry and transmission electron microscopy on thin sections prepared by focused ion beam. *Carbon* 48 (2010) 1244-1251.
- [20] Z. Li, X. Zhang, H. Tan, W. Qi, L. Wang, M. C. Ali, H. Zhang, J. Chen, P. Hu, C. Fan, H. Qiu, Combustion fabrication of nanoporous graphene for ionic separation membranes. *Adv. Funct. Materials* 28 (2018) 1805026.
- [21] M. Escoubes, J.Y. Dolveck, J. Davenas, X.L. Xu, G. Boiteux, Ion beam modification of polyimide membranes for gas permeation. *Nucl. Instrum. Meth. B* 105 (1995) 130-133.
- [22] R. Chennamsetty, I. Escobar, Effect of ion beam irradiation on two nanofiltration water treatment membranes. *Sep. Sci. Technol.* 43 (2008) 4009-4029.